Chapter 9: *Remote Sensing* - Lead Author Arlene Laing, CIRA, Colorado State University

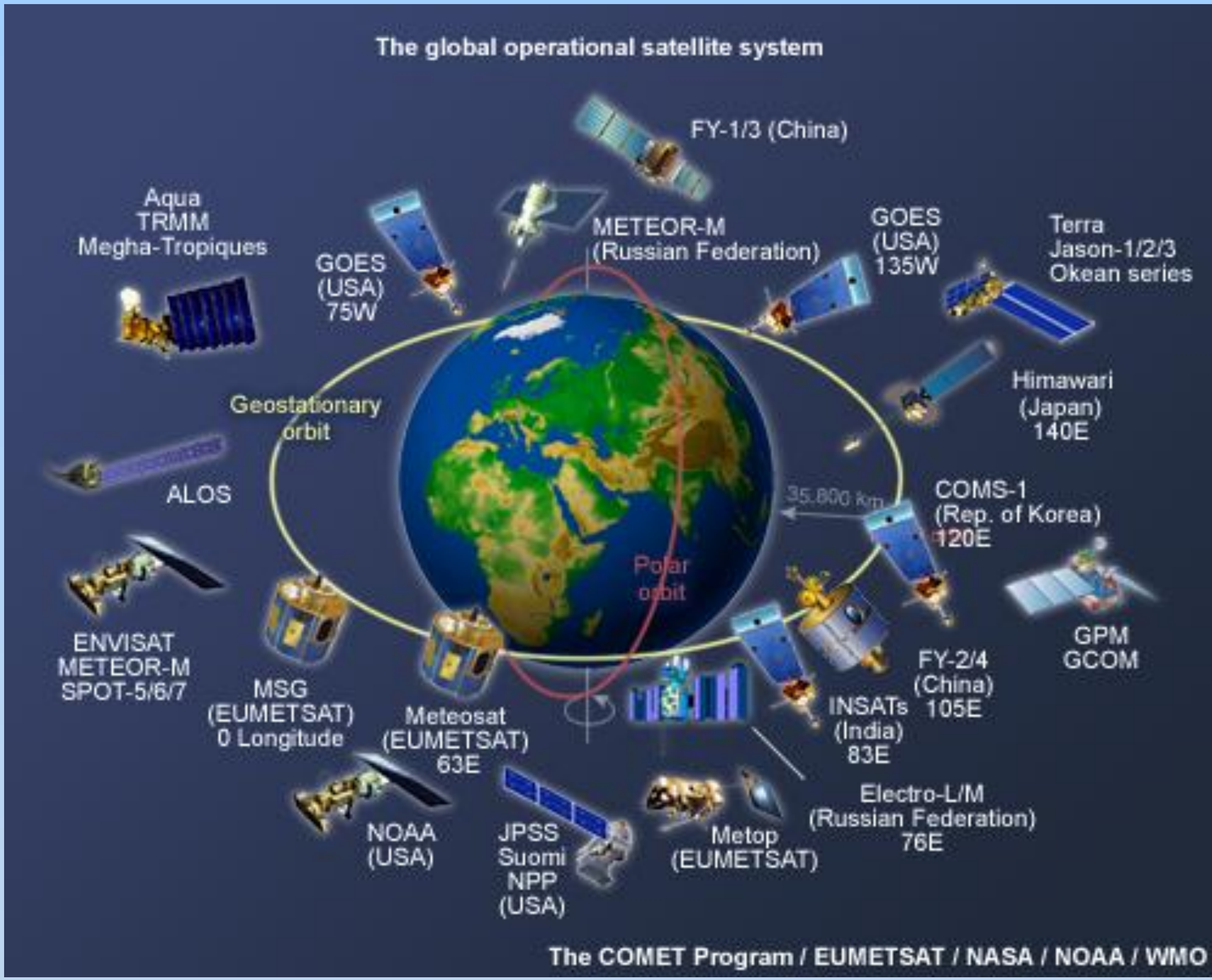

Figure 9.1.The global operational satellite observing system (World Meteorological Organization (WMO), 2005).

Chapter 9: *Remote Sensing* - Lead Author Arlene Laing, CIRA, Colorado State University

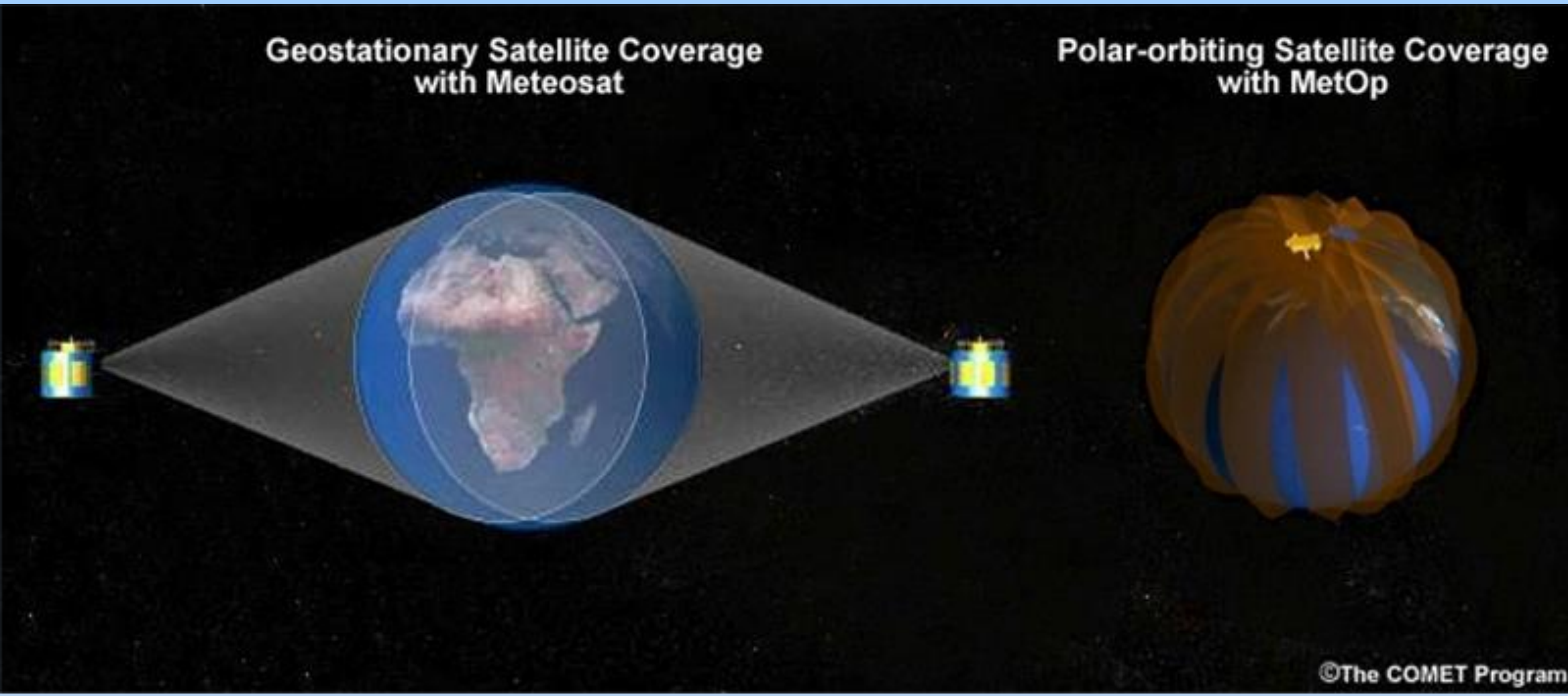

Figure 9.1.The global operational satellite observing system (World Meteorological Organization (WMO), 2005).

Chapter 9: *Remote Sensing* - Lead Author Arlene Laing, CIRA, Colorado State University

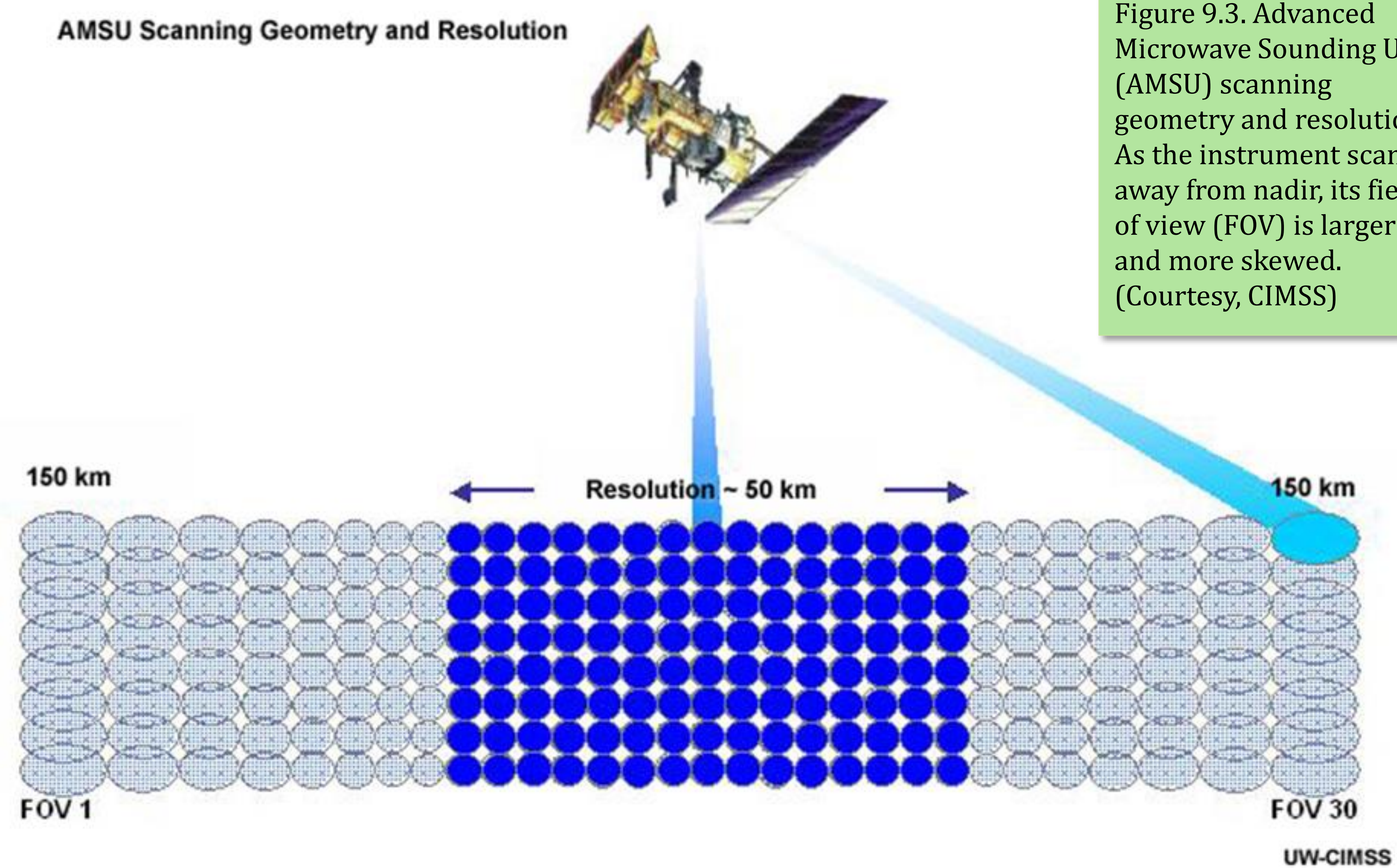

Figure 9.3. Advanced Microwave Sounding Unit (AMSU) scanning geometry and resolution. As the instrument scans away from nadir, its field of view (FOV) is larger and more skewed. (Courtesy, CIMSS)

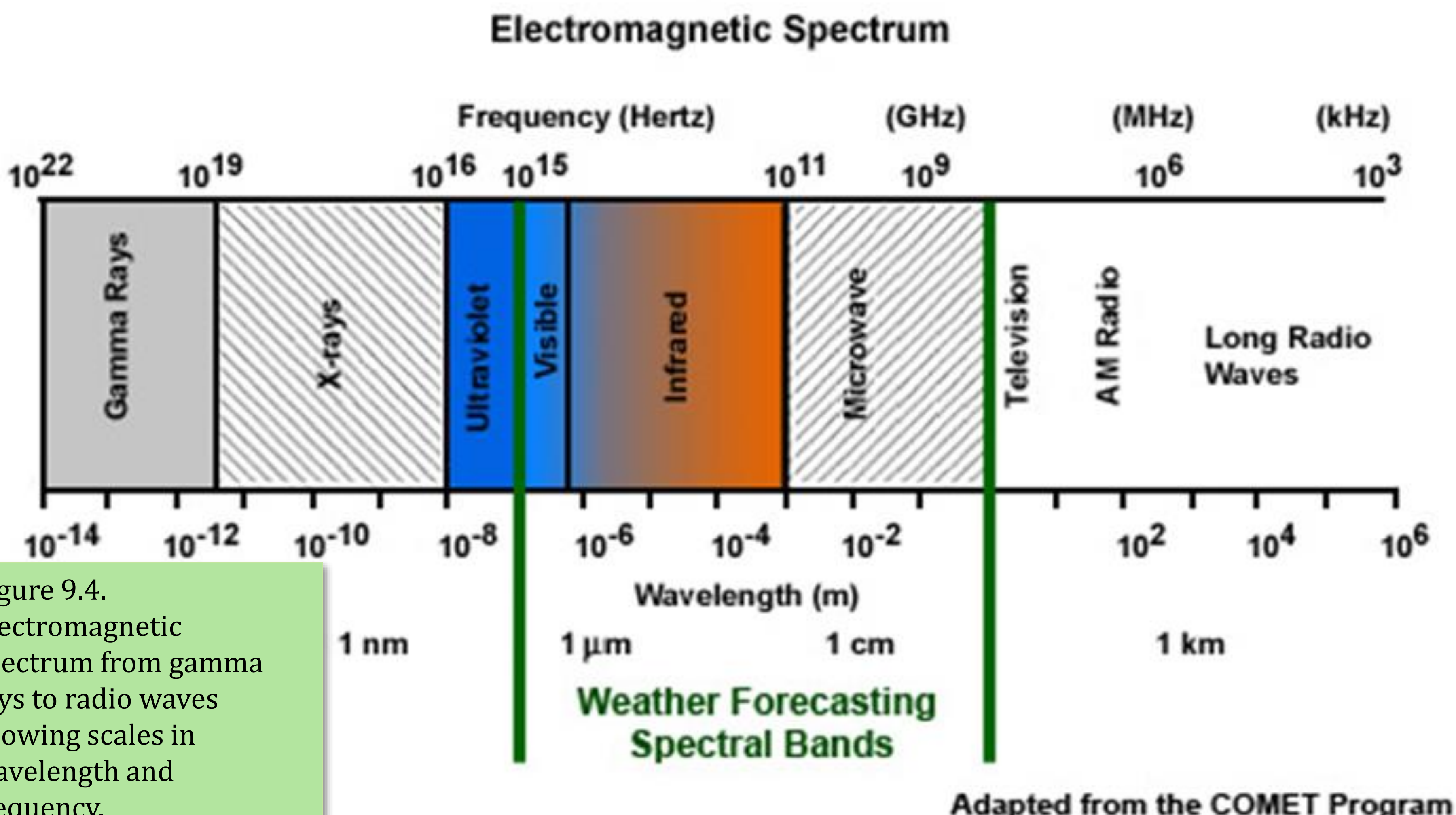

Figure 9.4. Electromagnetic spectrum from gamma rays to radio waves showing scales in wavelength and frequency.

Figure 9.5 Conceptual diagram of the spectral radiance or specific intensity of radiation

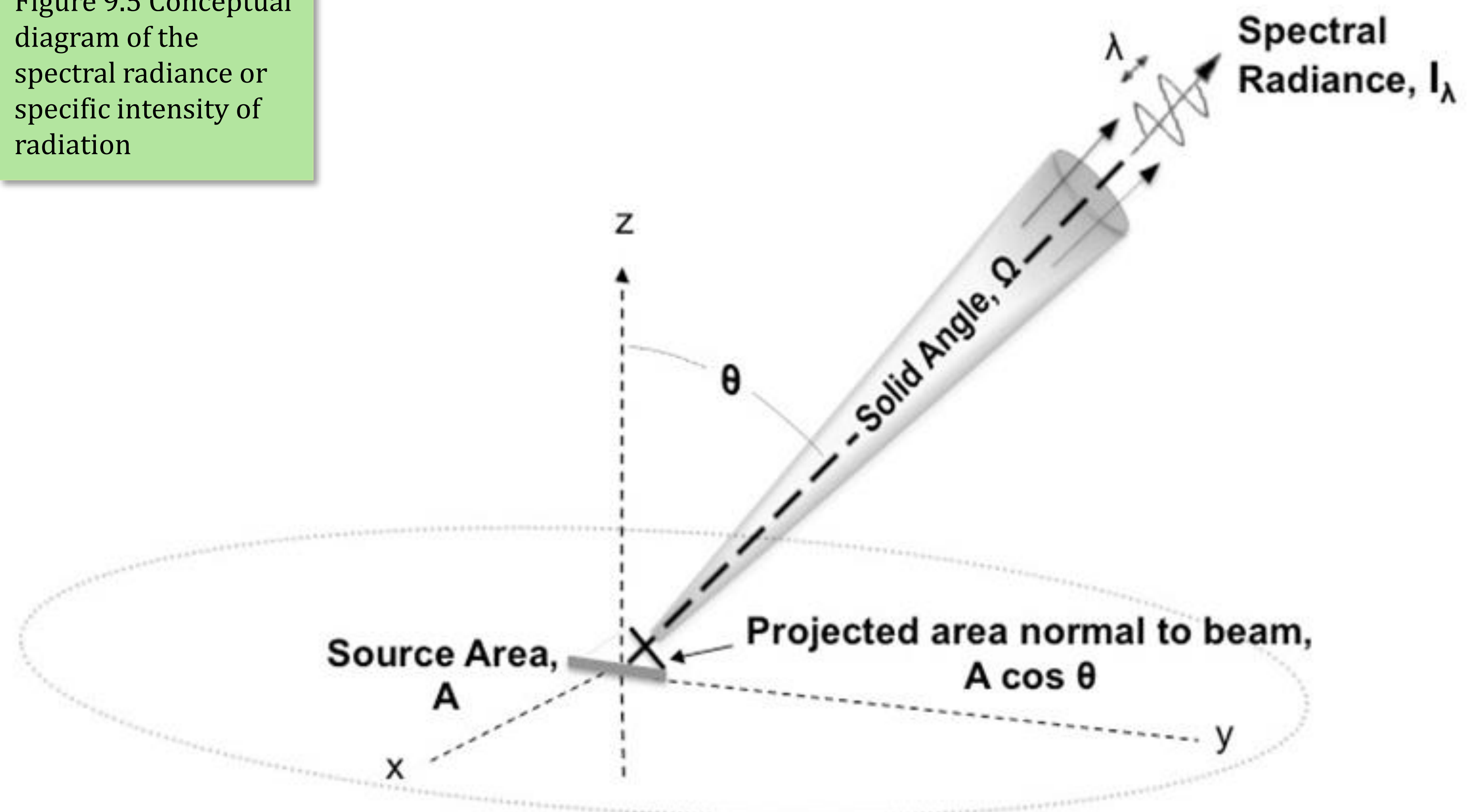

Chapter 9: ***Remote Sensing*** **- Lead Author Arlene Laing, CIRA, Colorado State University**

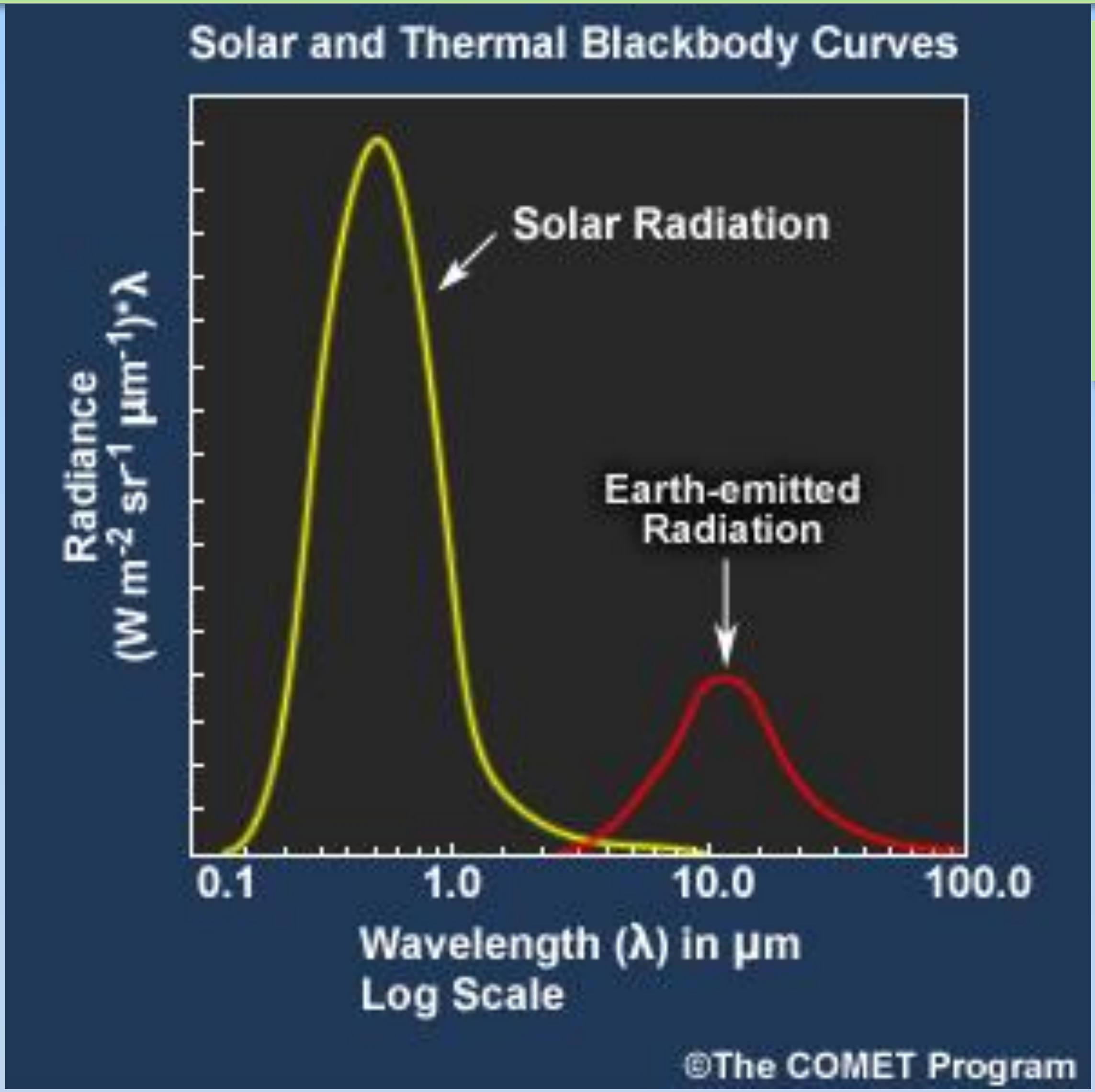

Figure 9.6 The radiance (W m-2 sr-1μm-1) normalised per wavelength on a logarithmic scale. The areas under the yellow and red lines represent solar and terrestrial radiance respectively.

Chapter 9: *Remote Sensing* - Lead Author Arlene Laing, CIRA, Colorado State University

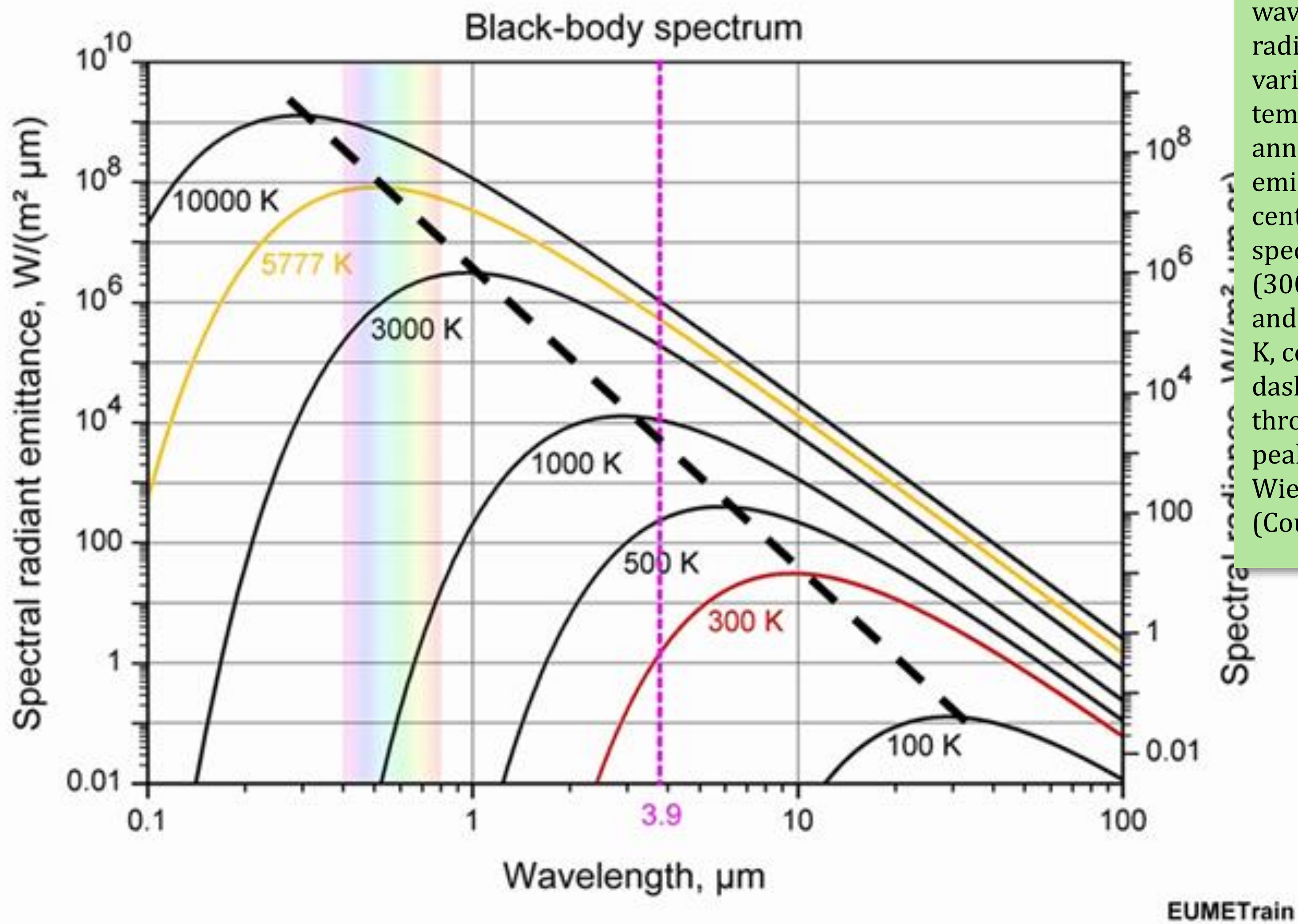

Figure 9.7. Log-scale plot of wavelength and spectral radiance and emittance for various black body temperatures. Coloured annotations mark the emissions of the Sun (5777 K, centred on 0.5 µm, visible spectrum), the Earth's surface (300 K, centred on 10 µm), and forest fires (600 to 1000 K, centred on 3.9 µm). The dashed diagonal line runs through the wavelengths of peak emission, illustrating Wien's Displacement Law. (Courtesy EUMETrain)

Chapter 9: *Remote Sensing* - Lead Author Arlene Laing, CIRA, Colorado State University

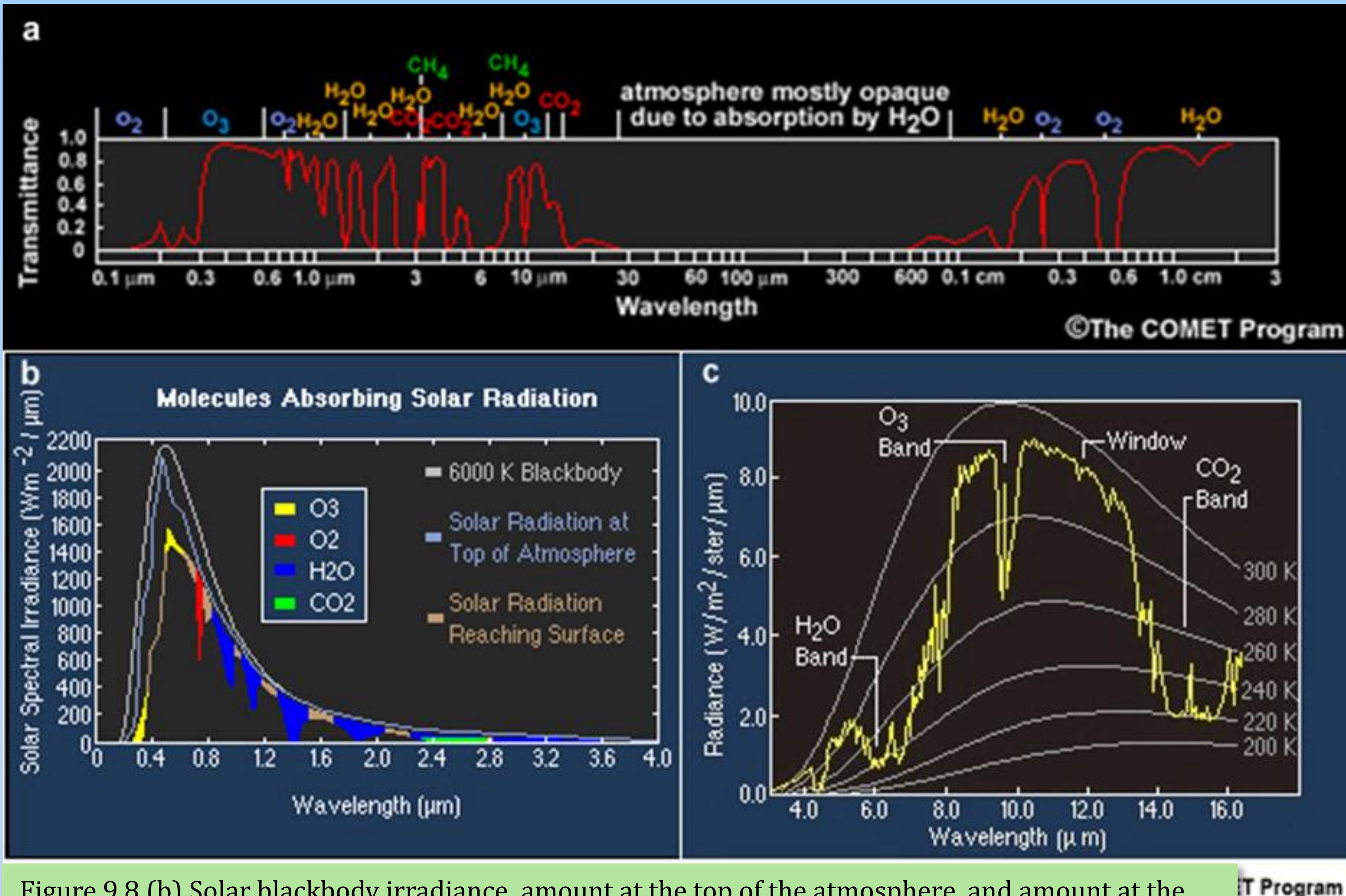

Figure 9.8 (a)Transmittance, a measure of the fraction of radiation passing through the atmosphere, from ultraviolet to microwave wavelengths. The higher the red line the greater the amount of radiation transmitted through the atmosphere. Wavelengths with transmittance at or near 1.0 are referred to as atmospheric windows.

Figure 9.8 (b) Solar blackbody irradiance, amount at the top of the atmosphere, and amount at the surface after atmospheric absorption. (c) Terrestrial blackbody radiance for different temperatures and the reduced surface radiance transmitted because of atmospheric absorption.

African Monsoon Multidisciplinary Analysis

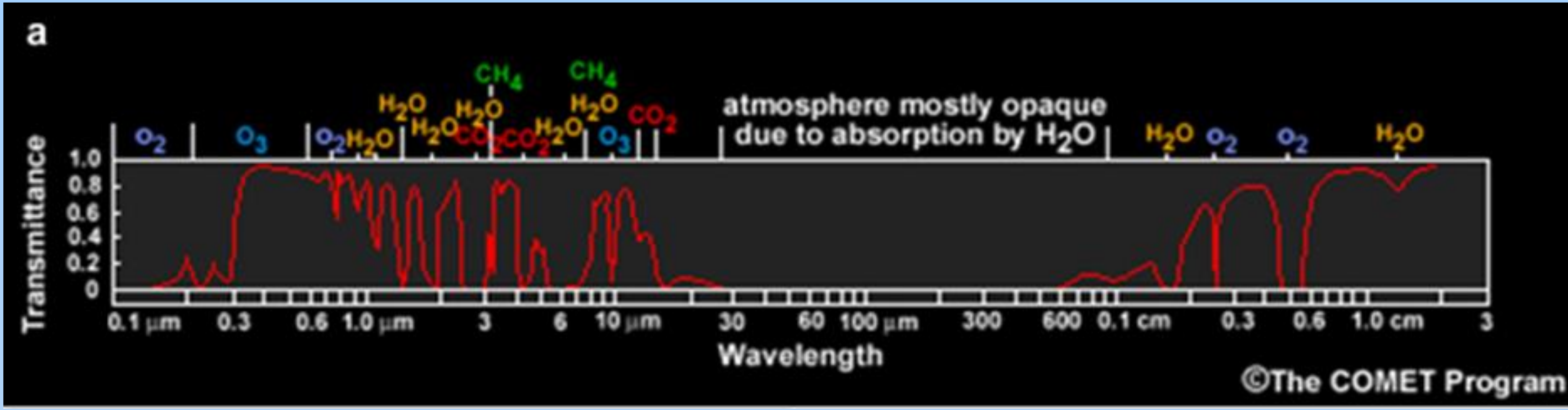

Figure 9.8 (a)Transmittance, a measure of the fraction of radiation passing through the atmosphere, from ultraviolet to microwave wavelengths. The higher the red line the greater the amount of radiation transmitted through the atmosphere. Wavelengths with transmittance at or near 1.0 are referred to as atmospheric windows.

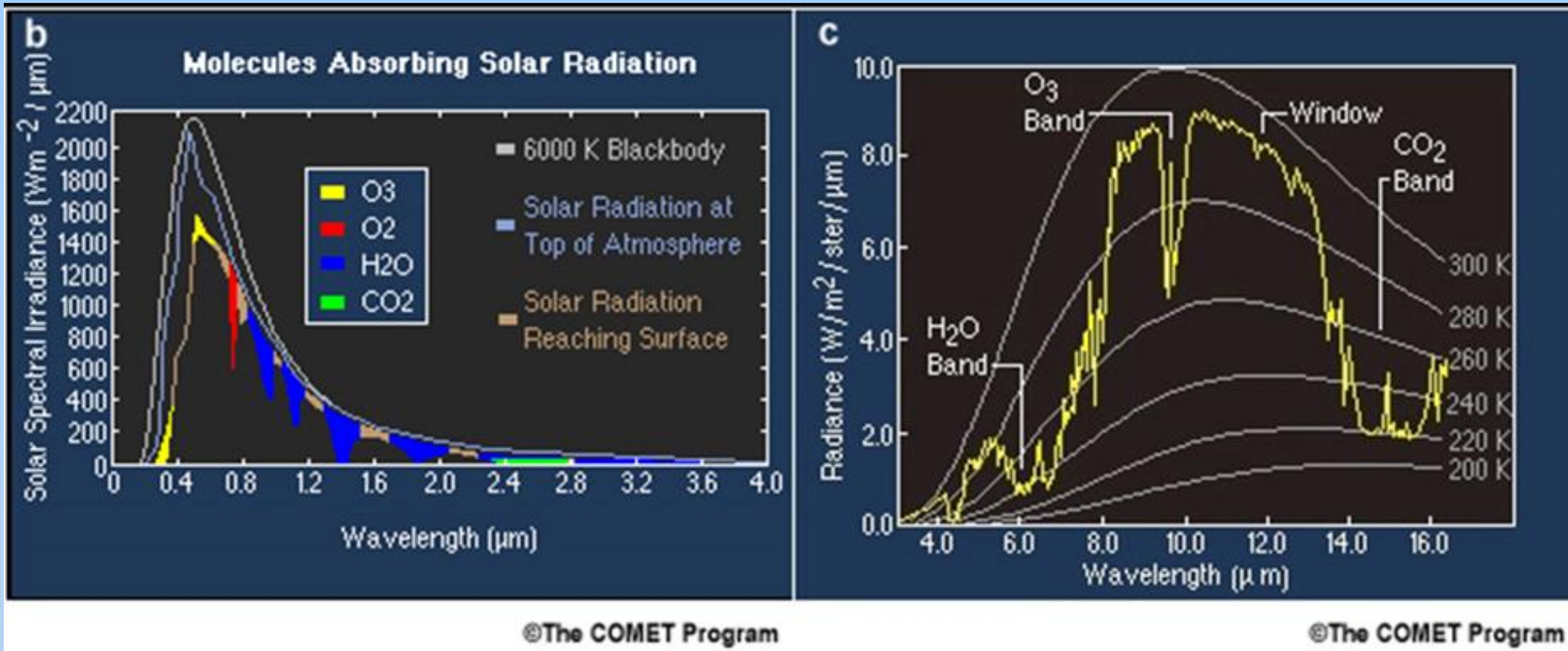

Figure 9.8 (b) Solar blackbody irradiance, amount at the top of the atmosphere, and amount at the surface after atmospheric absorption. (c) Terrestrial blackbody radiance for different temperatures and the reduced surface radiance transmitted because of atmospheric absorption.

Chapter 9: *Remote Sensing* - Lead Author Arlene Laing, CIRA, Colorado State University

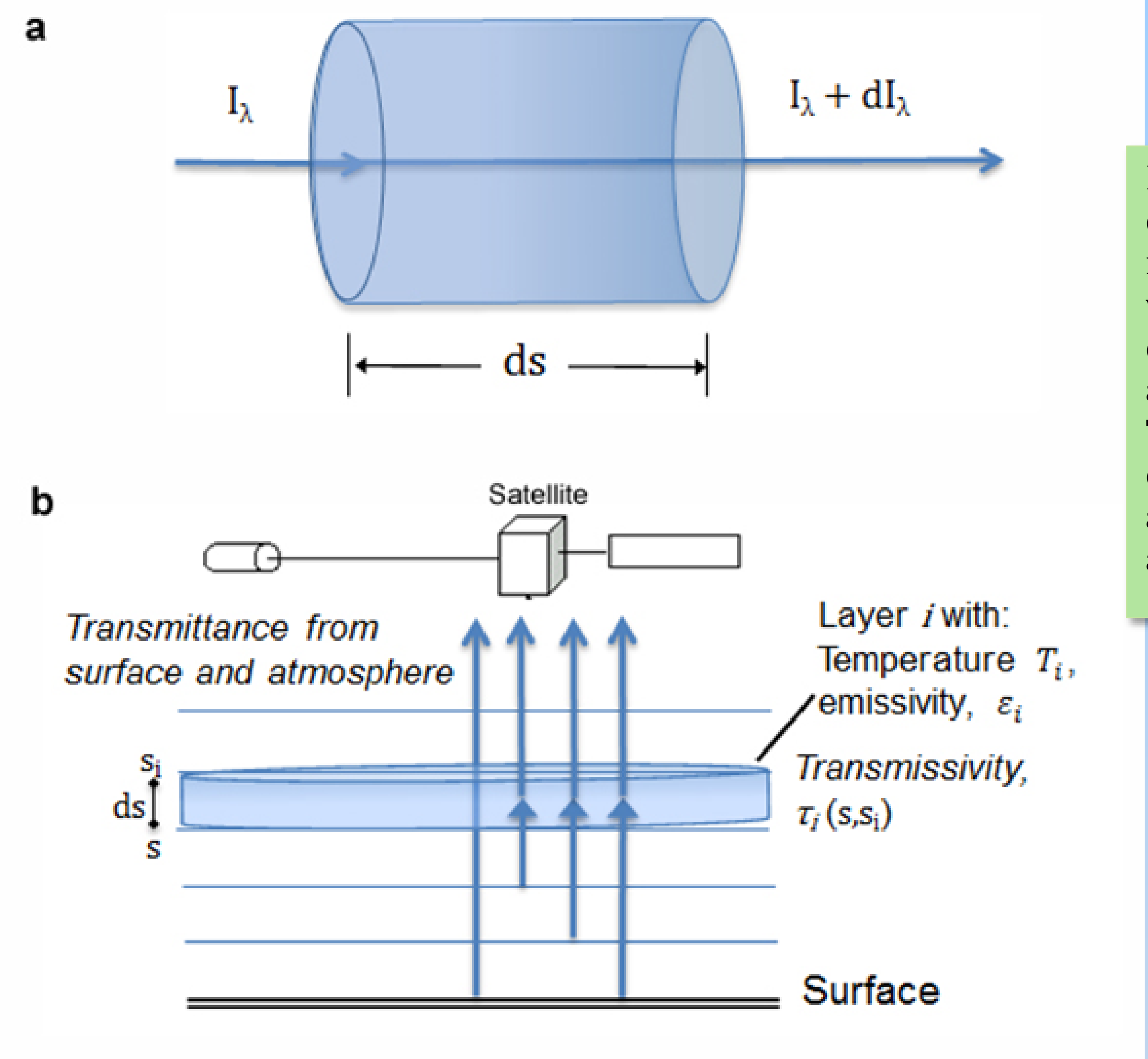

Figure 9.9 (a) Schematic diagram of the change of radiance (for a given wavelength) over a distance, s through the atmosphere. (b) Transmittance and emission from a layer in a plane-parallel atmosphere

Chapter 9: *Remote Sensing* - Lead Author Arlene Laing, CIRA, Colorado State University

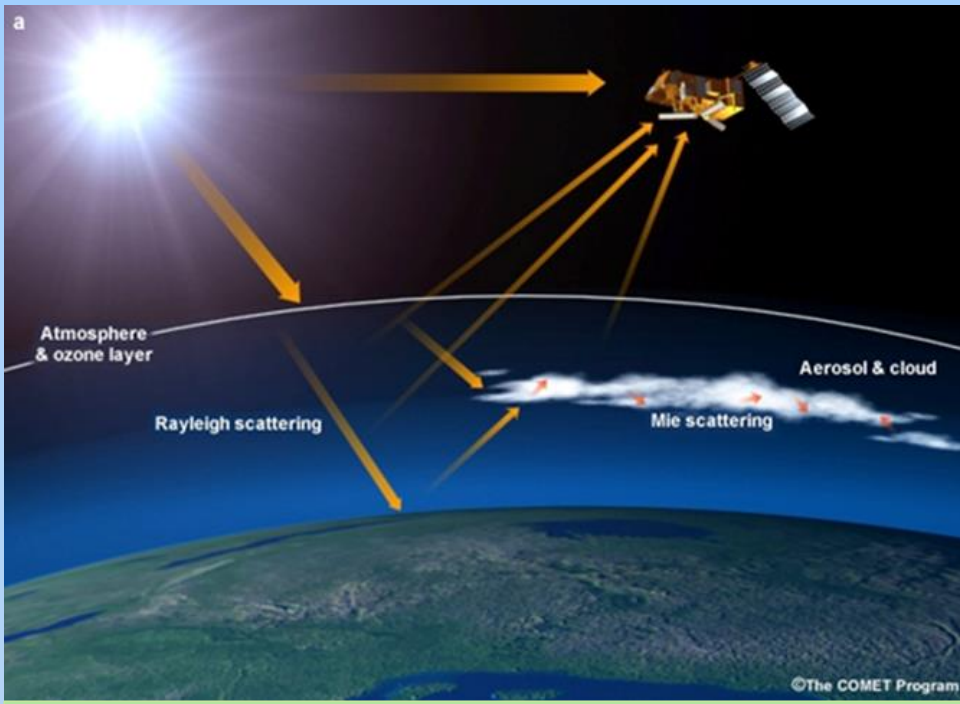

Figure 9.10 (a) Schematic of satellite sensing direct sunlight and light scattered by the atmosphere and surface.

Figure 9.10(b) Conceptual diagram of the incident radiance, Ii, and reflected radiance, Ir. Both the incident and reflected quantities are dependent on the zenith angle, θ, and the azimuth angle, Φ. The fraction of the incident radiation that is reflected is termed the reflectance and varies according to the medium on which the radiation is incident.

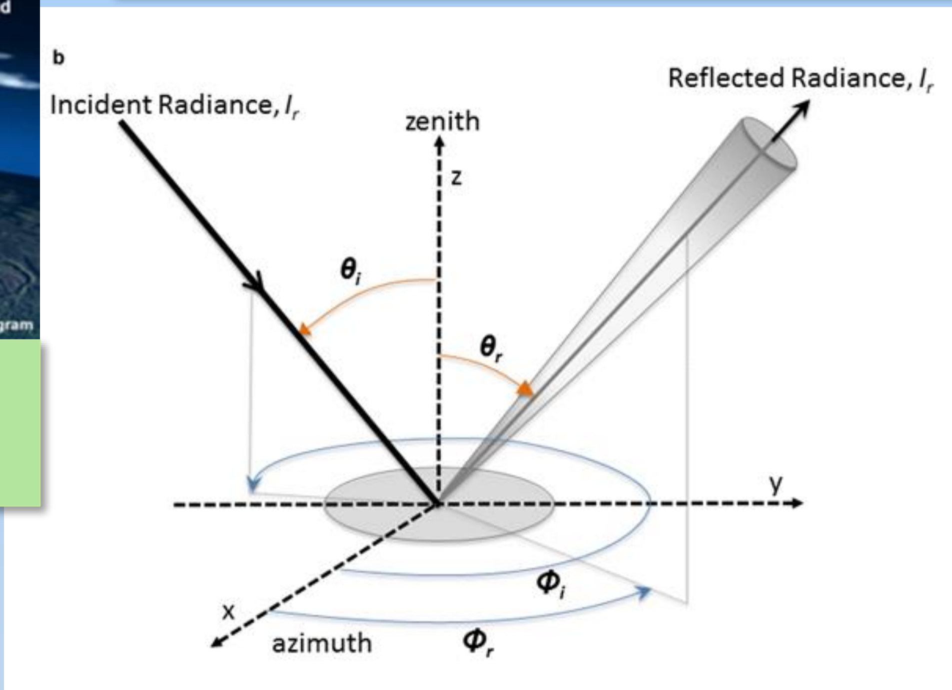

Chapter 9: *Remote Sensing* - Lead Author Arlene Laing, CIRA, Colorado State University

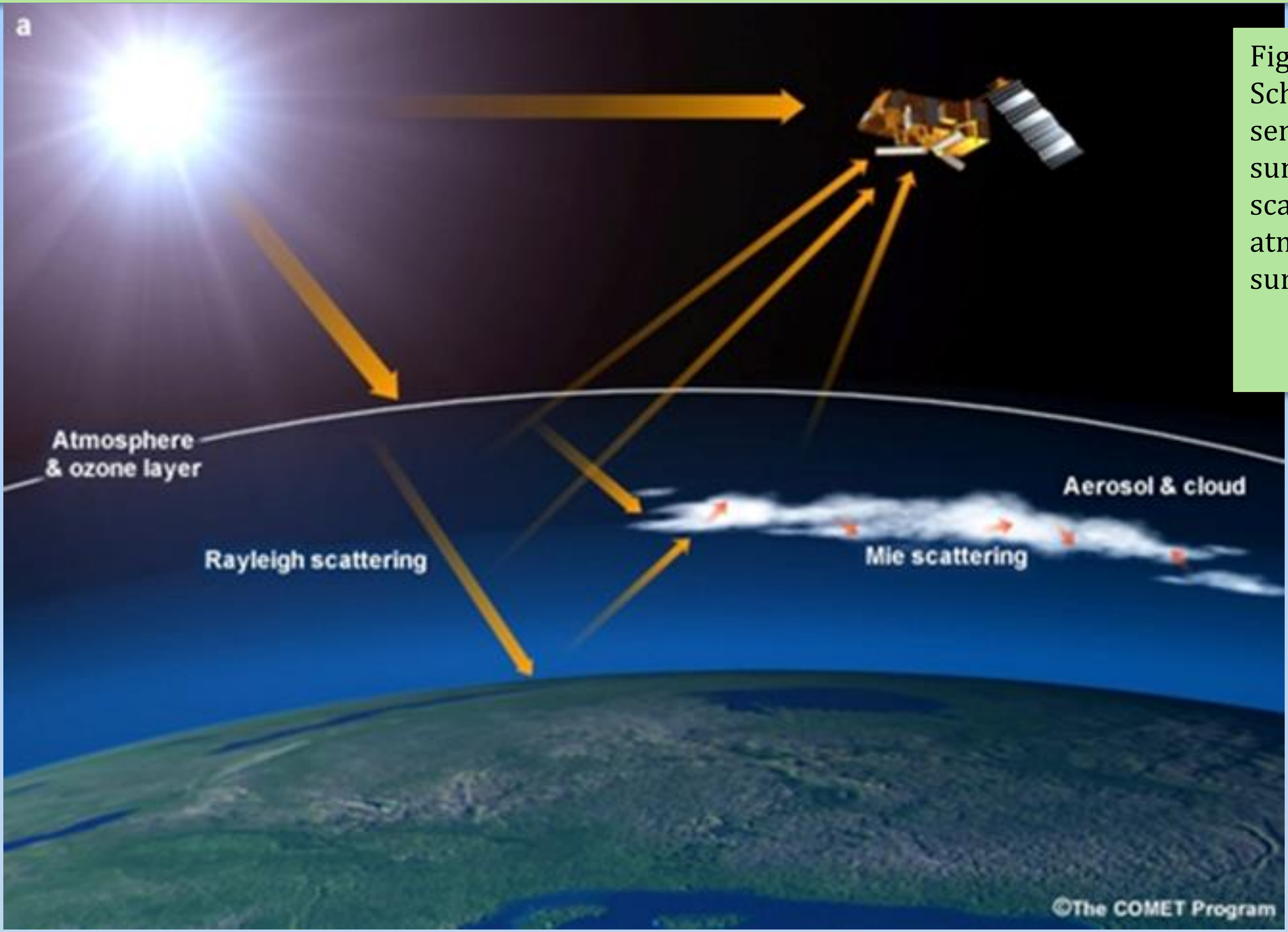

Figure 9.10 (a) Schematic of satellite sensing direct sunlight and light scattered by the atmosphere and surface.

Chapter 9: *Remote Sensing* - Lead Author Arlene Laing, CIRA, Colorado State University

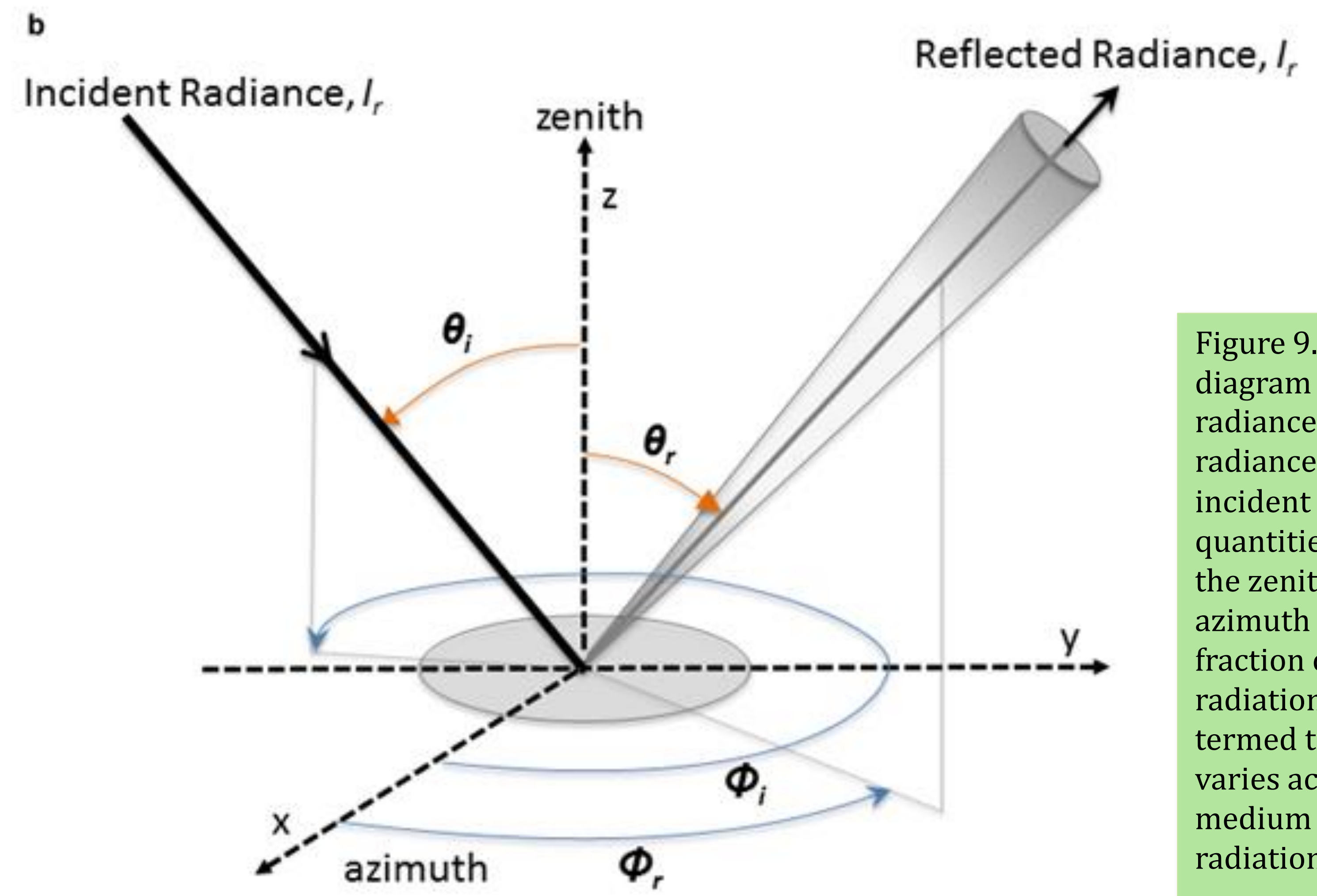

Figure 9.10(b) Conceptual diagram of the incident radiance, Ii, and reflected radiance, Ir. Both the incident and reflected quantities are dependent on the zenith angle, θ, and the azimuth angle, Φ. The fraction of the incident radiation that is reflected is termed the reflectance and varies according to the medium on which the radiation is incident.

African Monsoon Multidisciplinary Analysis

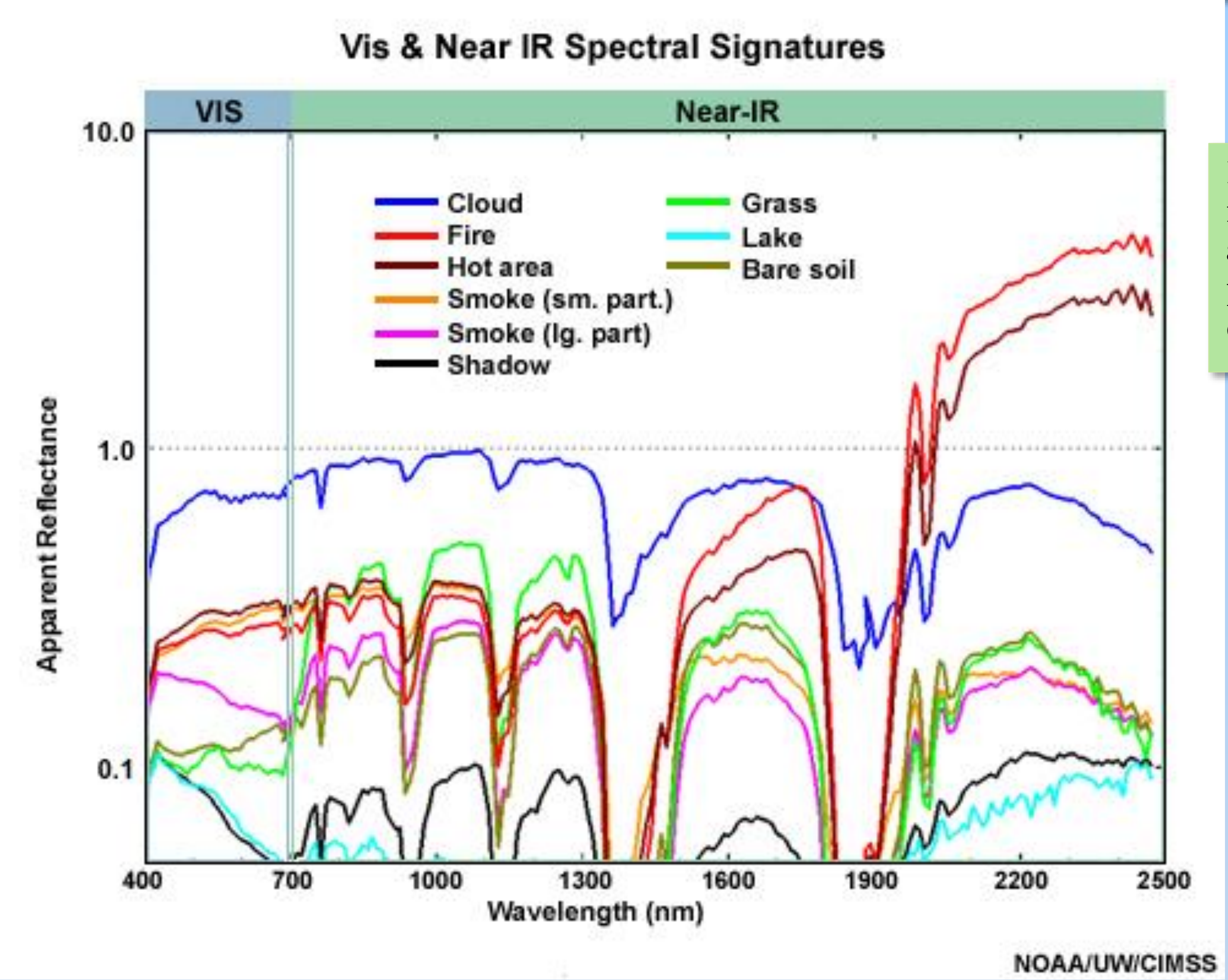

Figure 9.11. Apparent reflectance from various atmospheric phenomena and surface cover.

Chapter 9: *Remote Sensing* - Lead Author Arlene Laing, CIRA, Colorado State University

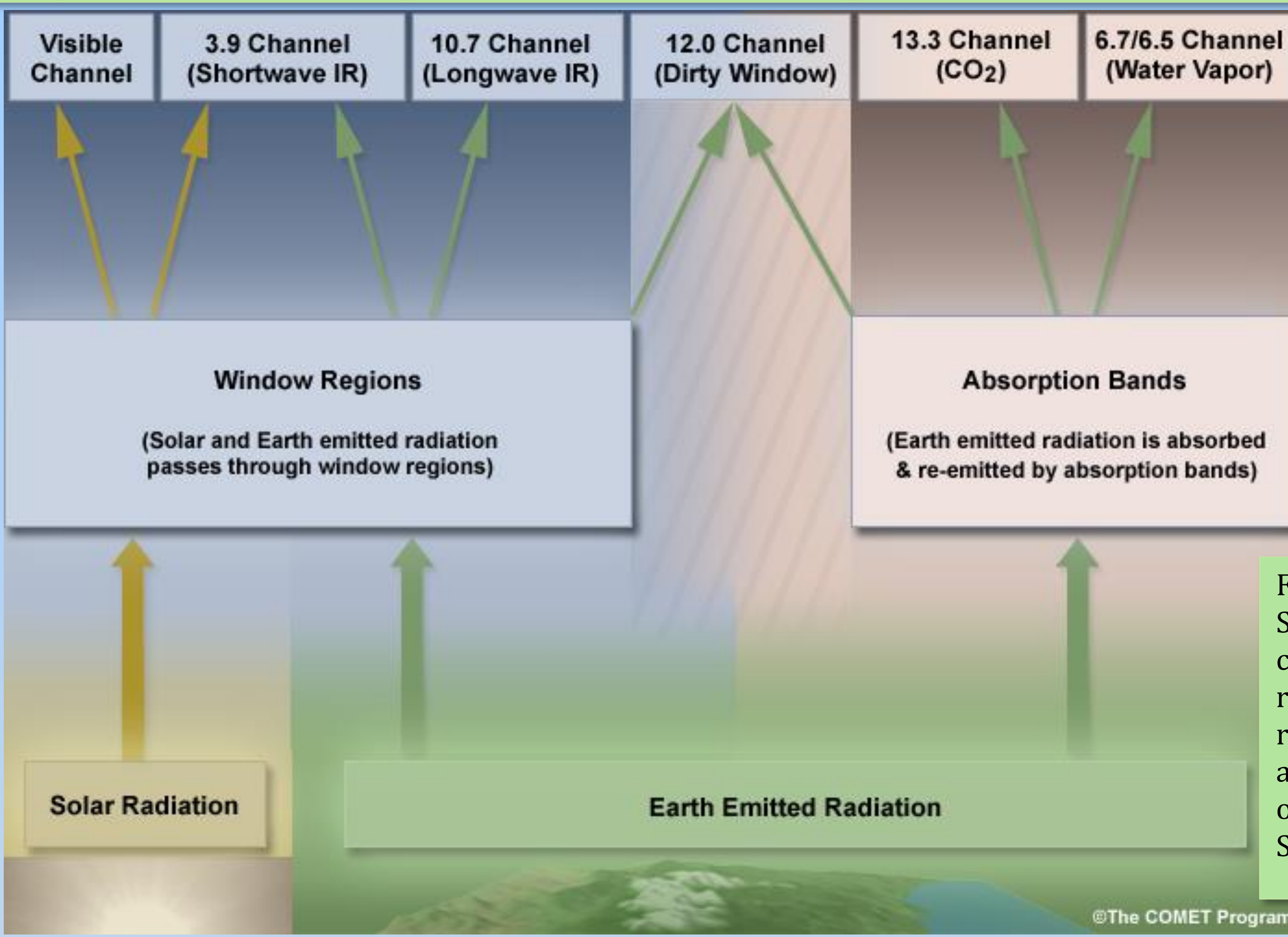

Figure 9.12 Schematic of channels that represent window regions and absorption bands on the Meteosat SEVIRI.

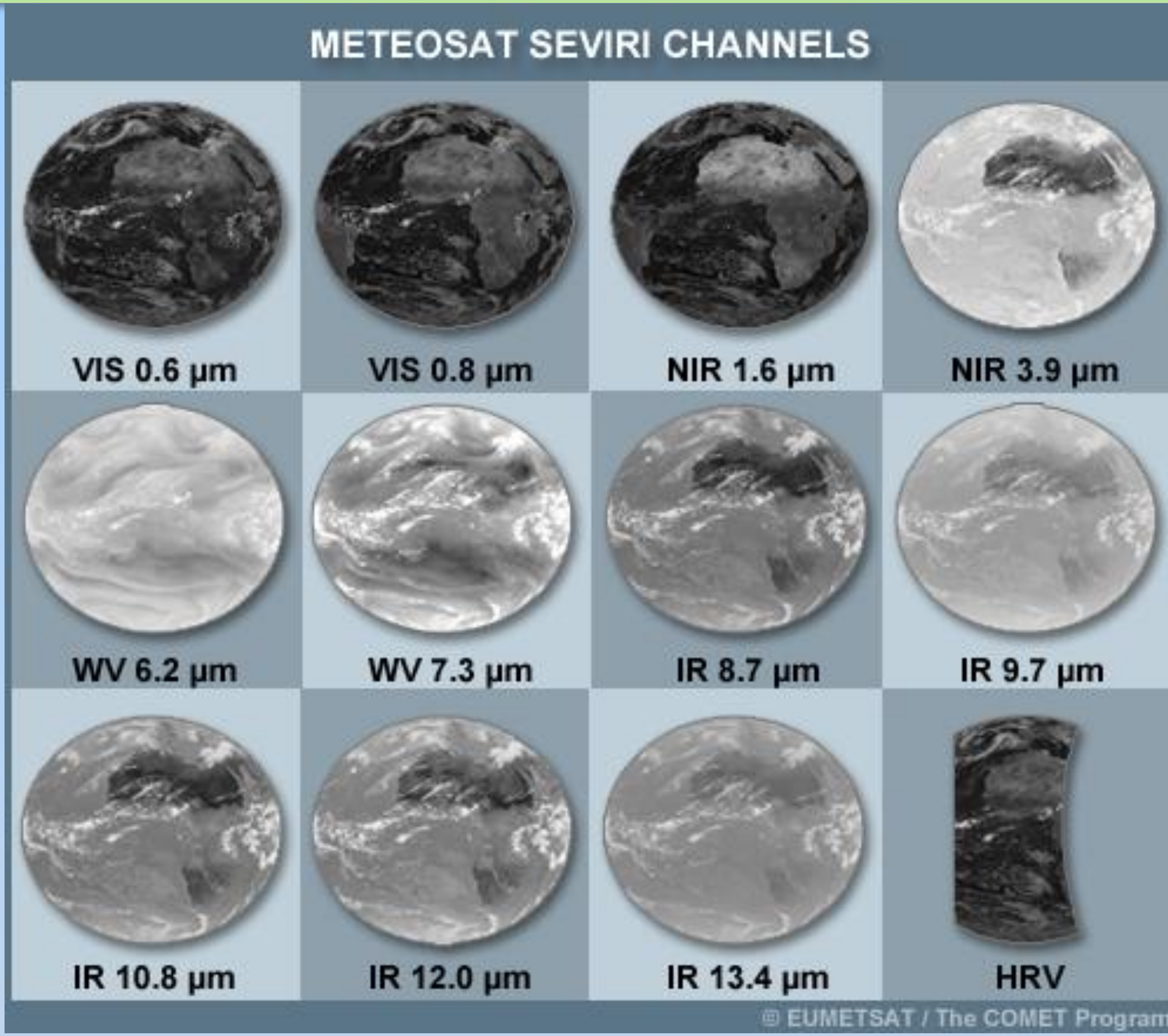

Figure 9.13. The channels on the Meteosat Second Generation (MSG) SEVIRI instrument

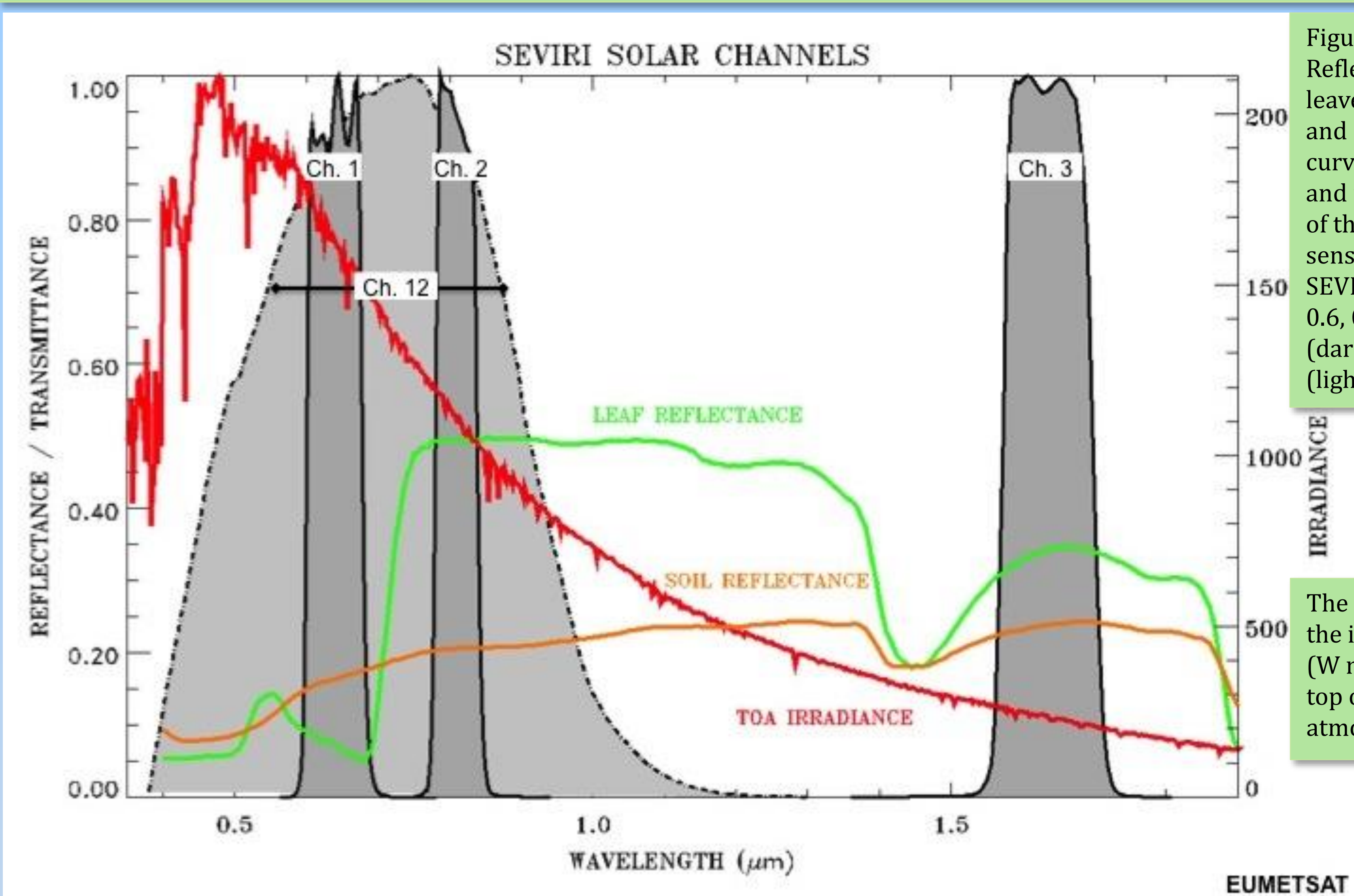

Figure 9.14 Reflectance from leaves (green curve) and soil (orange curve) in the visible and near-IR region of the spectrum, as sensed by four SEVIRI channels: 0.6, 0.8 and 1.6 μm (dark grey) and HRV (light grey).

The red line is the irradiance (W m-2) at the top of the atmosphere.

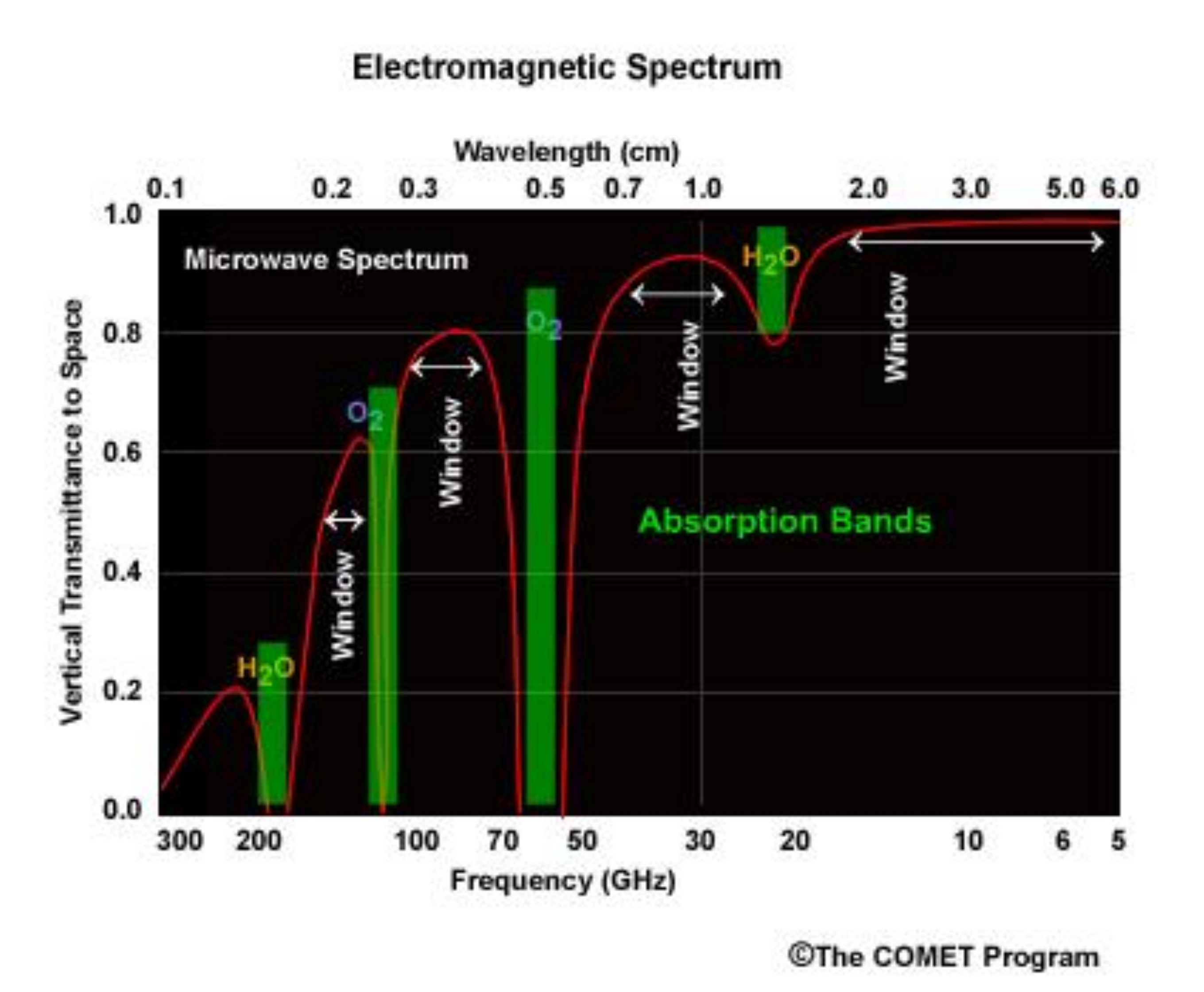

Figure 9.15. The window and absorption bands at microwave wavelengths

Chapter 9: *Remote Sensing* - Lead Author Arlene Laing, CIRA, Colorado State University

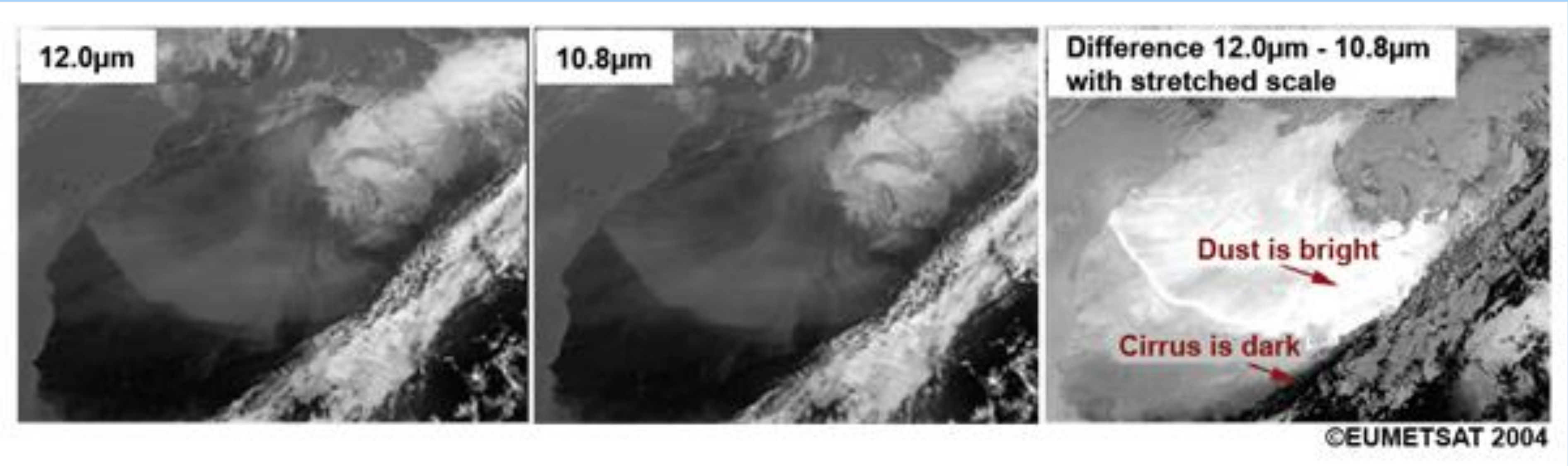

Figure 9.16 Images of Meteosat SEVIRI IR12.0, IR10.8, and IR12.0 - IR10.8 difference

Chapter 9: *Remote Sensing* - Lead Author Arlene Laing, CIRA, Colorado State University

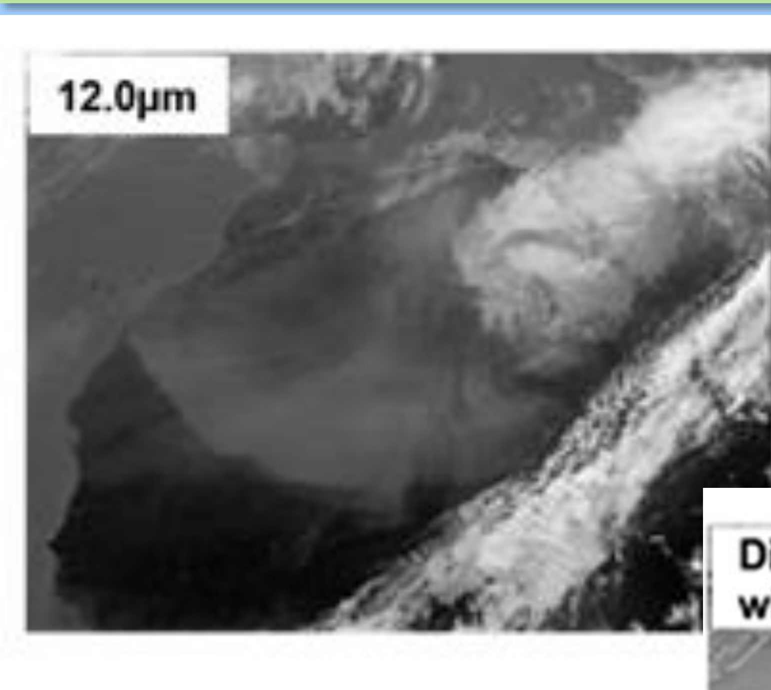

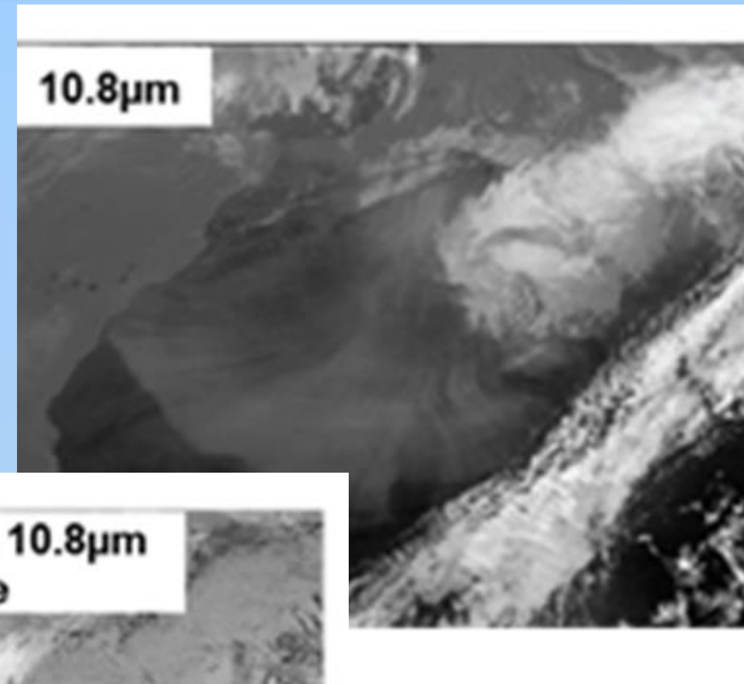

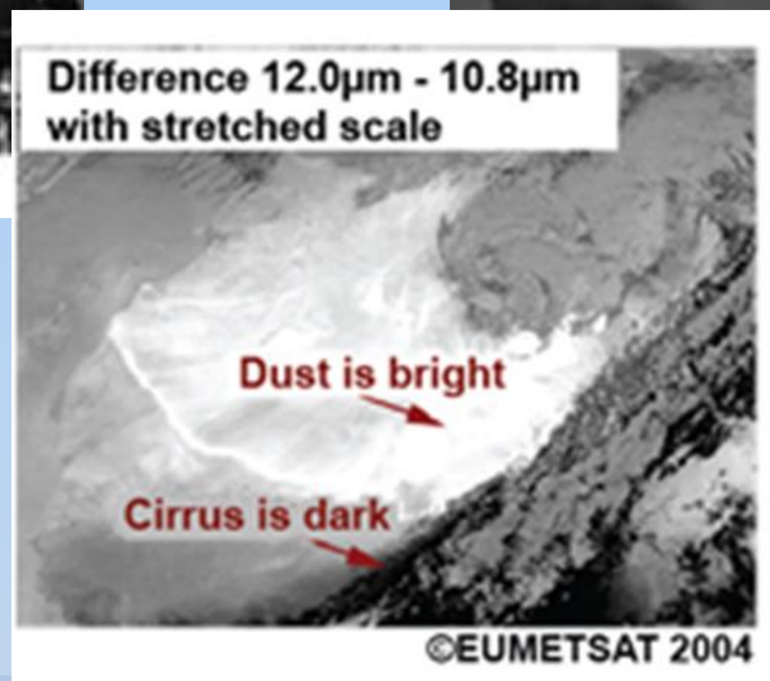

Figure 9.16 Images of Meteosat SEVIRI IR12.0, IR10.8, and IR12.0 - IR10.8 difference

African Monsoon Multidisciplinary Analysis

Chapter 9: *Remote Sensing* - Lead Author Arlene Laing, CIRA, Colorado State University

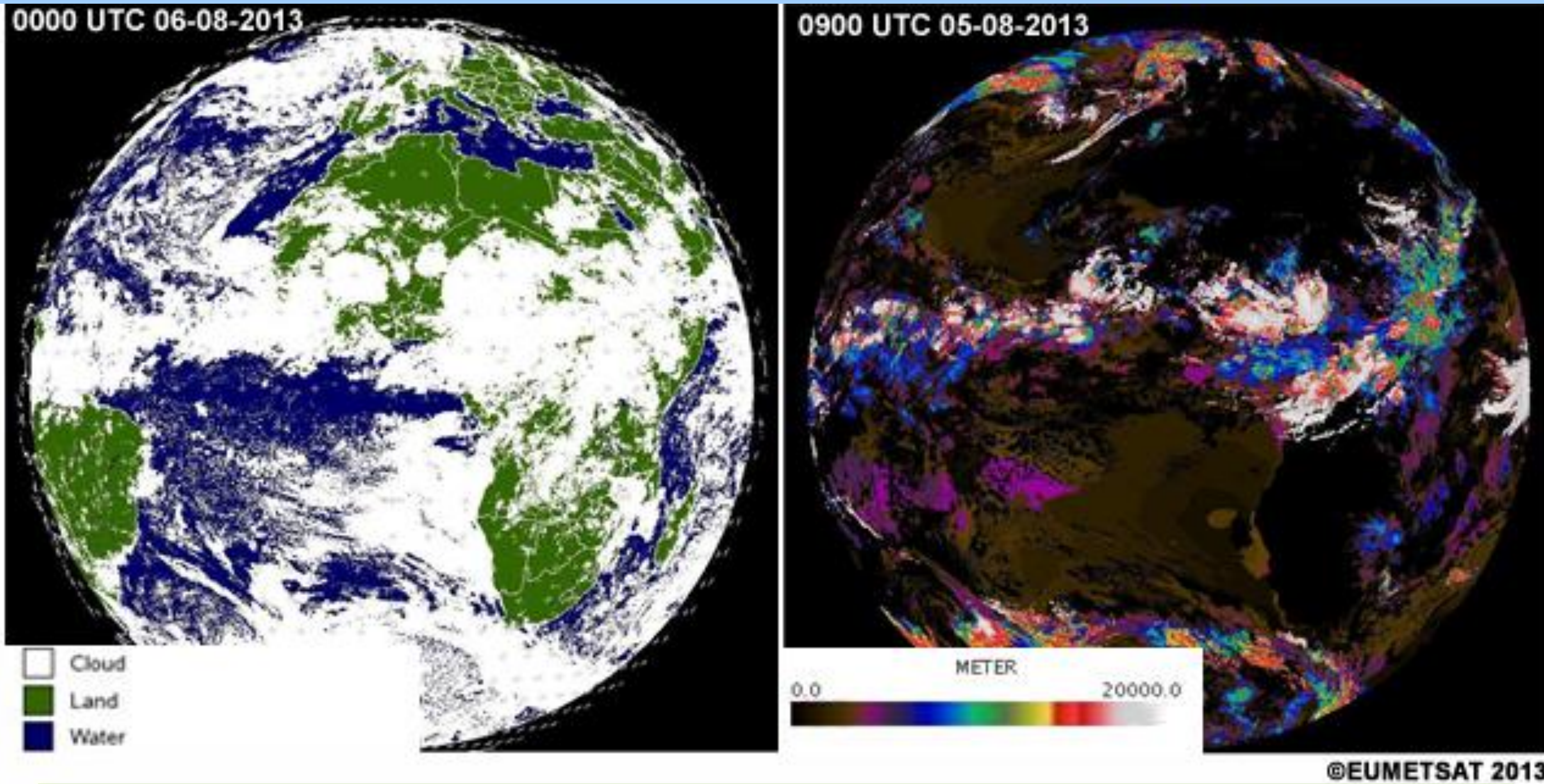

Figure 9.17. Cloud mask (left) and Cloud Top Height (right) products derived from quantitative extraction algorithms developed by the EUMETSAT Satellite Application Facilities Support to Nowcasting and Very Short Range Forecasting (SAFNWC).

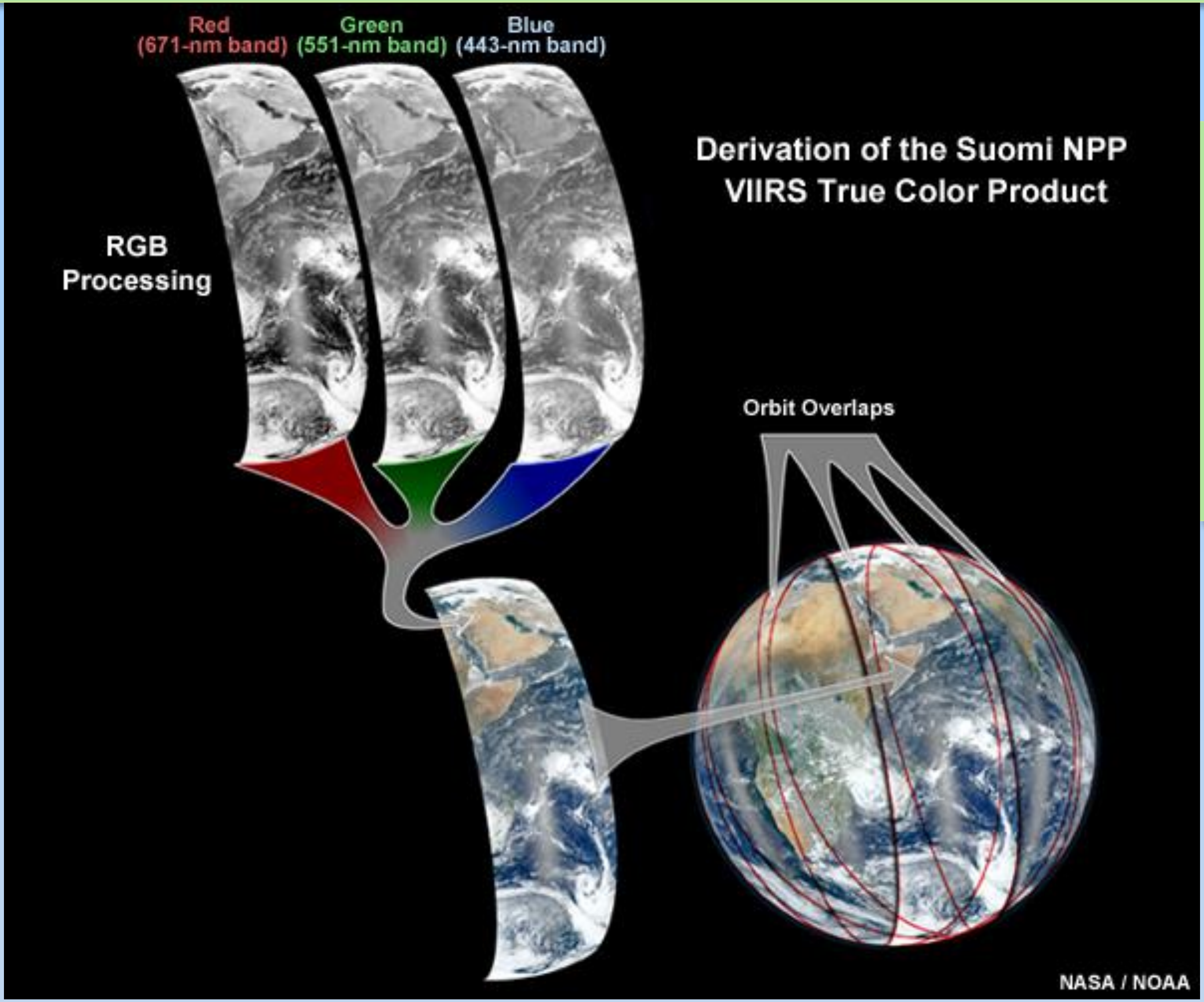

Figure 9.18. True colour image produced from RGB processing of data from the Suomi National Polar-orbiting Partnership (NPP) Visible Infrared Imaging Radiometer Suite (VIIRS).

Chapter 9: *Remote Sensing* - Lead Author Arlene Laing, CIRA, Colorado State University

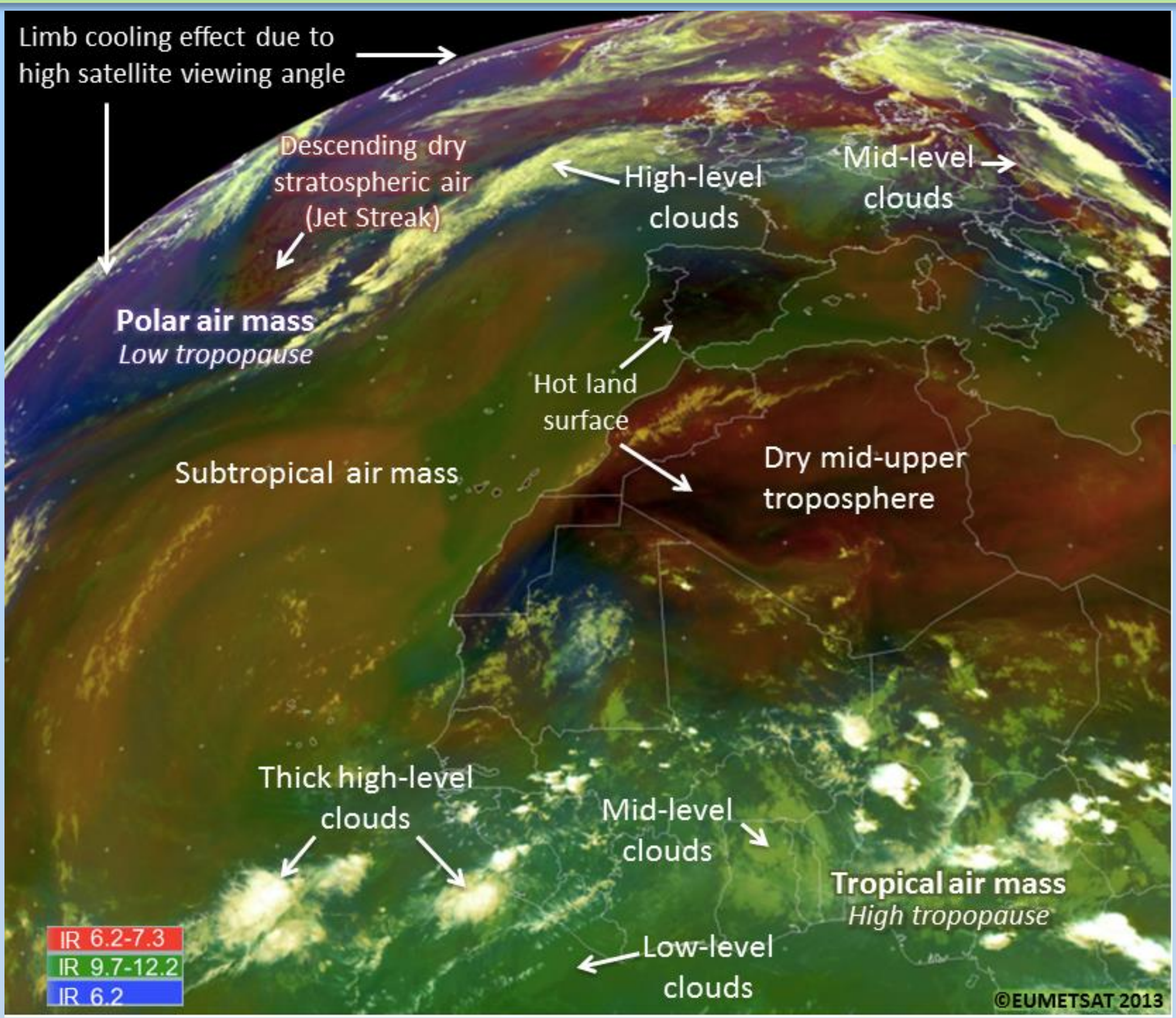

Figure 9.19a Airmass RGB image with interpretation of air masses and cloud levels. (EuMetrain/ © EUMETSAT 2013/ECMWF).

Chapter 9: *Remote Sensing* - Lead Author Arlene Laing, CIRA, Colorado State University

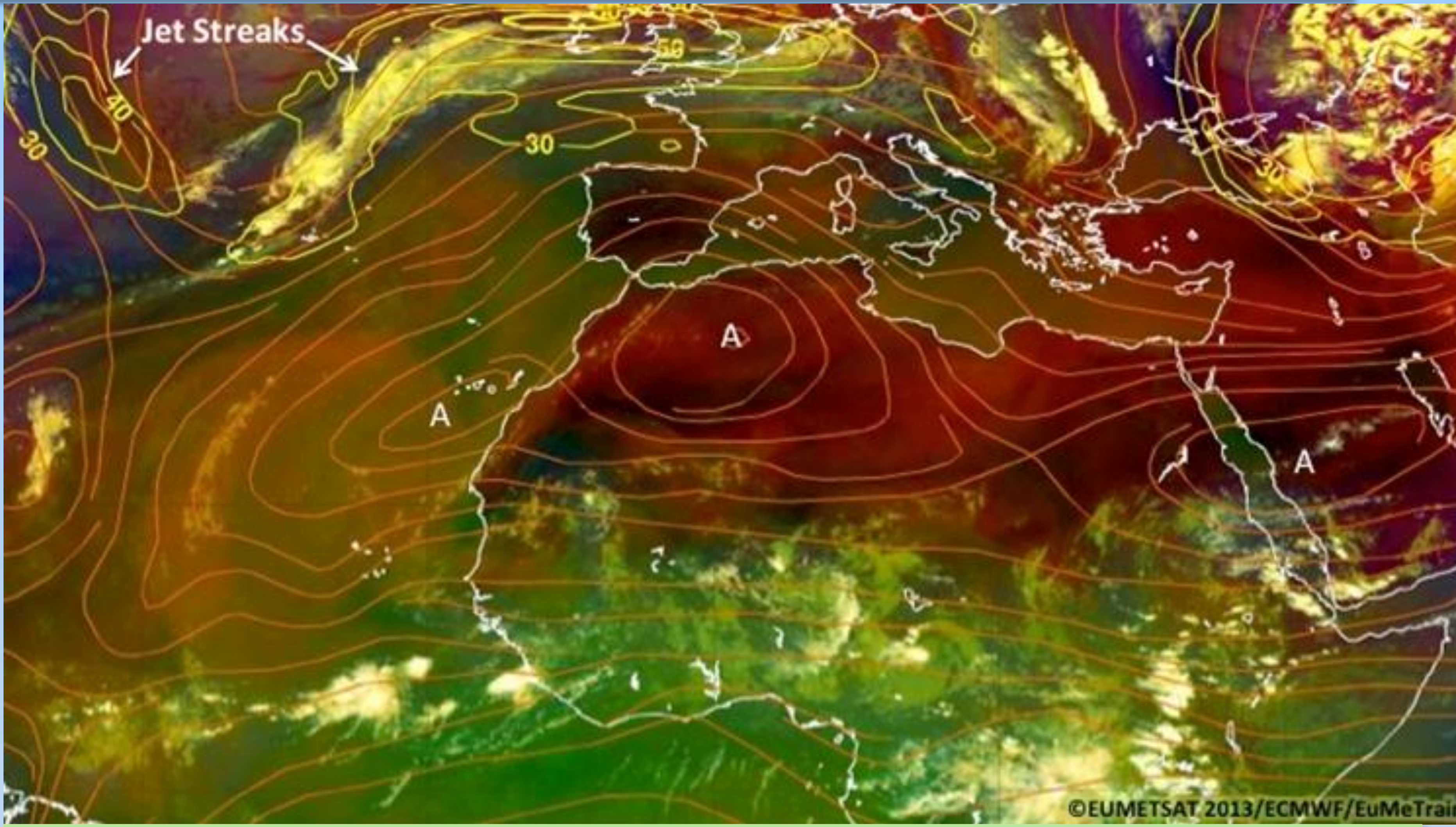

Figure 9.19b Airmass RGB image overlaid with streamlines (orange) and isotachs (yellow) at 300 hPa.

Chapter 9: *Remote Sensing* - Lead Author Arlene Laing, CIRA, Colorado State University

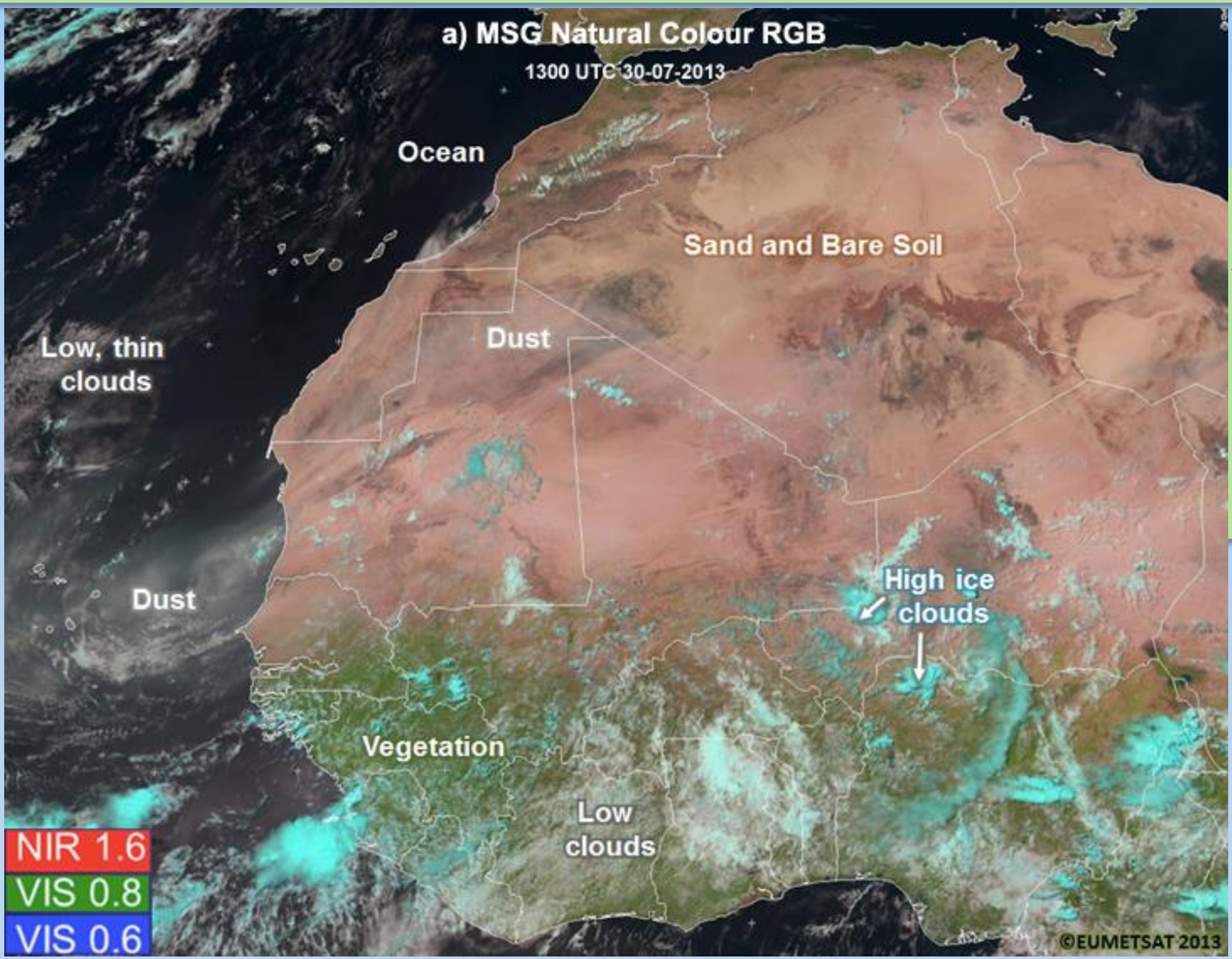

Figure 9.20a) Natural colour RGB image from the MSG SEVIRI (Upper) and True Colour RGB images from Moderate-resolution Imaging Spectroradiometer (MODIS)

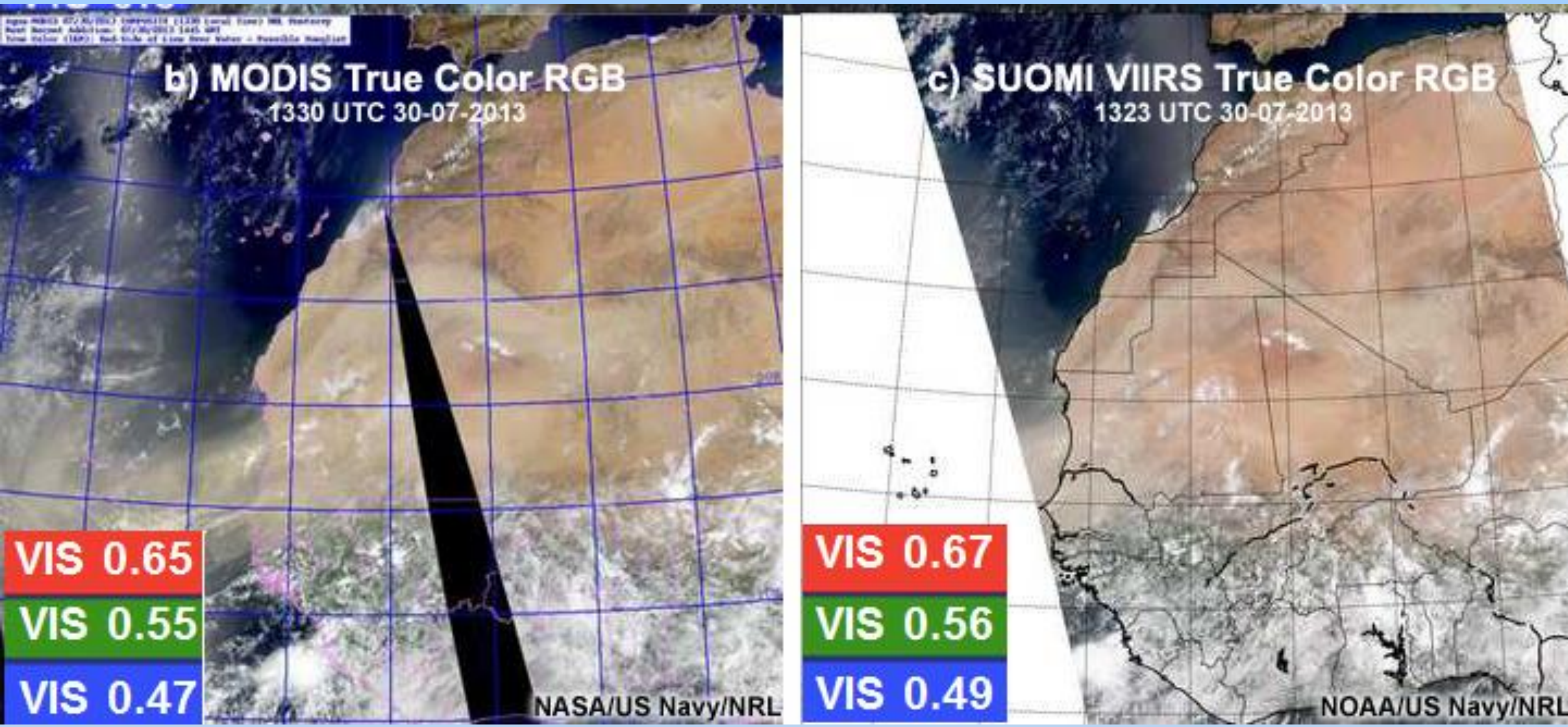

Figure 9.20b) and c) Natural colour RGB image from the MSG SEVIRI (Upper) and True Colour RGB images from Moderate-resolution Imaging Spectroradiometer (MODIS) Aqua (left) and Suomi-NPP VIIRS (right)

Chapter 9: *Remote Sensing* - Lead Author Arlene Laing, CIRA, Colorado State University

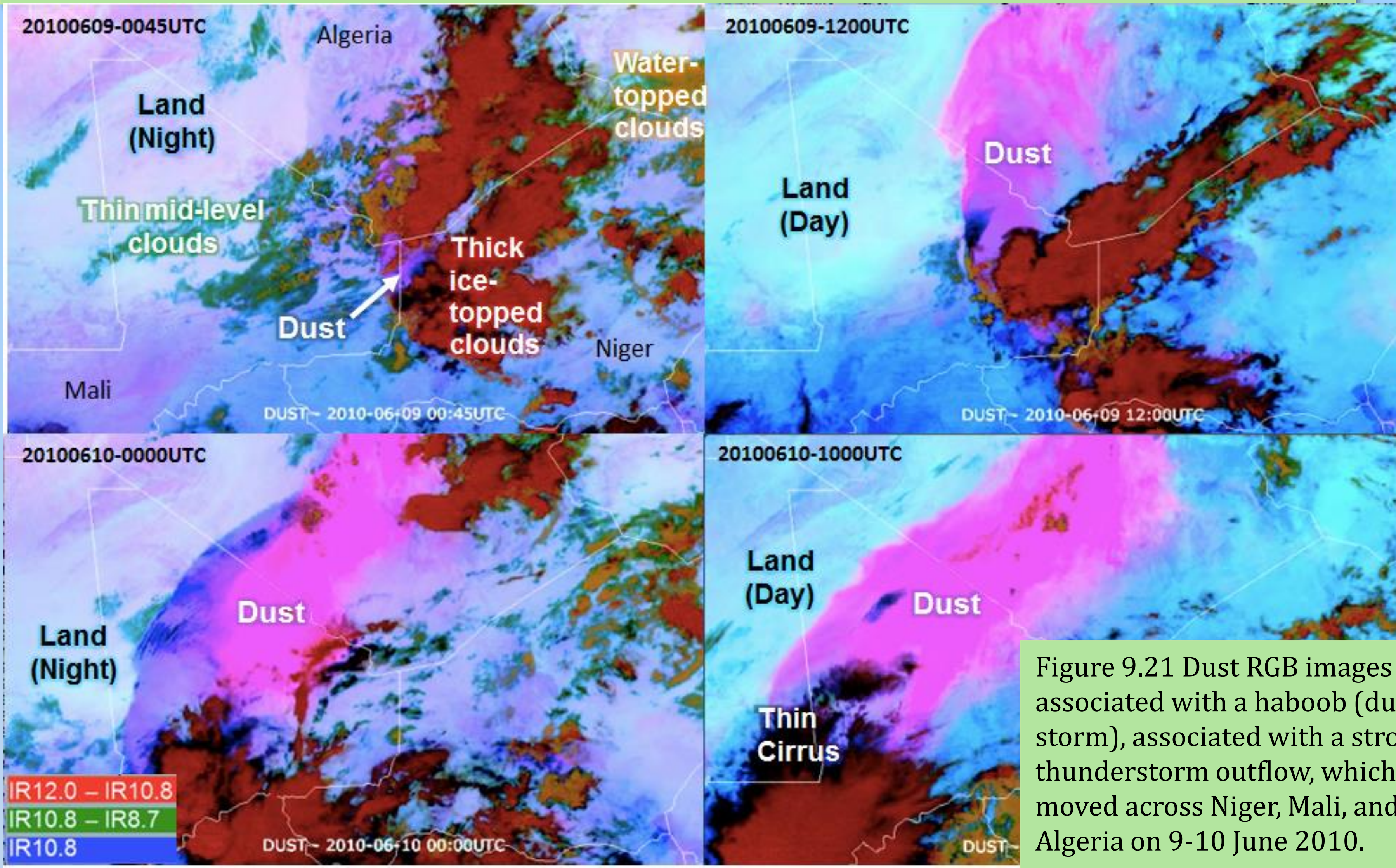

Figure 9.21 Dust RGB images associated with a haboob (dust storm), associated with a strong thunderstorm outflow, which moved across Niger, Mali, and Algeria on 9-10 June 2010.

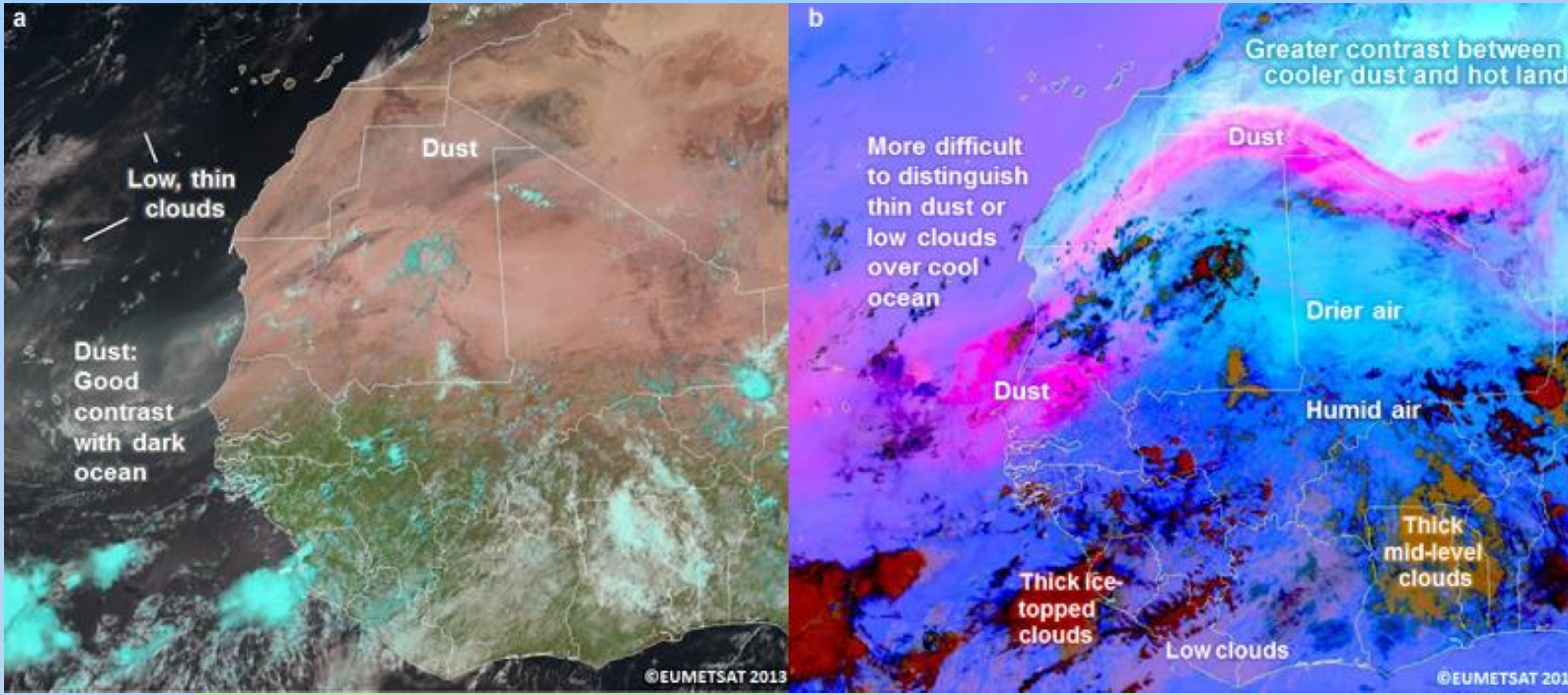

Figure 9.22. Dust over West Africa detected by (a) Natural Colour RGB and (b) Dust RGB

Chapter 9: *Remote Sensing* - Lead Author Arlene Laing, CIRA, Colorado State University

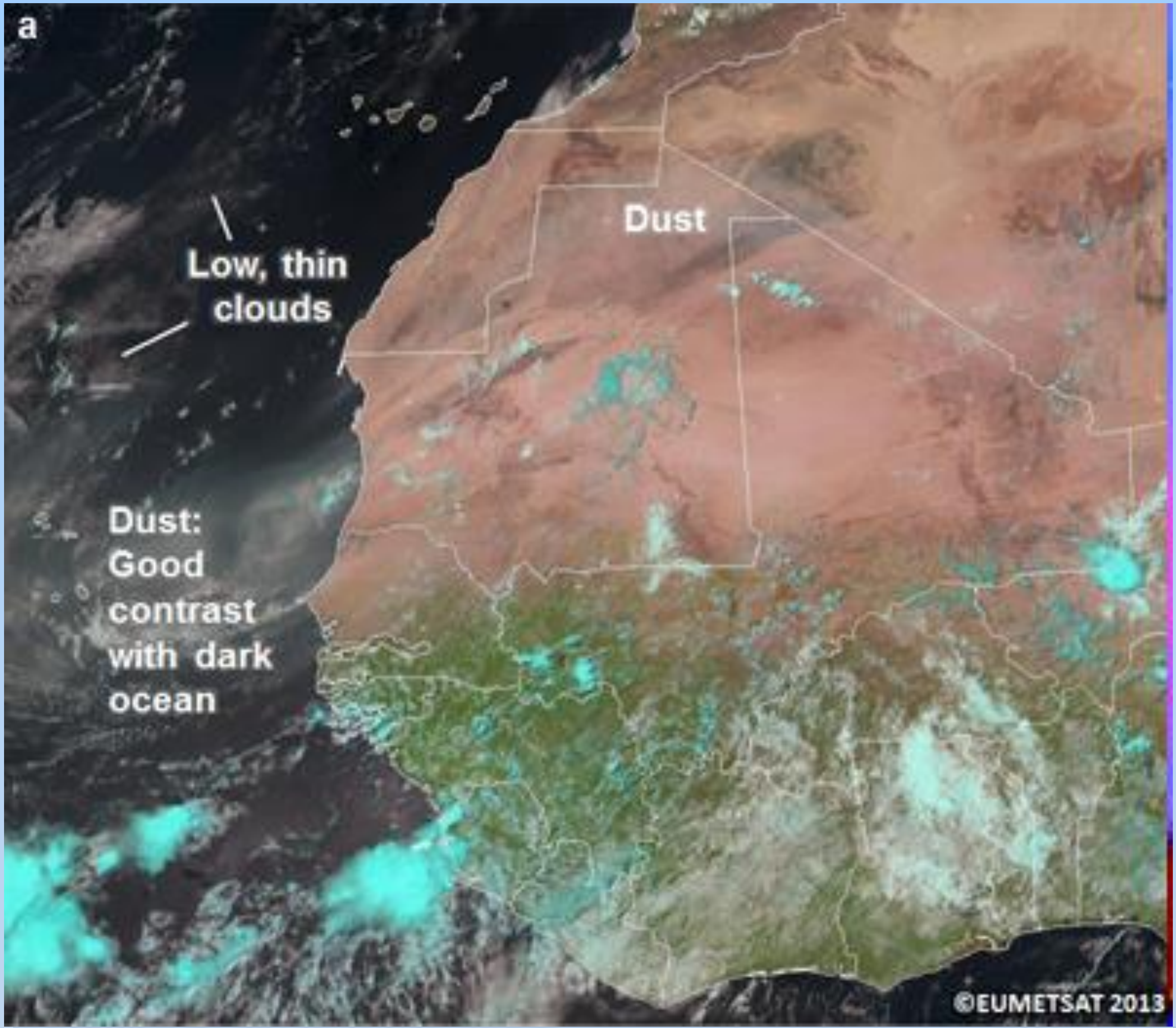

Figure 9.22a) Dust over West Africa detected by Natural Colour RGB.

Chapter 9: *Remote Sensing* - Lead Author Arlene Laing, CIRA, Colorado State University

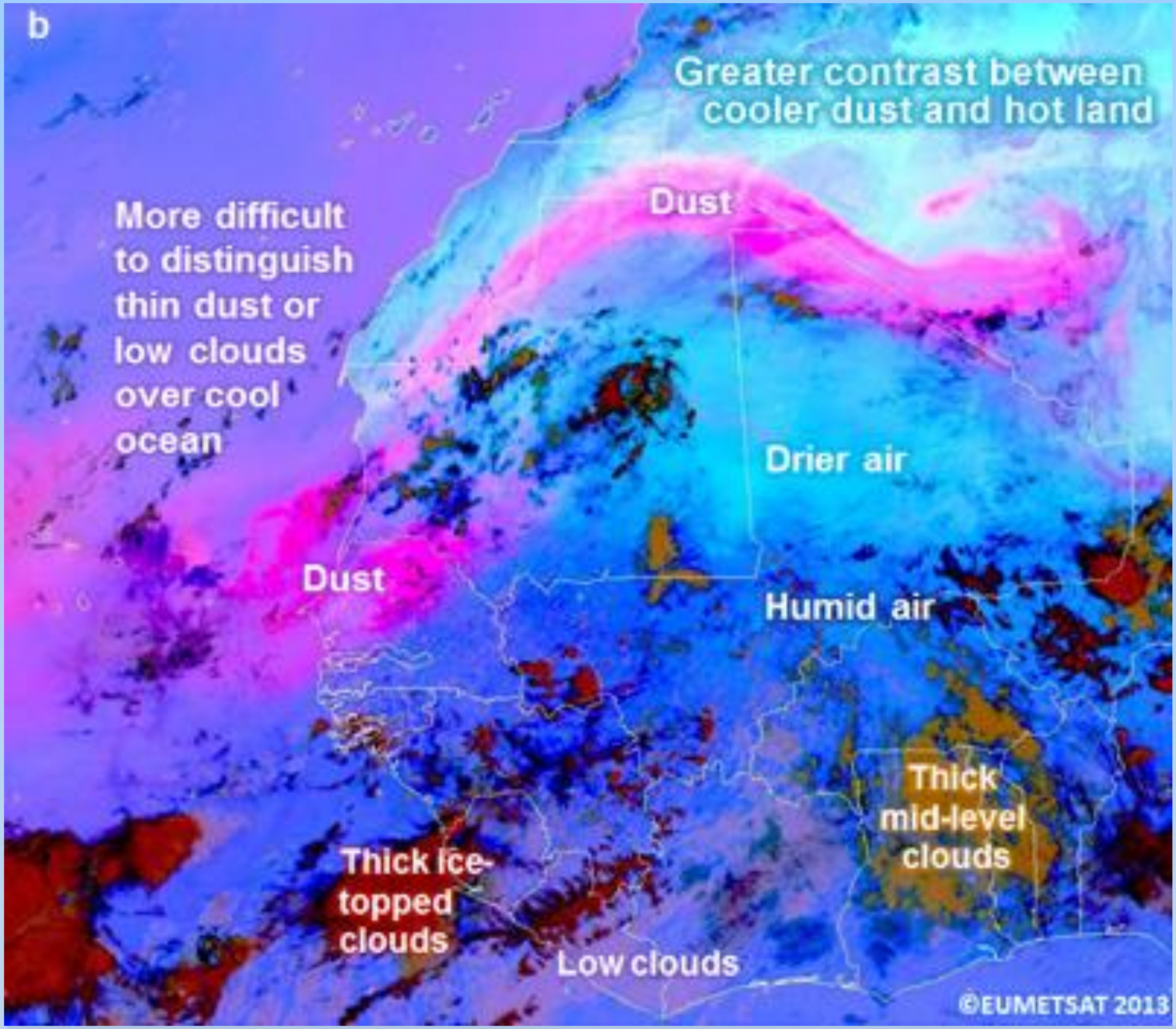

Figure 9.22b) Dust over West Africa detected by dust RGB

Chapter 9: *Remote Sensing* - Lead Author Arlene Laing, CIRA, Colorado State University

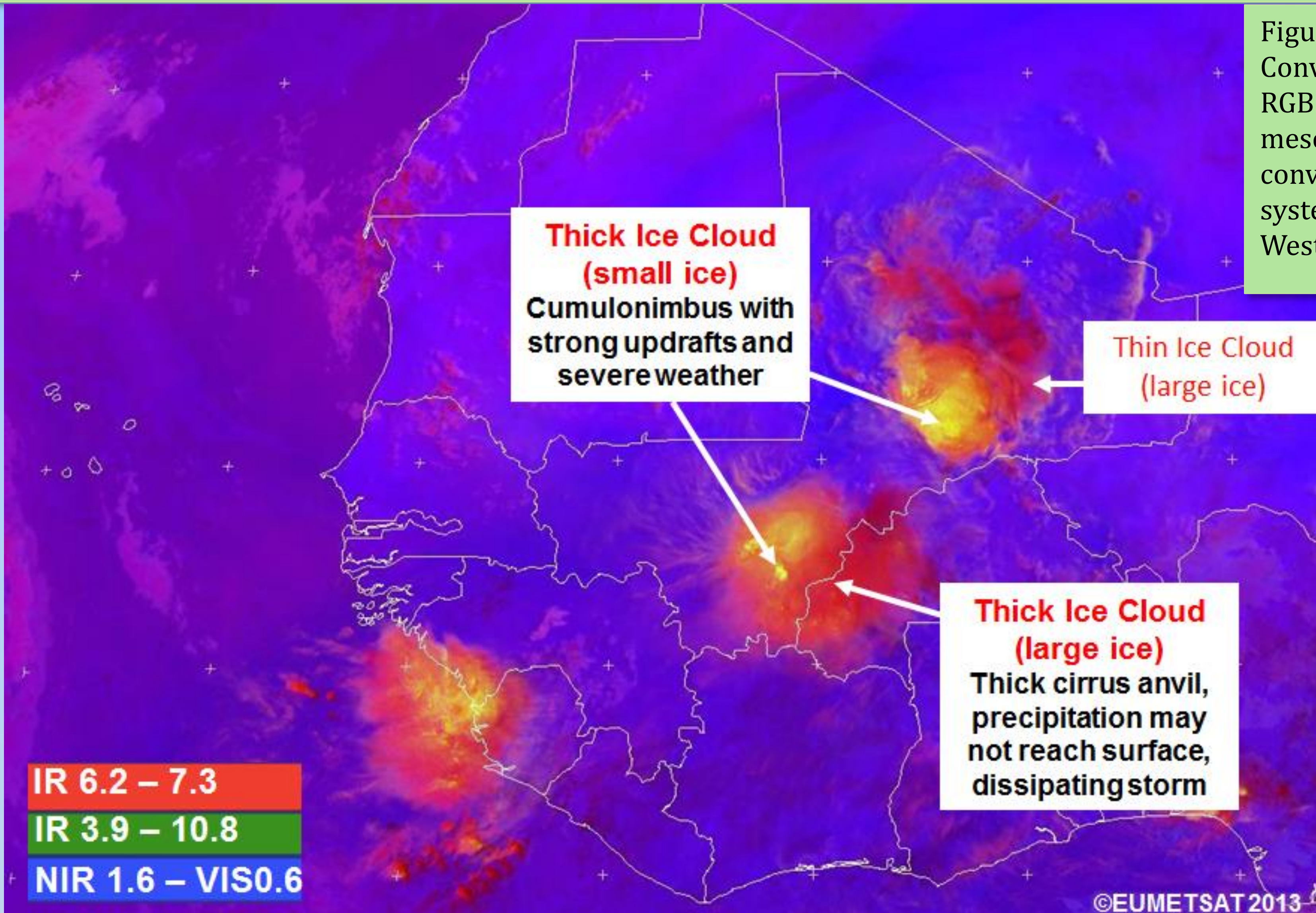

Figure 9.23. Convective RGB image of mesoscale convective systems over West Africa.

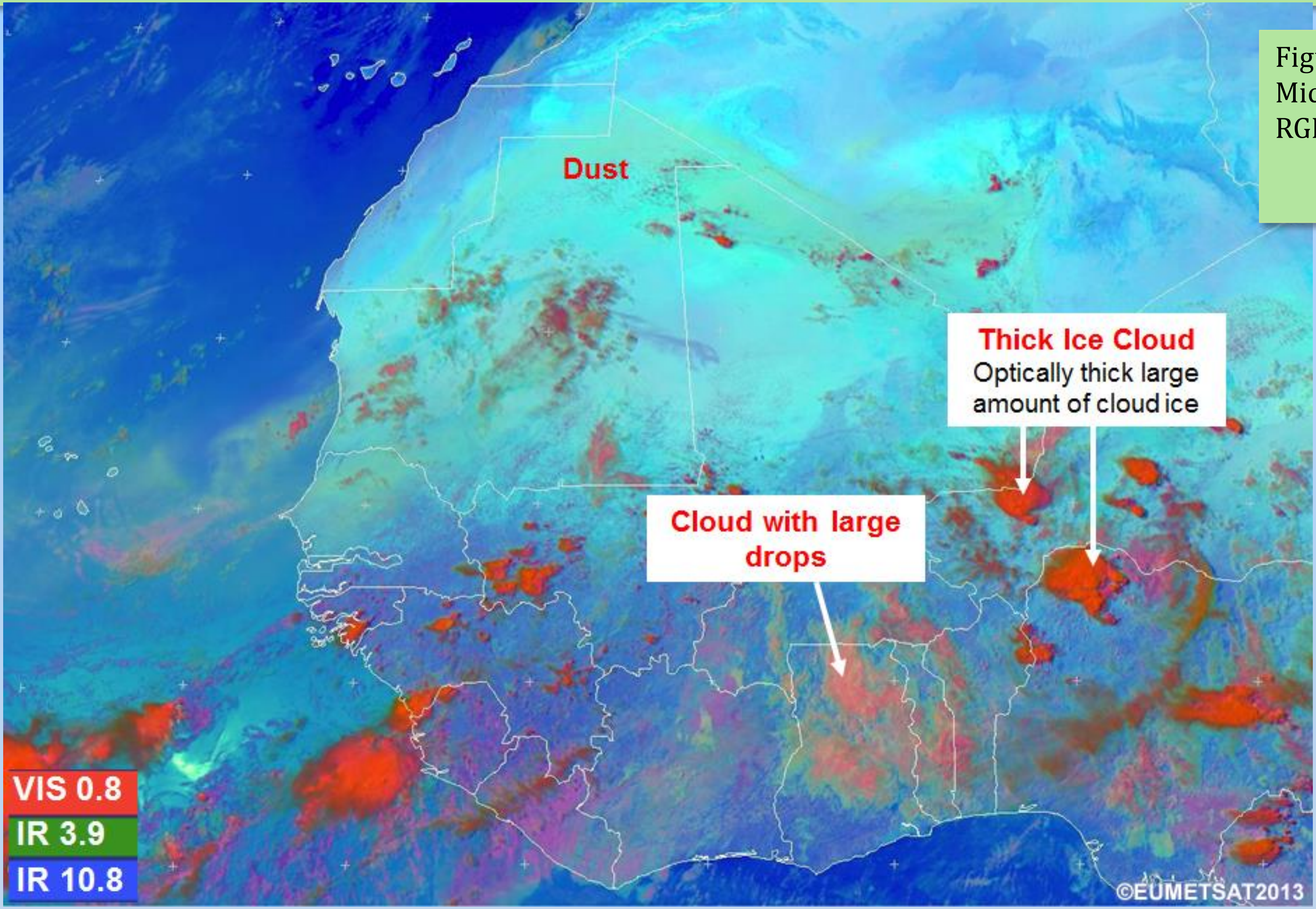

Figure 9.24 Day Microphysics RGB image

Chapter 9: *Remote Sensing* - Lead Author Arlene Laing, CIRA, Colorado State University

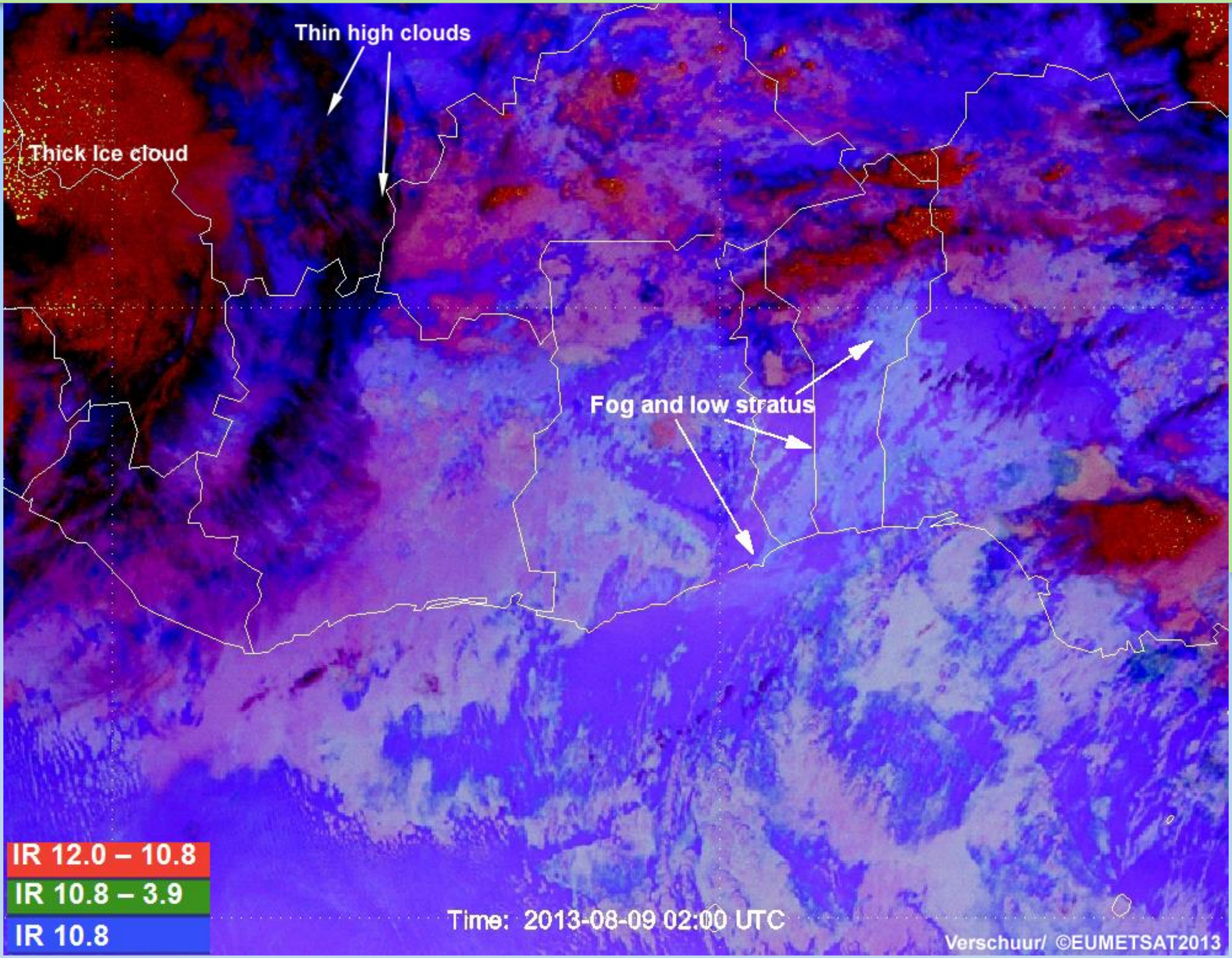

Figure 9.25. Fog and low stratus near the coast of the Gulf of Guinea. Thunderstorms near the west coast of Africa are bordered by thin cirrus outflow (Courtesy of Henk Verschuur).

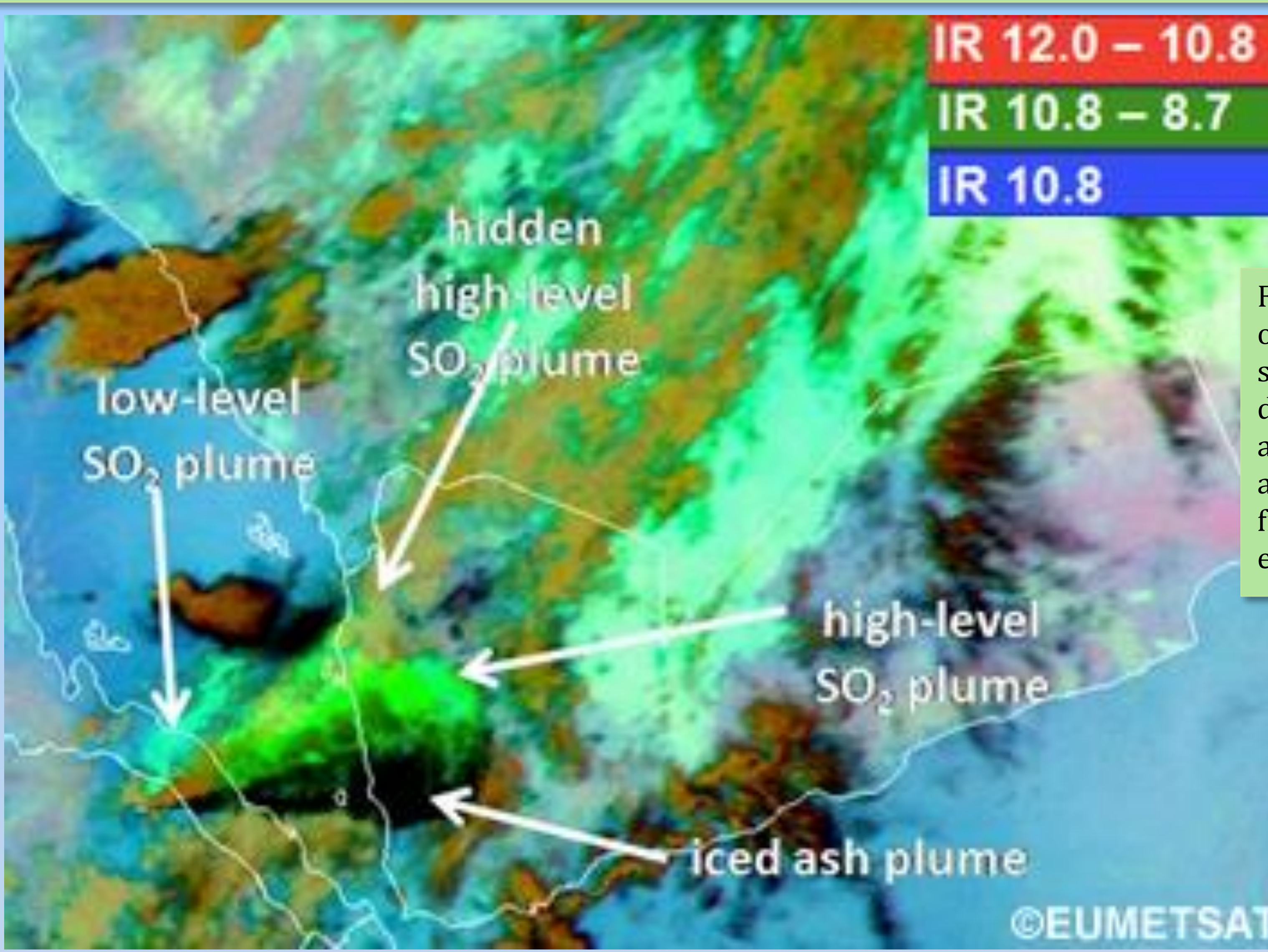

Figure 9.26. Example of Ash RGB image showing sulphur dioxide (SO2) plumes at different levels and an iced ash plume from volcanic eruption in Ethiopia.

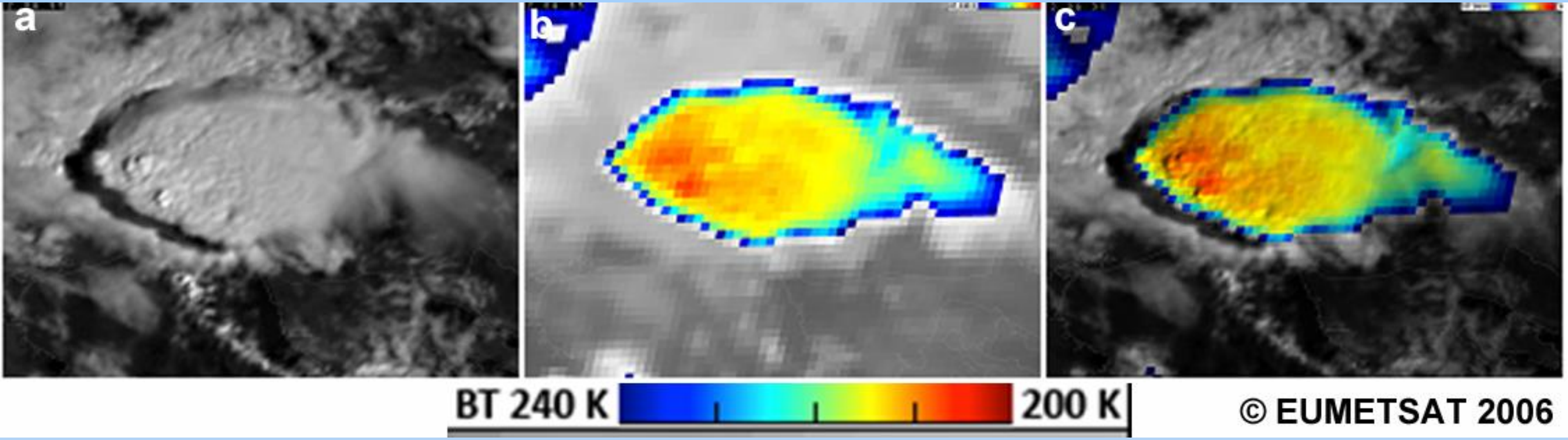

Figure 9.27 MSG-3 (a) visible, (b) colour-enhanced IR10.8 μm brightness temperature, and (c) sandwich product of the visible and IR images highlighting the overshooting tops of a supercell thunderstorm over Italy.

Chapter 9: *Remote Sensing* - Lead Author Arlene Laing, CIRA, Colorado State University

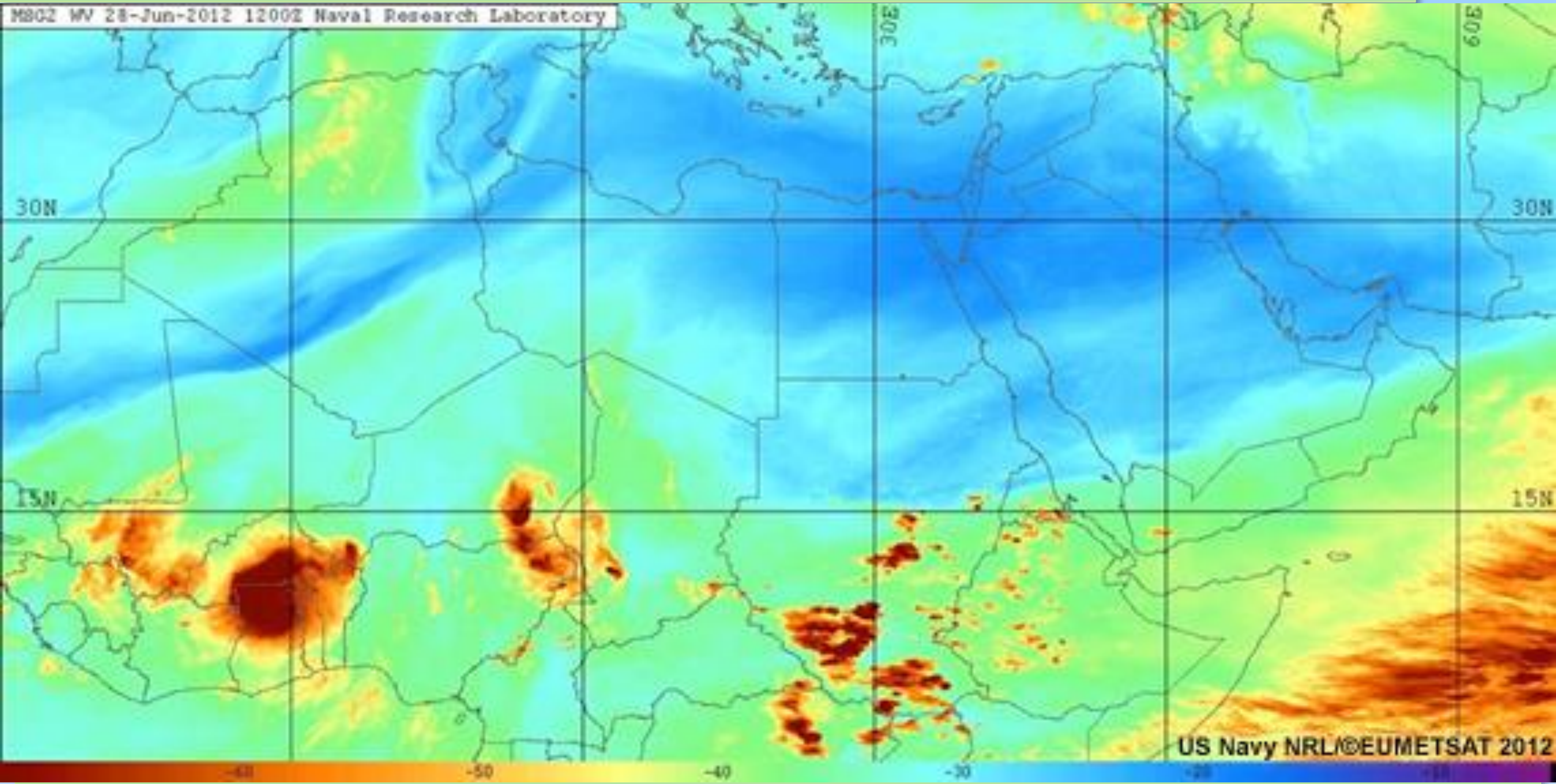

Figure 9.28 Example of colour enhanced IR water vapour image for northern Africa; dark red areas indicate high water vapour content in the mid-upper troposphere and blue to violet areas show the dry mid-upper troposphere.

Chapter 9: *Remote Sensing* - Lead Author Arlene Laing, CIRA, Colorado State University

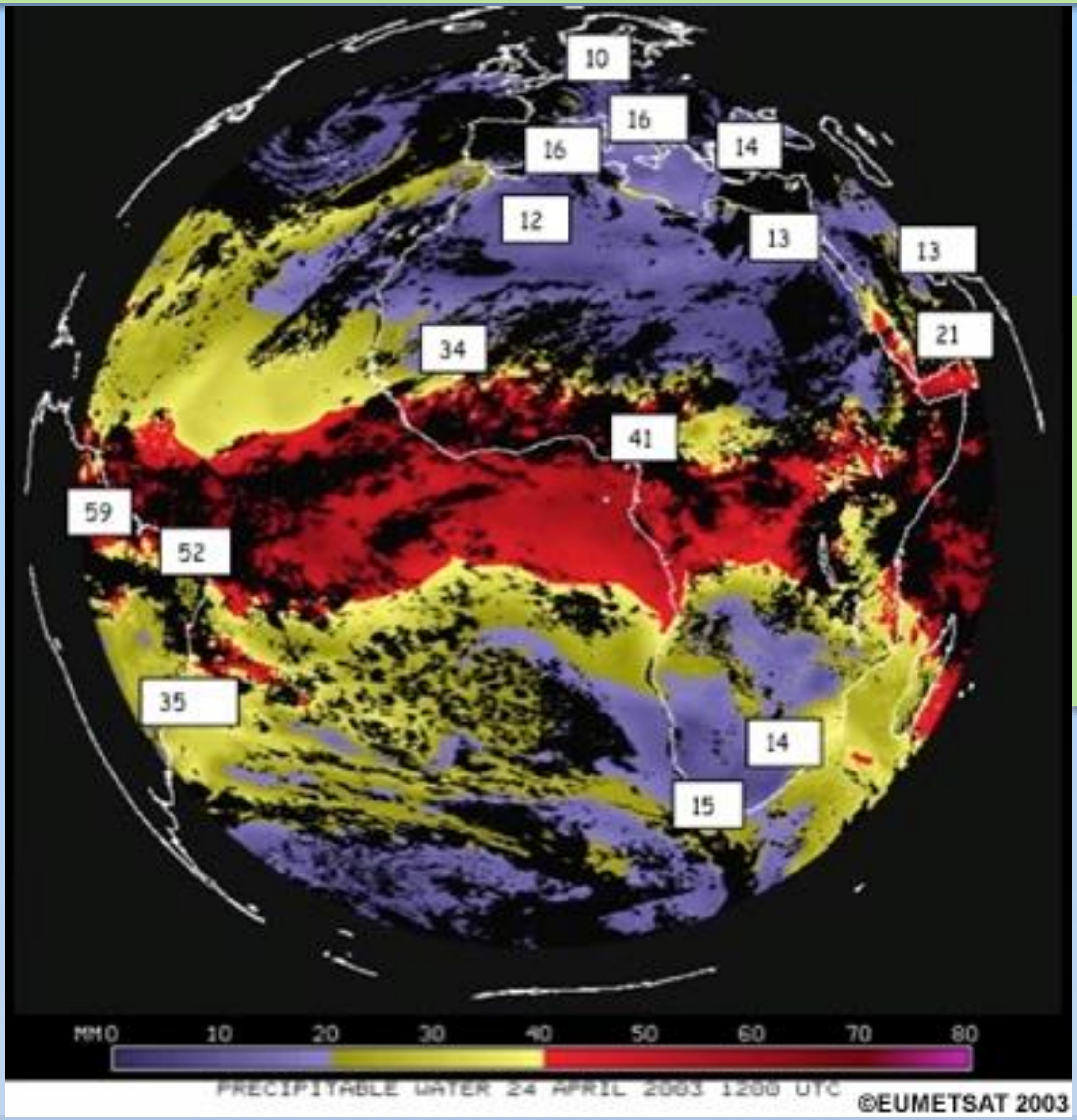

Figure 9.29 Precipitable water product derived from MSG SEVIRI. Boxed values are precipitable water from soundings. (Courtesy, EUMETSAT)

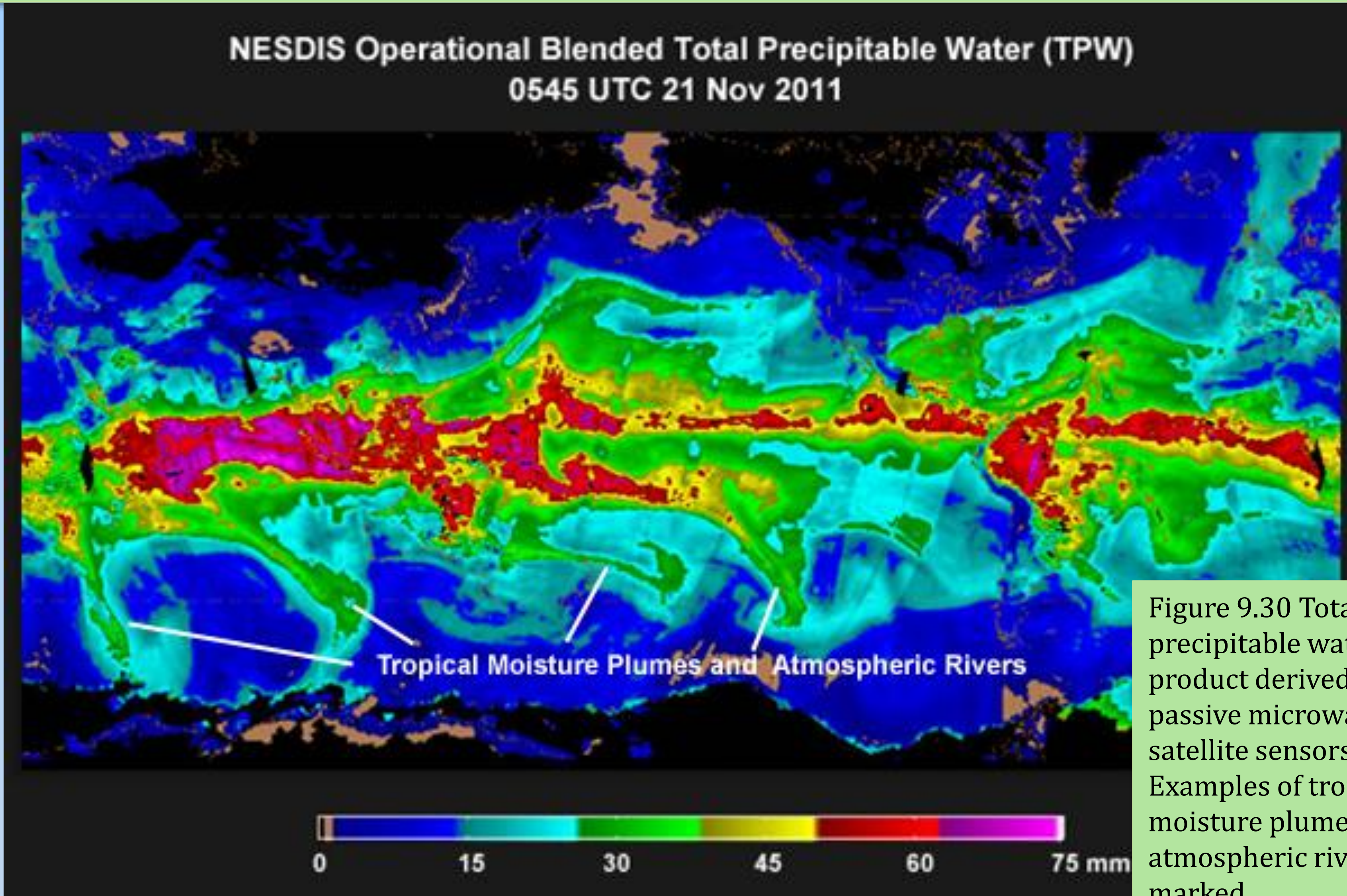

Figure 9.30 Total precipitable water vapour product derived from passive microwave satellite sensors. Examples of tropical moisture plumes and atmospheric rivers are marked.

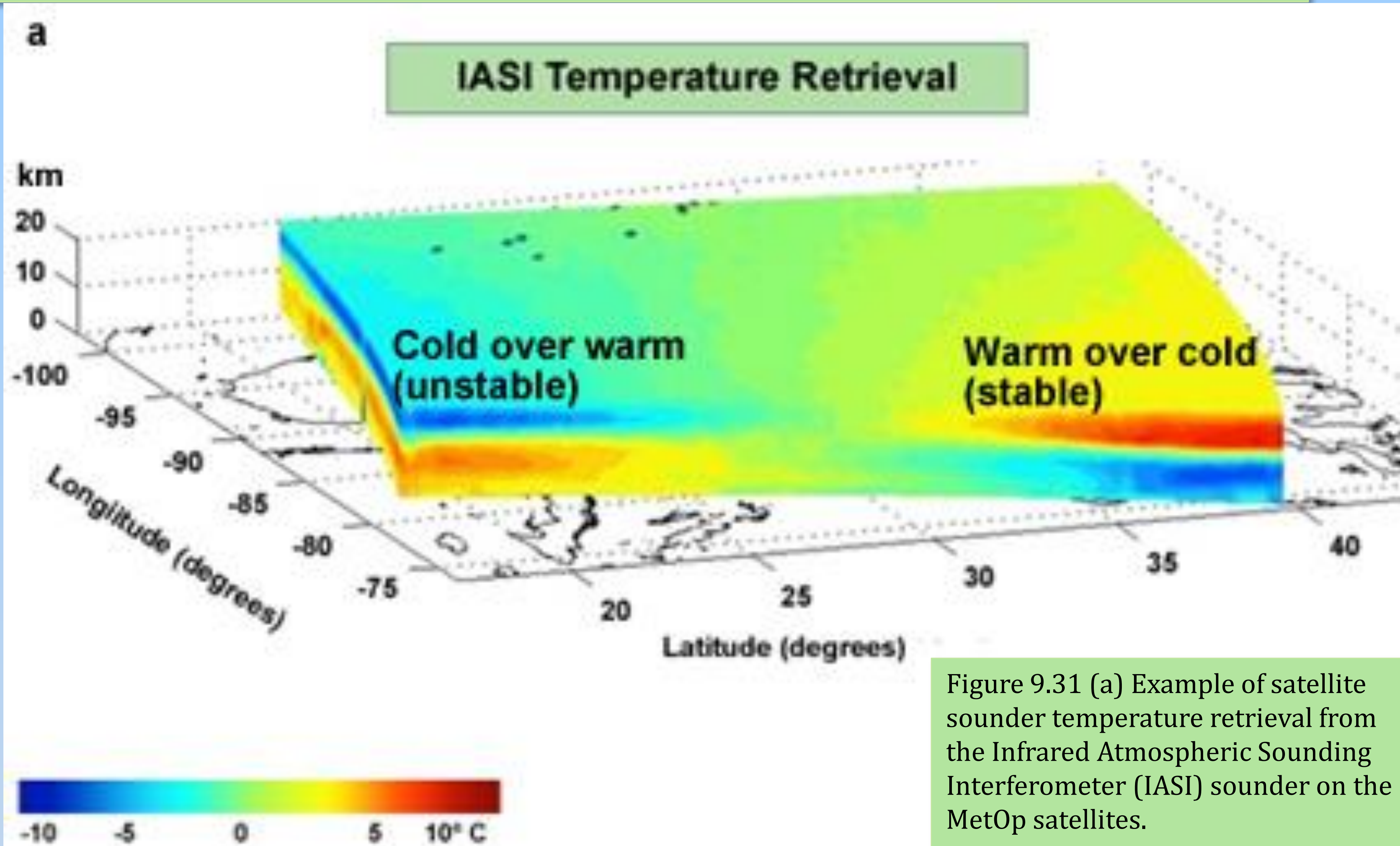

Figure 9.31 (a) Example of satellite sounder temperature retrieval from the Infrared Atmospheric Sounding Interferometer (IASI) sounder on the MetOp satellites.

Chapter 9: ***Remote Sensing*** **- Lead Author Arlene Laing, CIRA, Colorado State University**

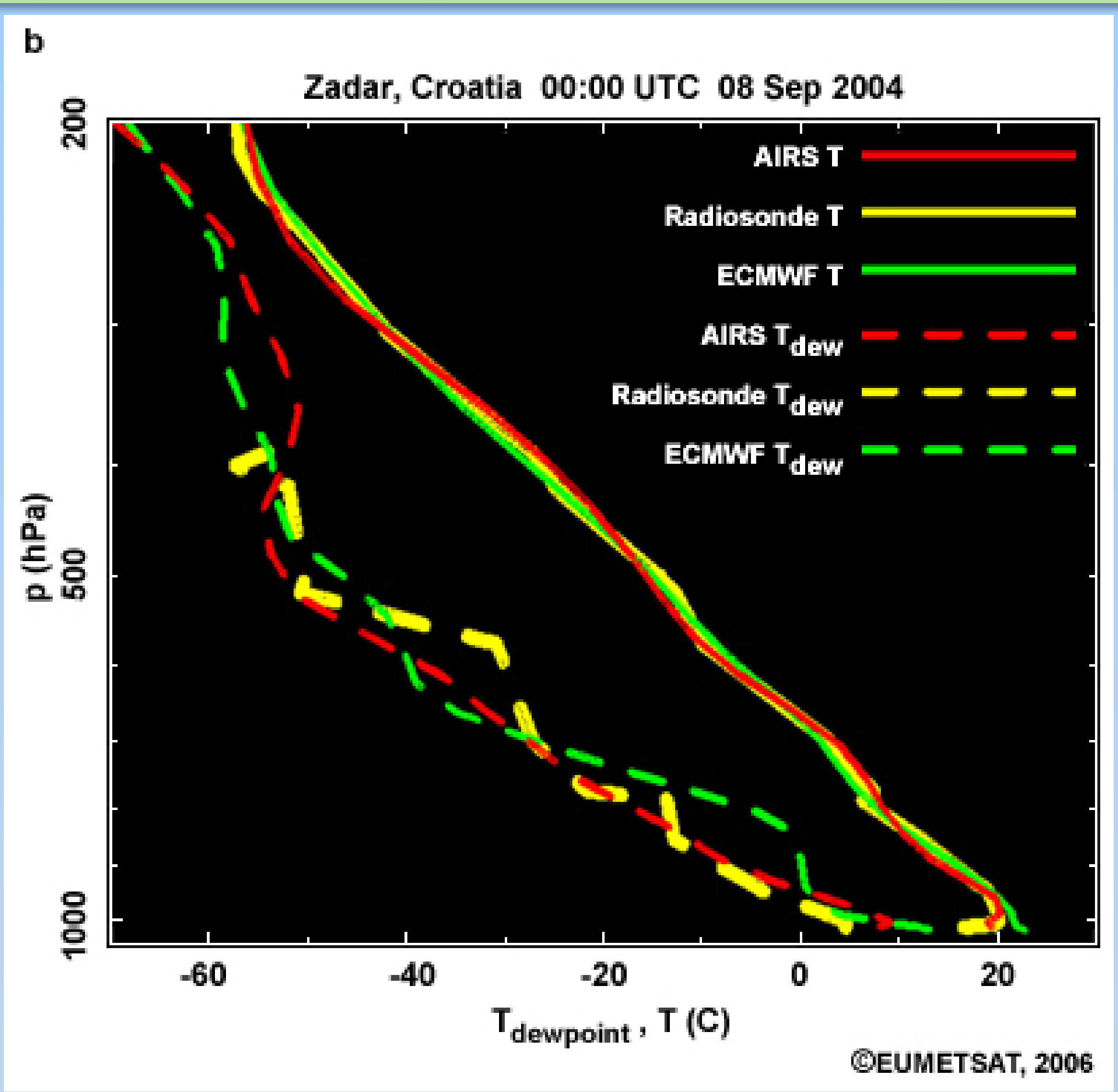

Figure 9.31 b) Skew-T log-P plot of temperature and dew point from the NASA Atmospheric IR Sounder (AIRS), radiosonde, and ECWMF analysis for clear sky over Zadar, Croatia.

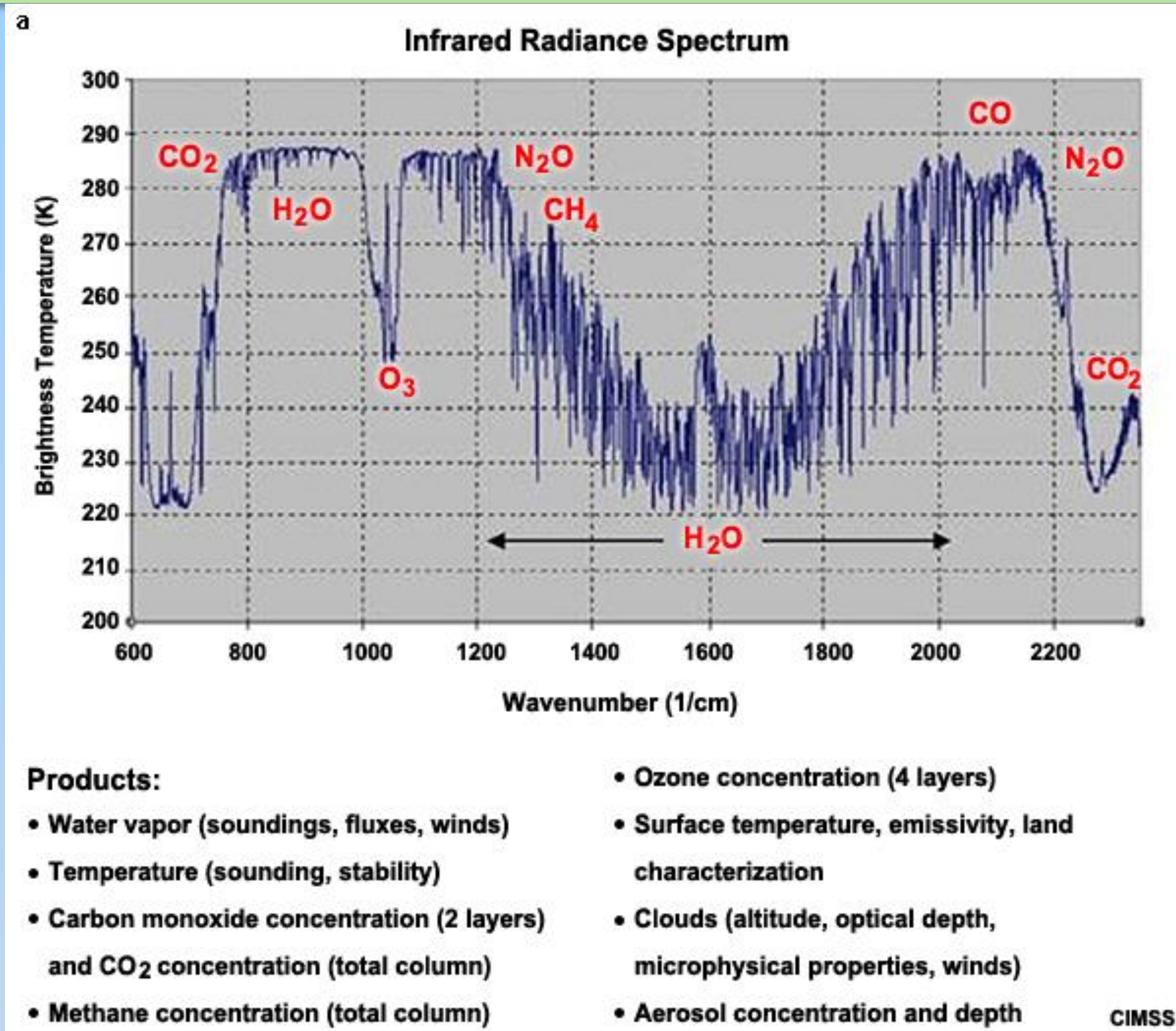

Figure 9.32 (a) IR radiance spectrum, bands that interact with specific gases, and products retrieved by satellite sounders to monitor the surface and the atmospheric column above.

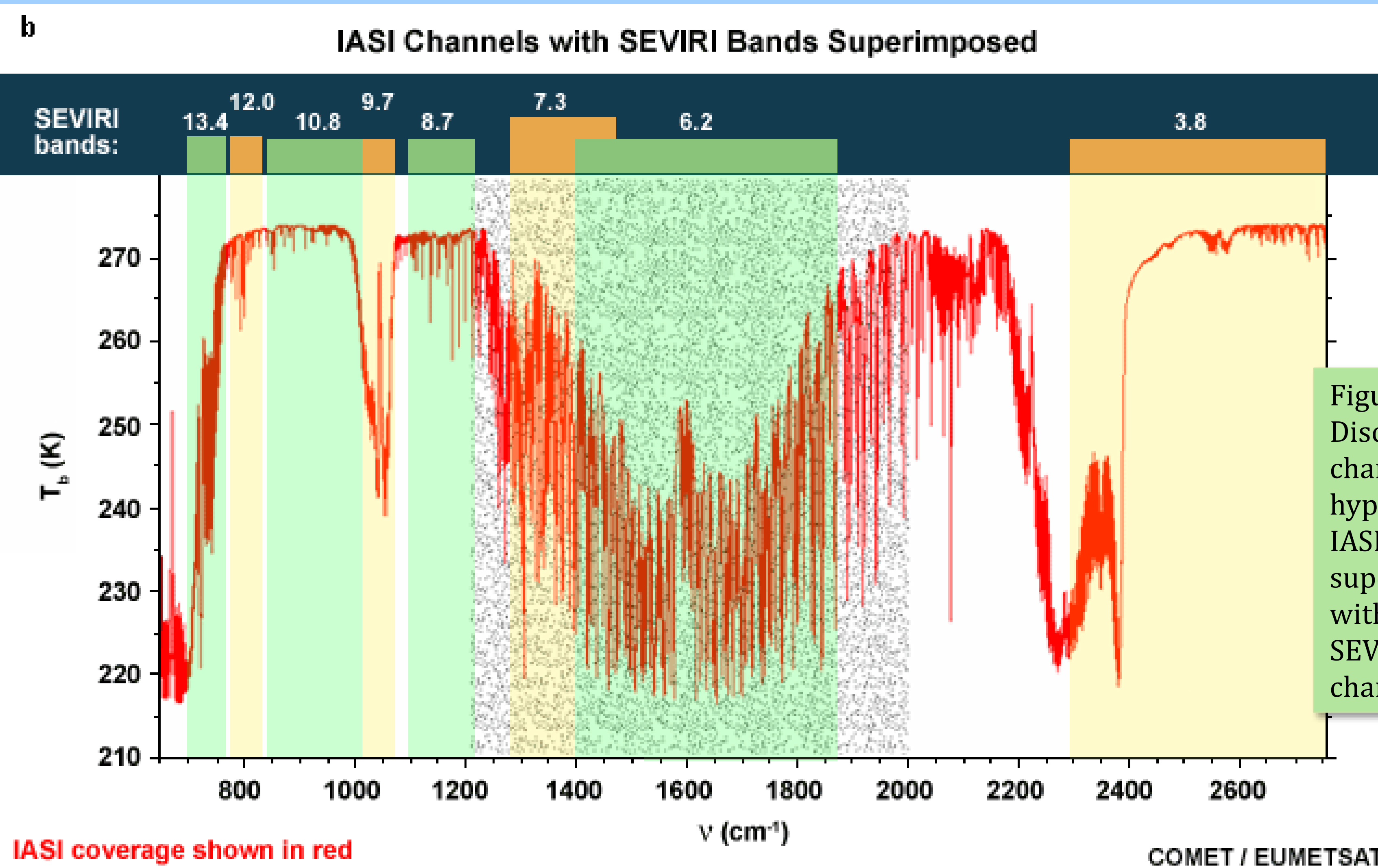

Figure 9.32 (b) Discrete channels of the hyperspectral IASI sounder superimposed with the MSG SEVIRI channels.

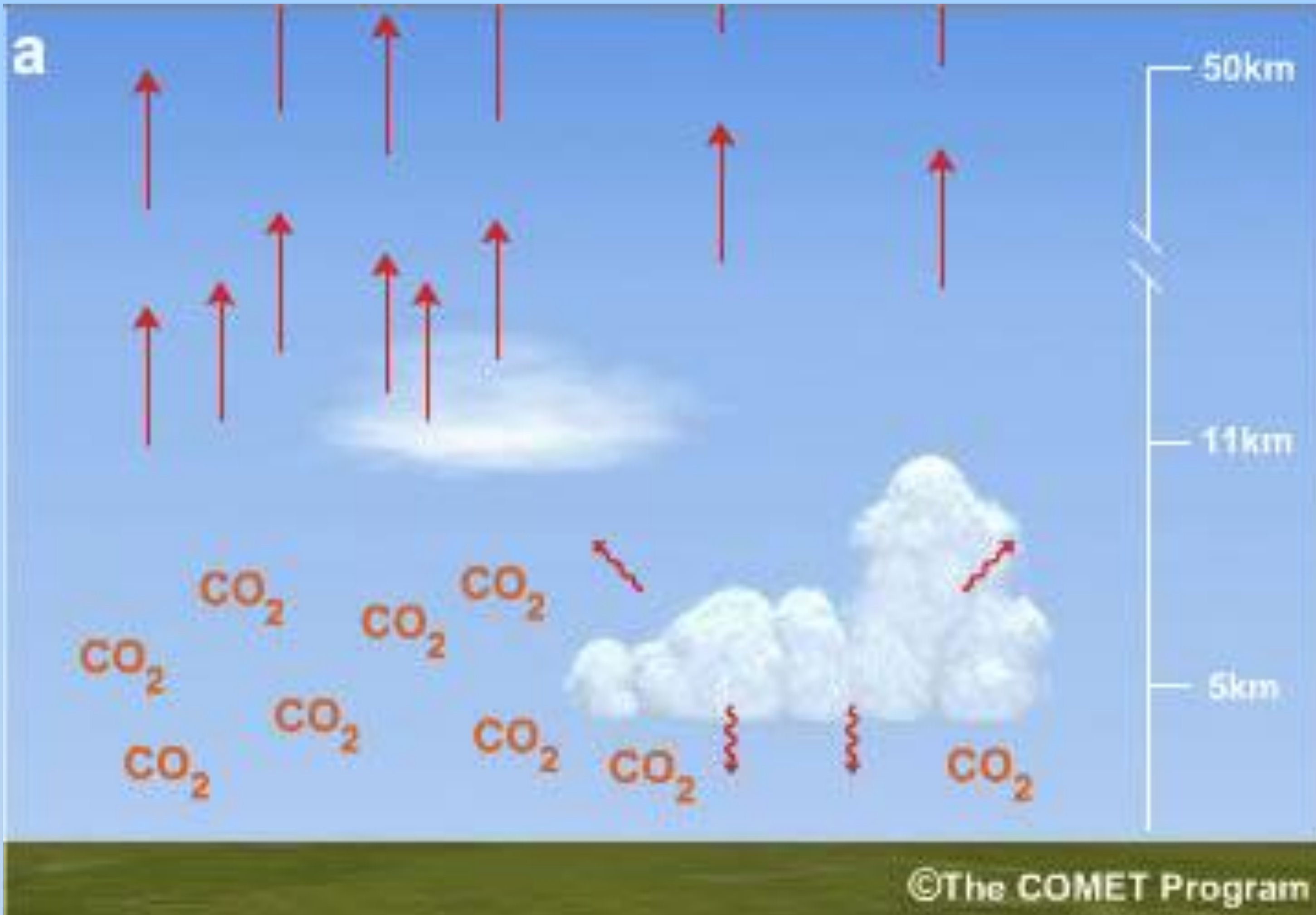

Figure 9.33 (a) Schematic of emission of CO2 at 13.3μm wavelength, which is more dominant near the surface.

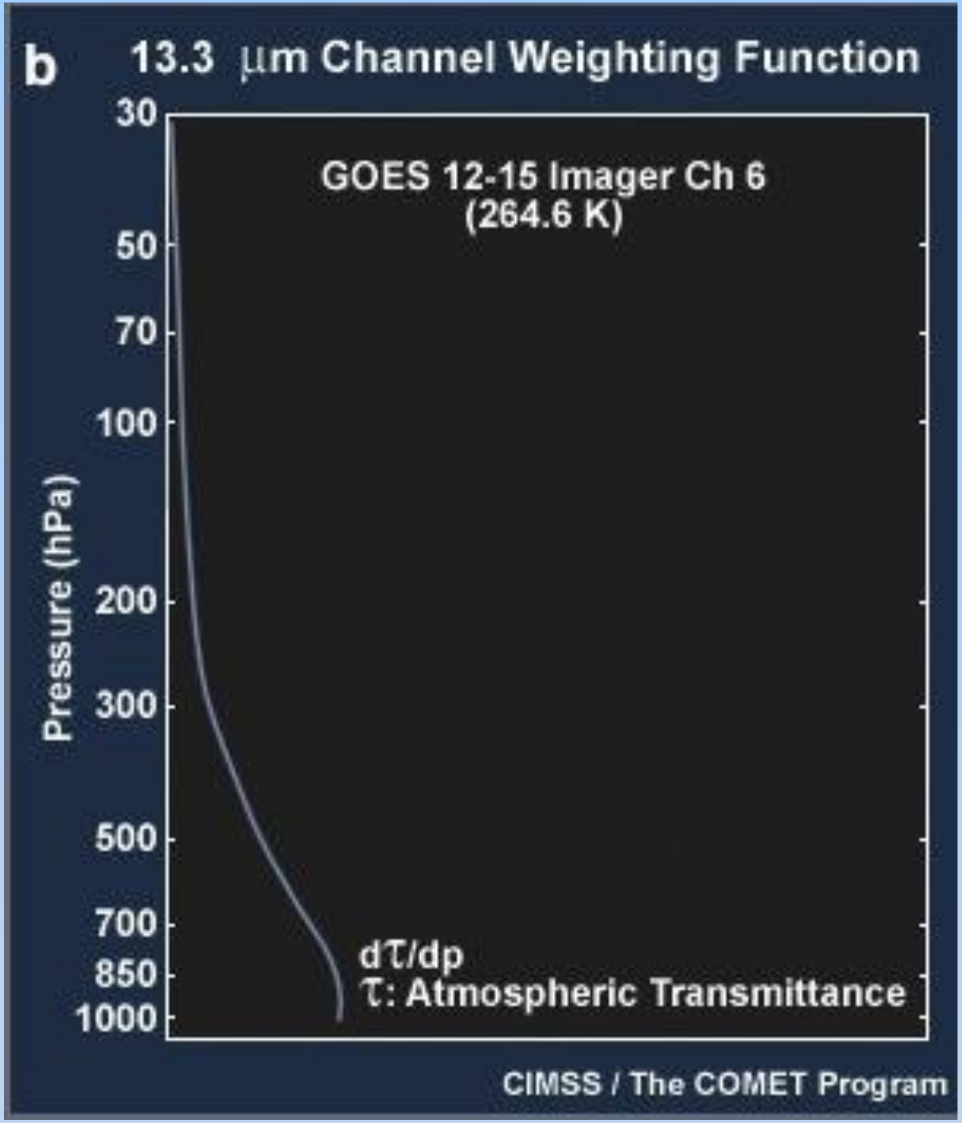

Figure 9.33 (b) the corresponding weight function for that spectral band.

Chapter 9: *Remote Sensing* - Lead Author Arlene Laing, CIRA, Colorado State University

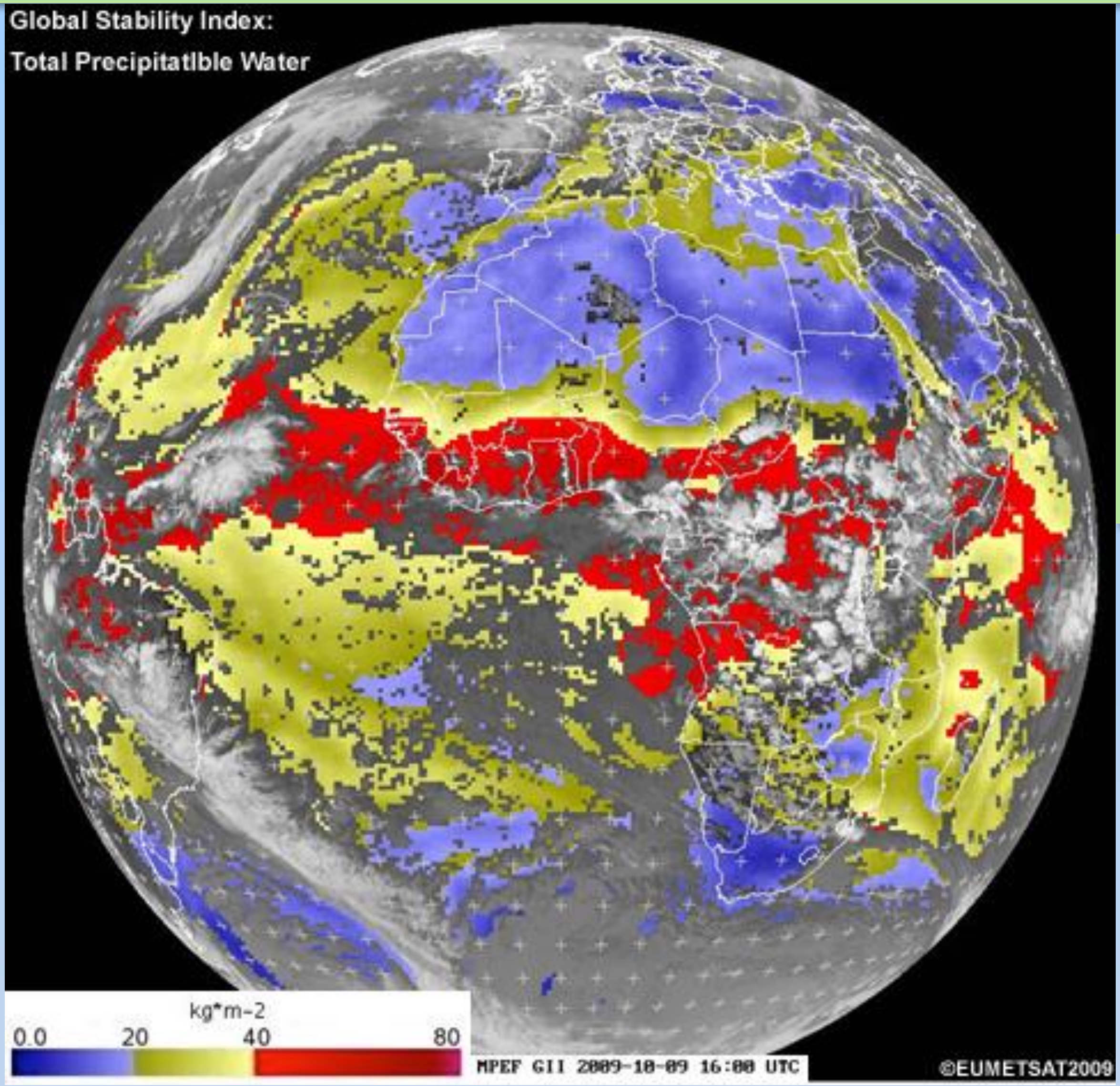

Figure 9.34. Meteosat total precipitable water (TPW), a global stability index derived empirically for cloud free areas and used to identify convective potential (©EUMETSAT 2009).

Chapter 9: *Remote Sensing* - Lead Author Arlene Laing, CIRA, Colorado State University

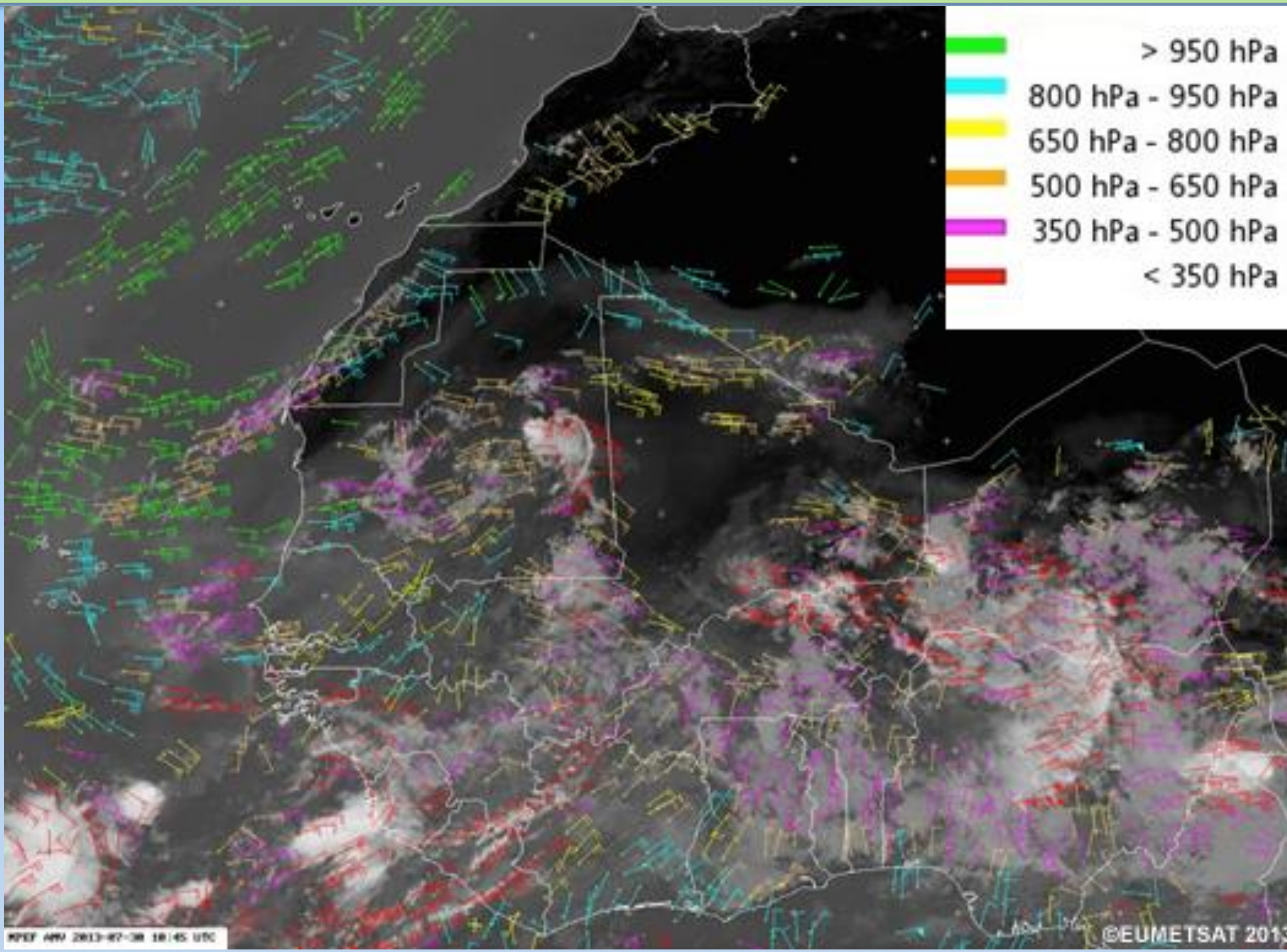

Figure 9.35 Atmospheric Motion Vectors (AMV) for various layers in the atmosphere derived from geostationary imagery. (©EUMETSAT 2013)

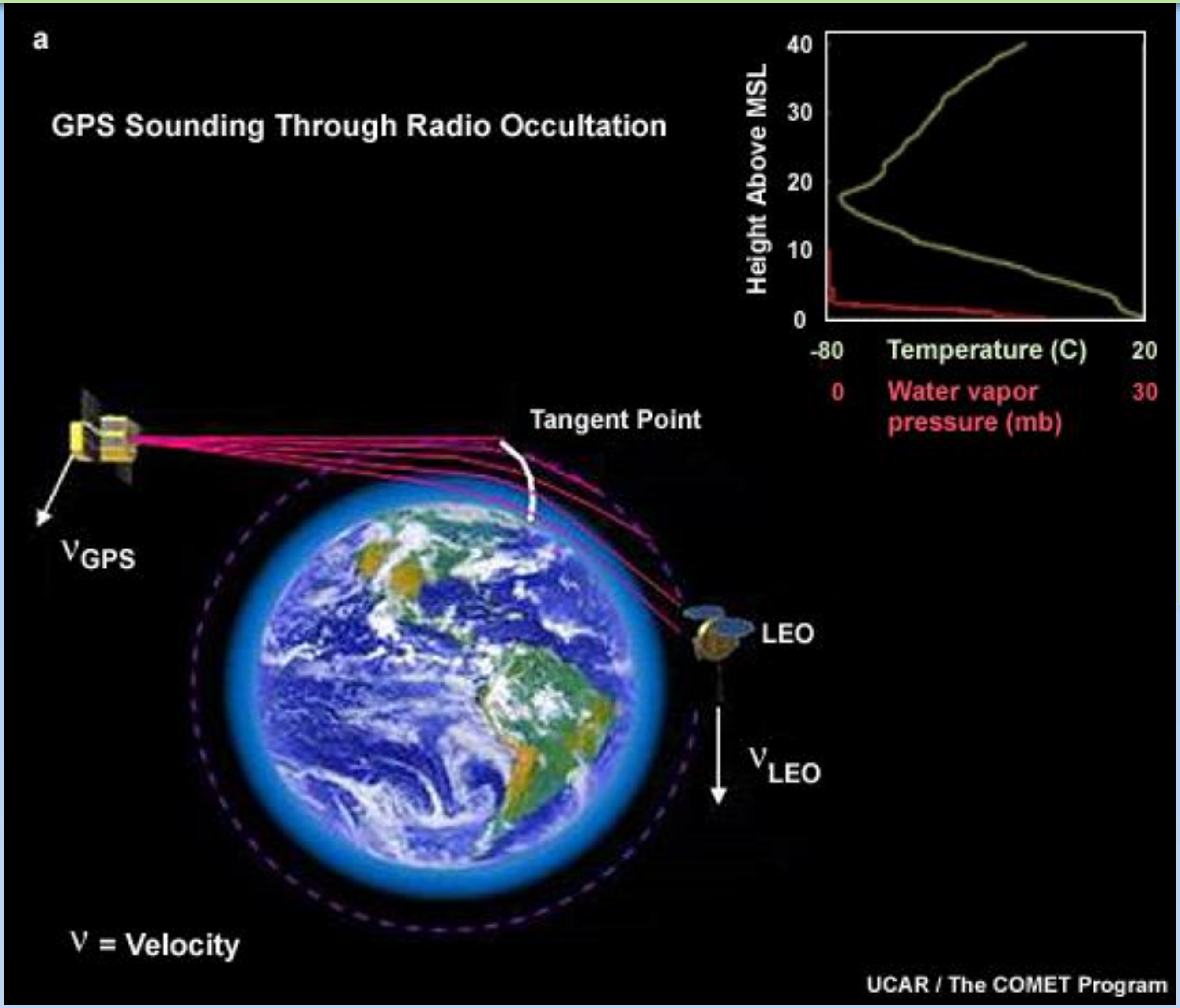

Figure 9.36(a) Schematic showing bending of GPS satellite signals due to variations in atmospheric density, a function of temperature and relative humidity and profiles of temperature .

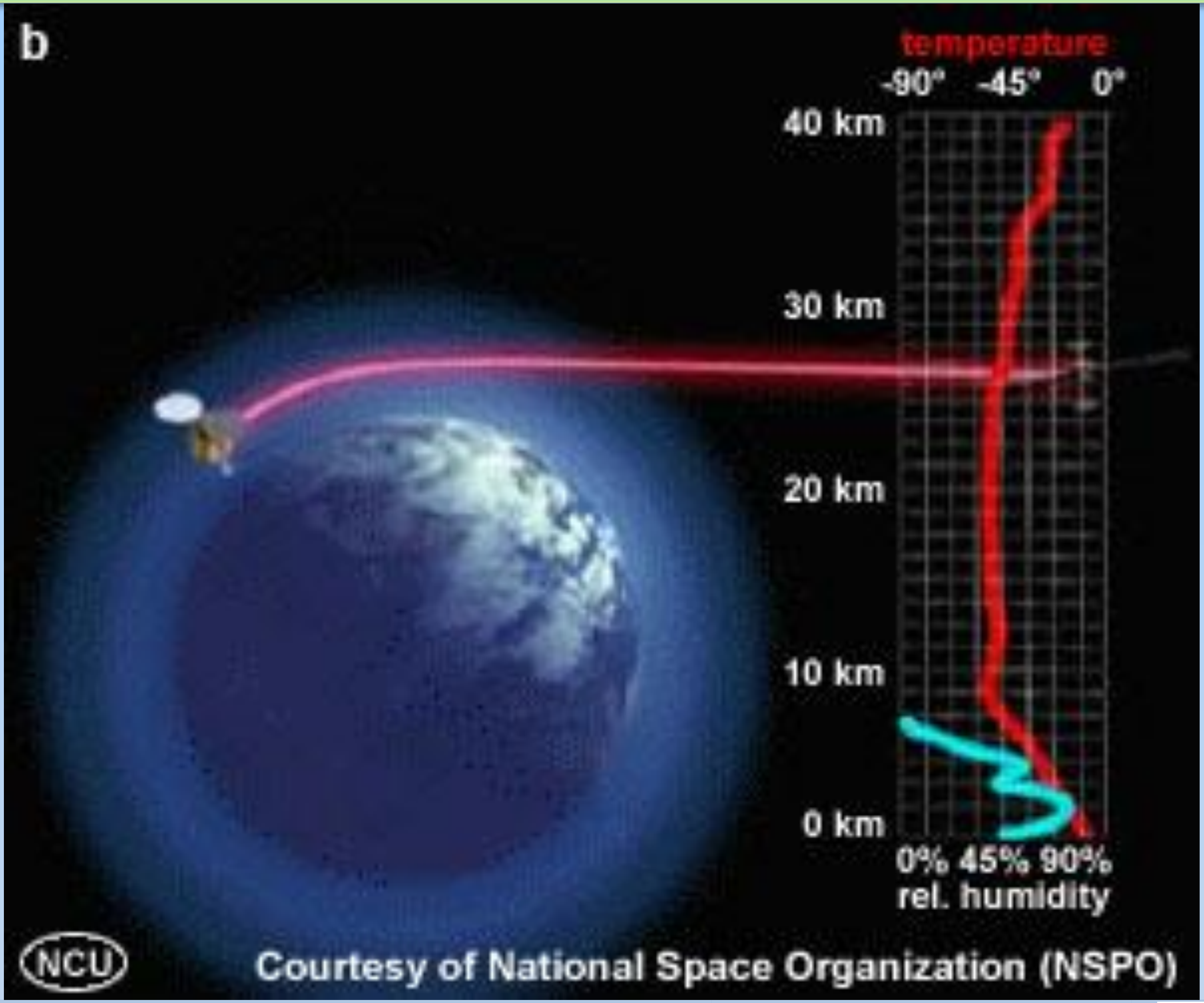

Figure 9.36(b) Schematic showing profiles of temperature and relative humidity derived from the retrieved refractions.

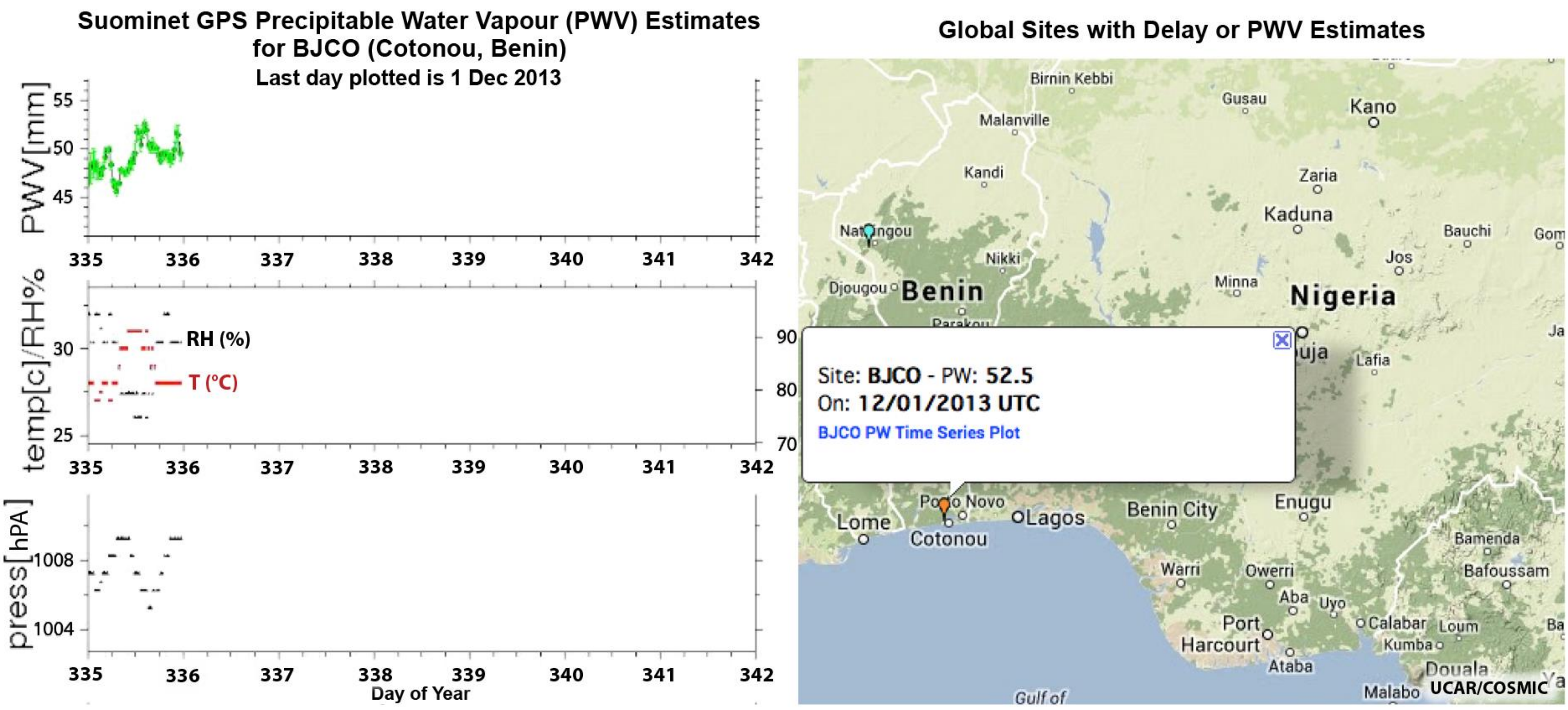

Figure 9.37. Real-time observations of precipitable water vapour, temperature, relative humidity, and pressure from surface GPS instruments at Cotonou, Benin.

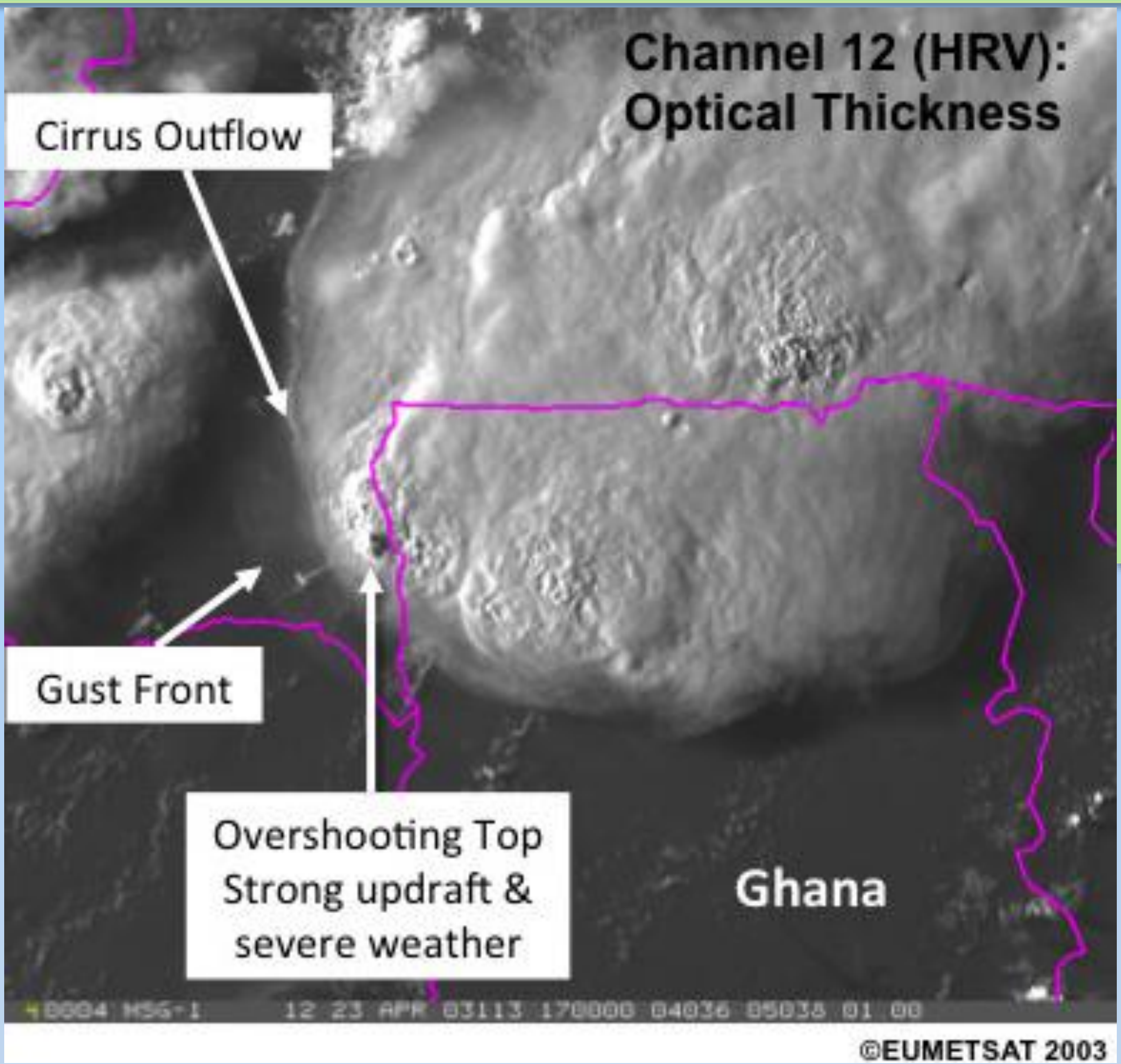

Figure 9.38. HRV image of convection over Ghana and Burkina Faso.

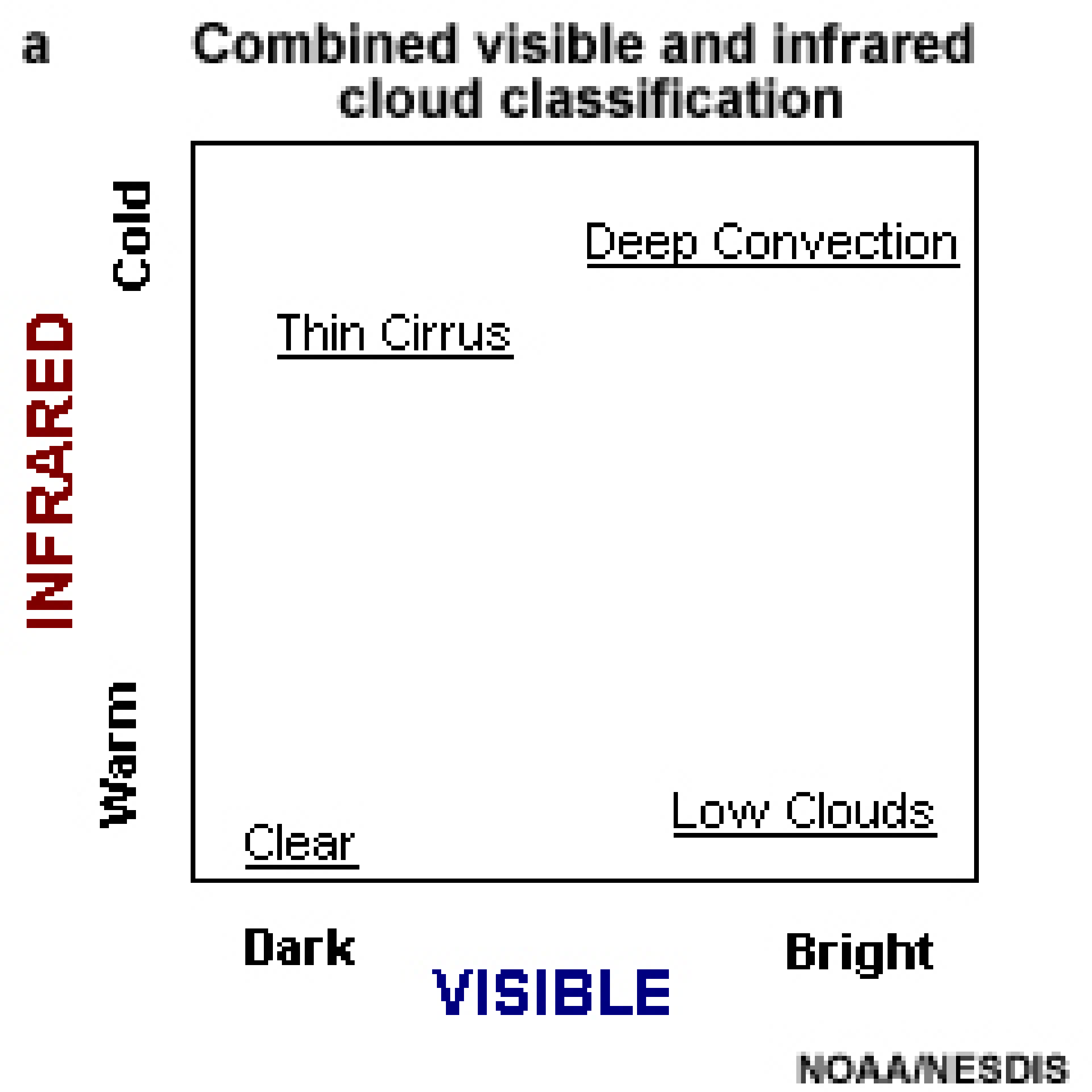

Figure 9.39 (a) Cloud type identification using a combination of visible and IR imagery. Main cloud classifications are low, medium, and high cumulus and semi-transparent cirrus ("sem." in the legend of 9.39b). Cirrus is also categorized as thin, medium, thick, or above other clouds. For example, "sem. thin" means semi-transparent thin cirrus.

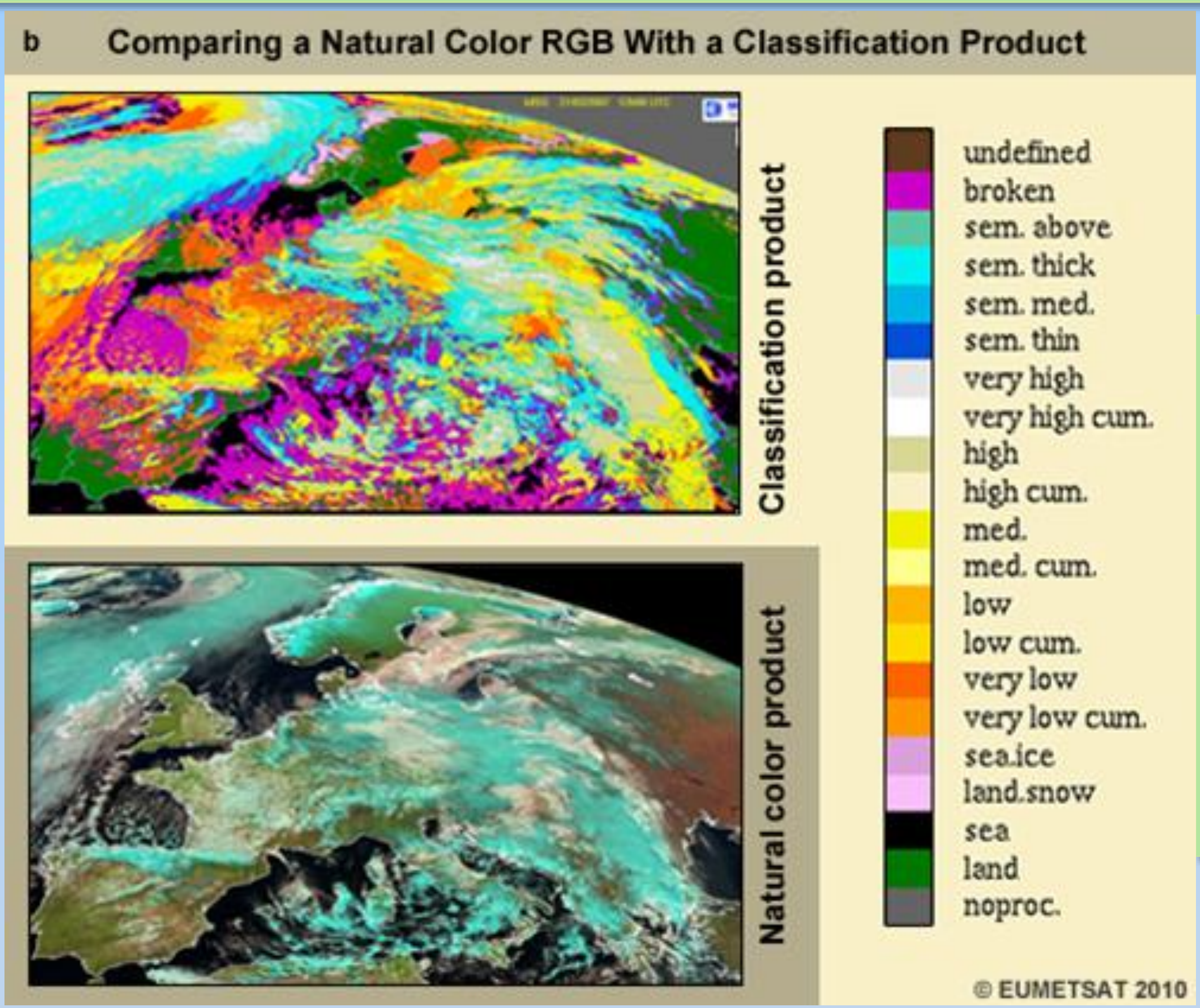

Figure 9.39(b) Clouds identified by cloud classification compared with natural colour RGB. Main cloud classifications are low, medium, and high cumulus and semi-transparent cirrus ("sem." in the legend). Cirrus is also categorized as thin, medium, thick, or above other clouds. For example, "sem. thin" means semi-transparent thin cirrus.

Chapter 9: *Remote Sensing* - Lead Author Arlene Laing, CIRA, Colorado State University

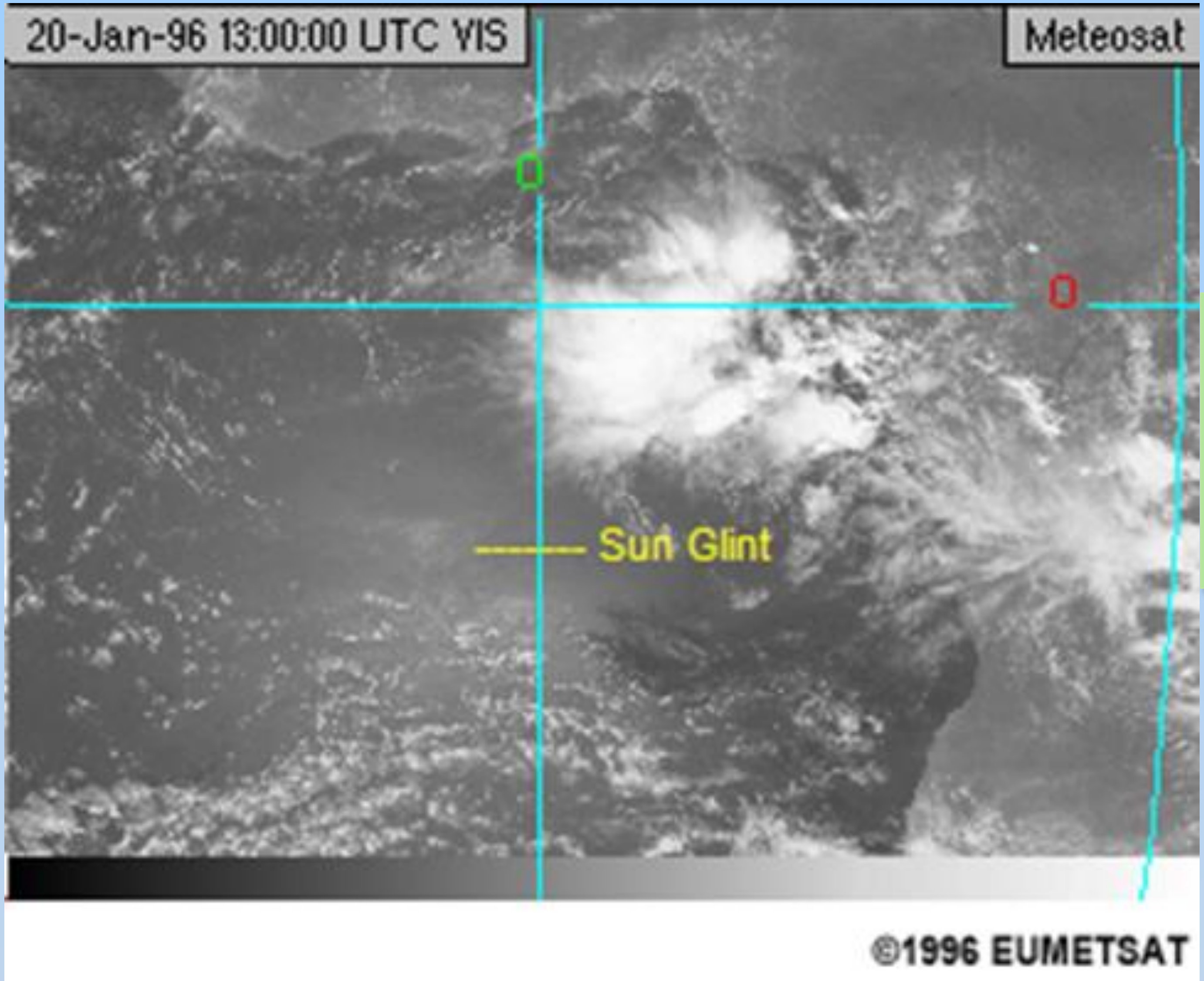

Figure 9.40 Sun glint over the Gulf of Guinea; note the brightness of the sun glint relative to the rest of the ocean surface.

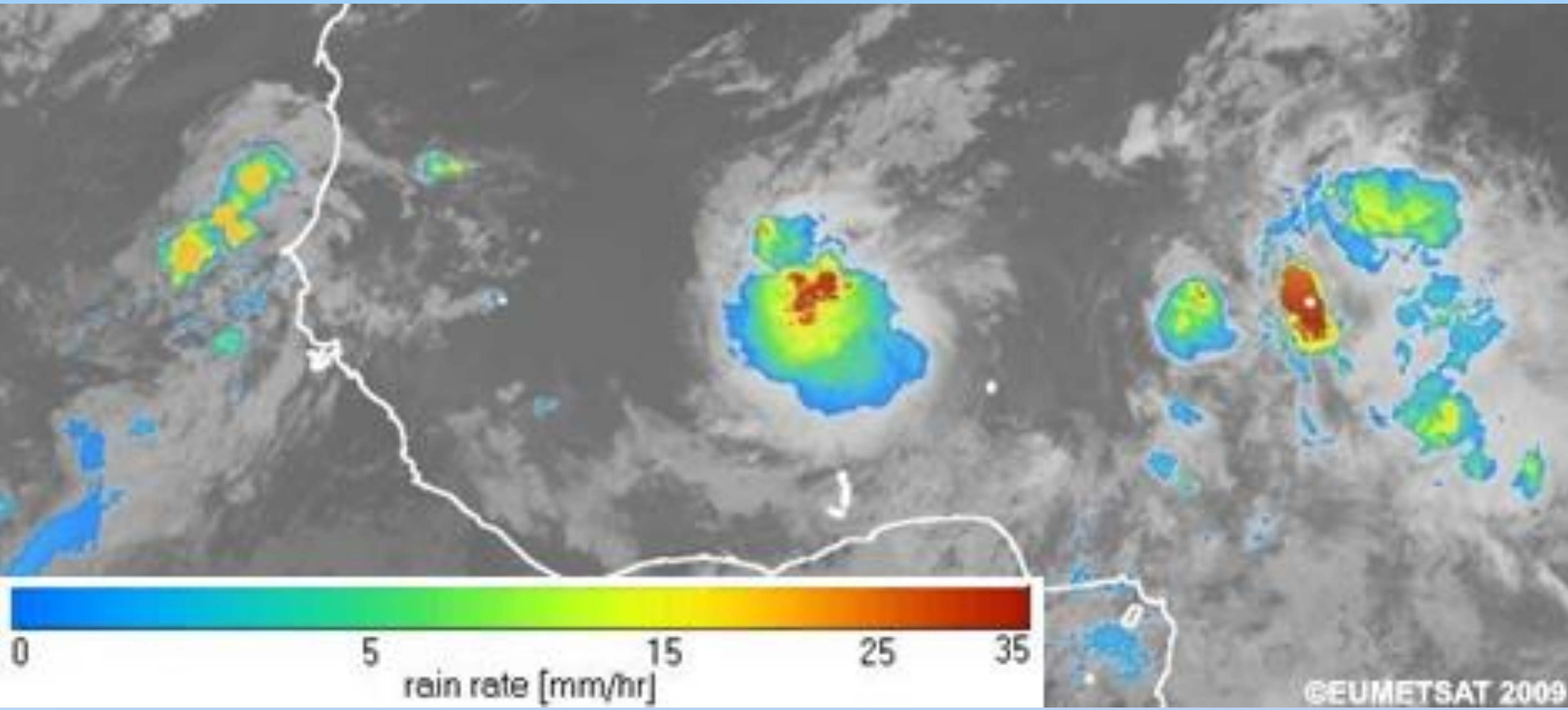

Figure 9.41. Meteosat Multisensor Precipitation Estimate (MPE) image showing high rain rates produced by an intensive mesoscale convective system (MCS) that caused record flooding in Ouagadougou on 1 Sept 2009

Chapter 9: *Remote Sensing* - Lead Author Arlene Laing, CIRA, Colorado State University

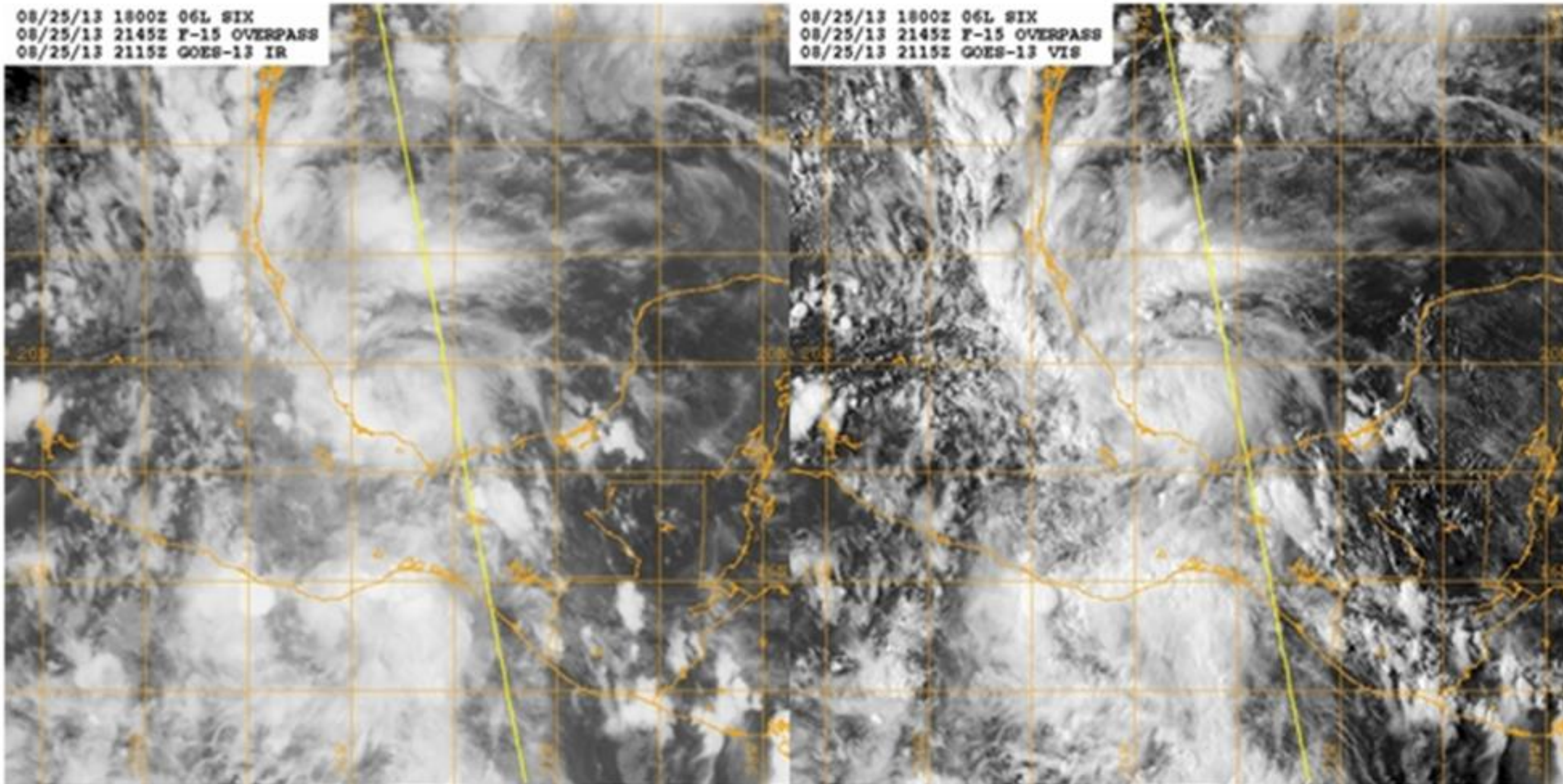

Figure 9.42. Tropical storm over the Gulf of Mexico observed by (a) geostationary IR and (b) geostationary visible sensors. The RGB shows deep convection, low-level water vapour, and precipitation. PCT < 255K almost always indicates precipitation. The eye and eyewall are apparent in the centre of the image in the microwave, but obscured in the IR and visible.

Chapter 9: *Remote Sensing* - Lead Author Arlene Laing, CIRA, Colorado State University

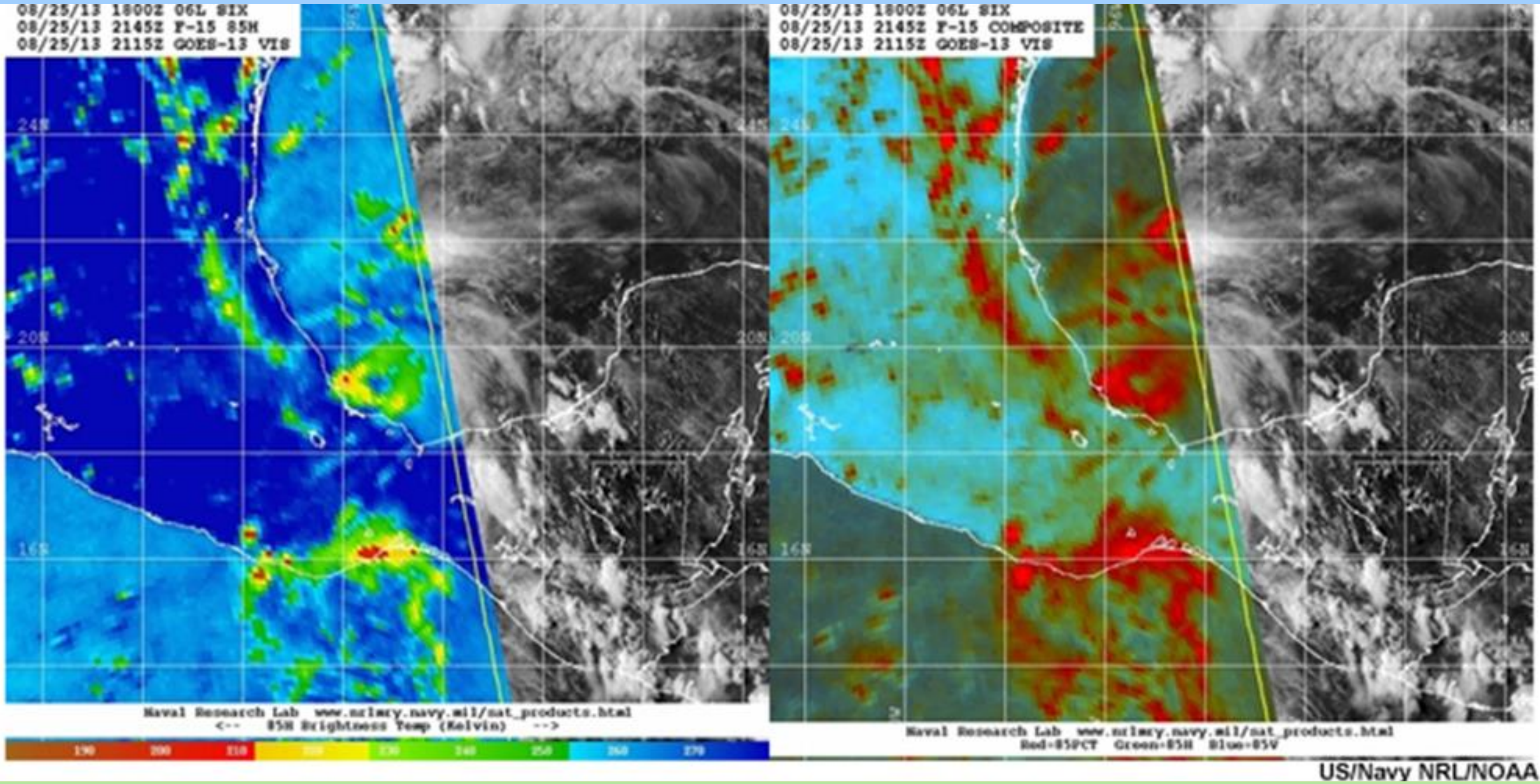

Figure 9.42. Tropical storm over the Gulf of Mexico observed by (c) polar-orbiting microwave 85 GHz polarization corrected temperature (PCT) and, (d) RGB composite of the 85 GHz PCT and 85 GHz horizontal and vertical polarization. The RGB shows deep convection, low-level water vapour, and precipitation. PCT < 255K almost always indicates precipitation. The eye and eyewall are apparent in the centre of the image in the microwave, but obscured in the IR and visible.

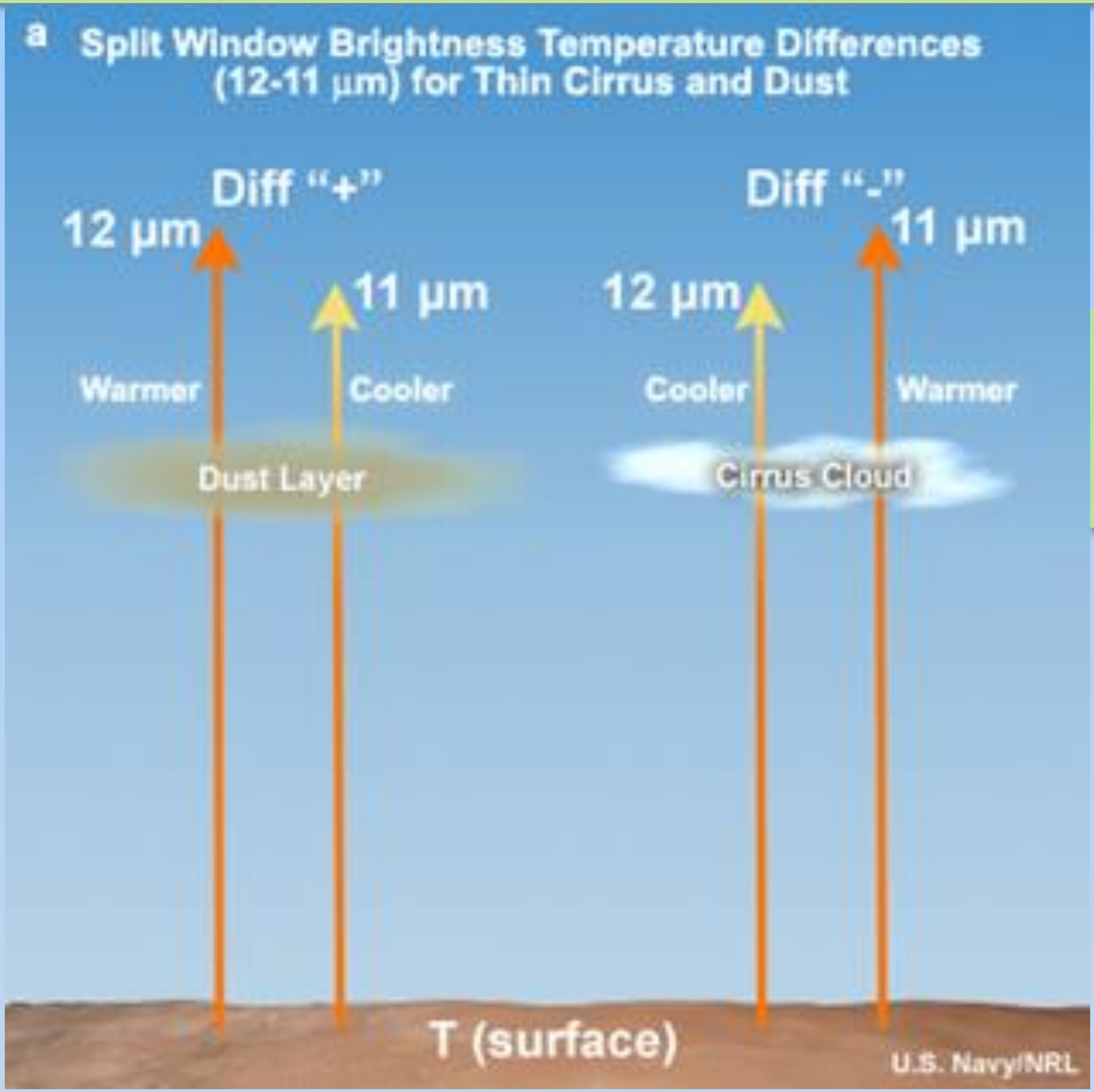

Figure 9.43 (a) Conceptual model of the split window used to differentiate between dust and cirrus.

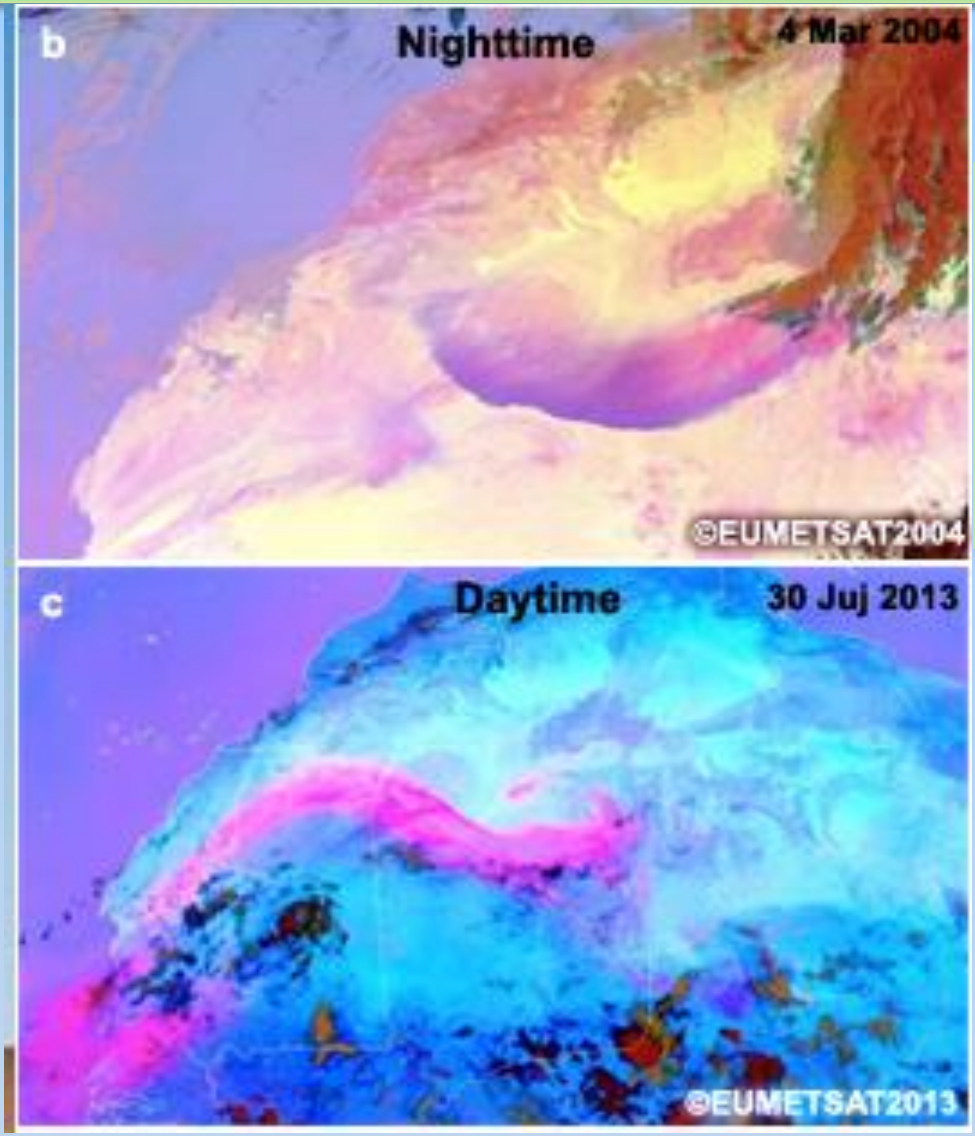

Figure 9.43 (b) Conceptual model of the split window used to differentiate between dust and cirrus. Dust RGB during nighttime, 4 Mar 2004 (upper), and (lower) daytime, 30 Jul 2013 (same as right hand panel of Figure 9.22).

Chapter 9: *Remote Sensing* - Lead Author Arlene Laing, CIRA, Colorado State University

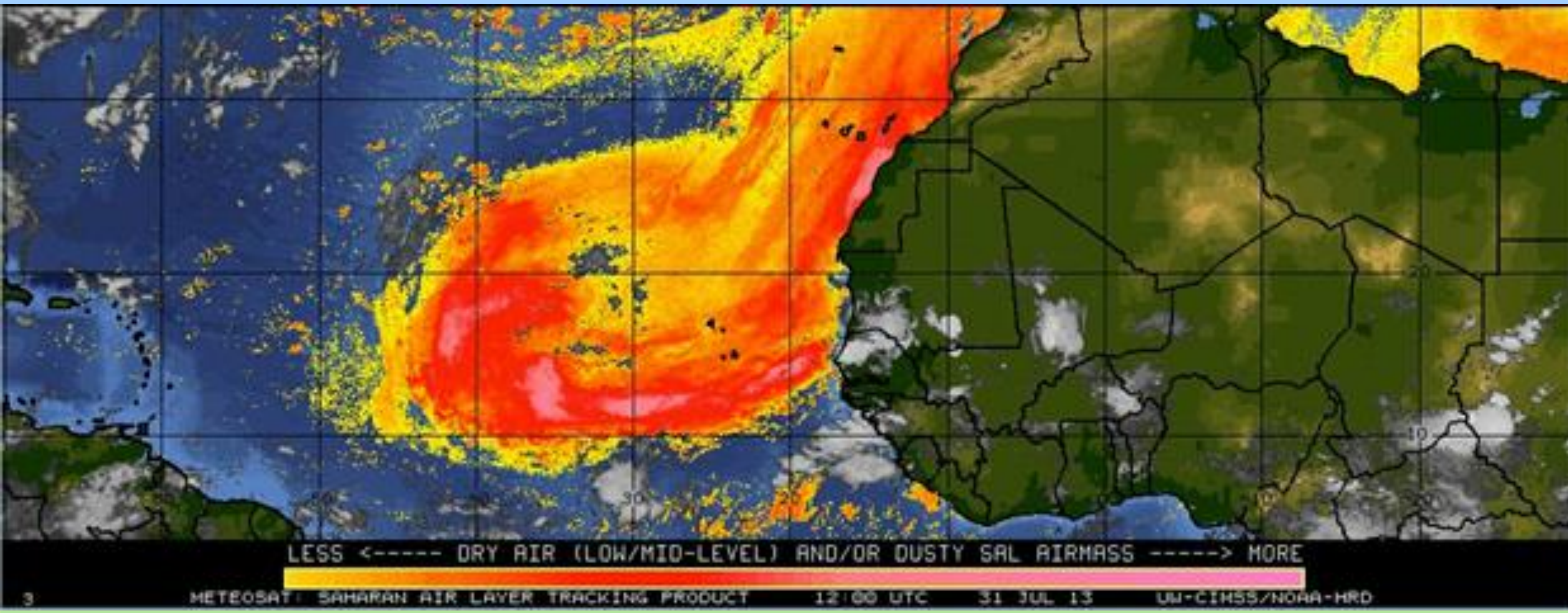

Figure 9.44. A major dust storm, 31 Jul 2013, is monitored using the Sahara Air Layer tracking product derived from Meteosat channels. (Courtesy of University of Wisconsin-CIMSS and NOAA Hurricane Research Division)

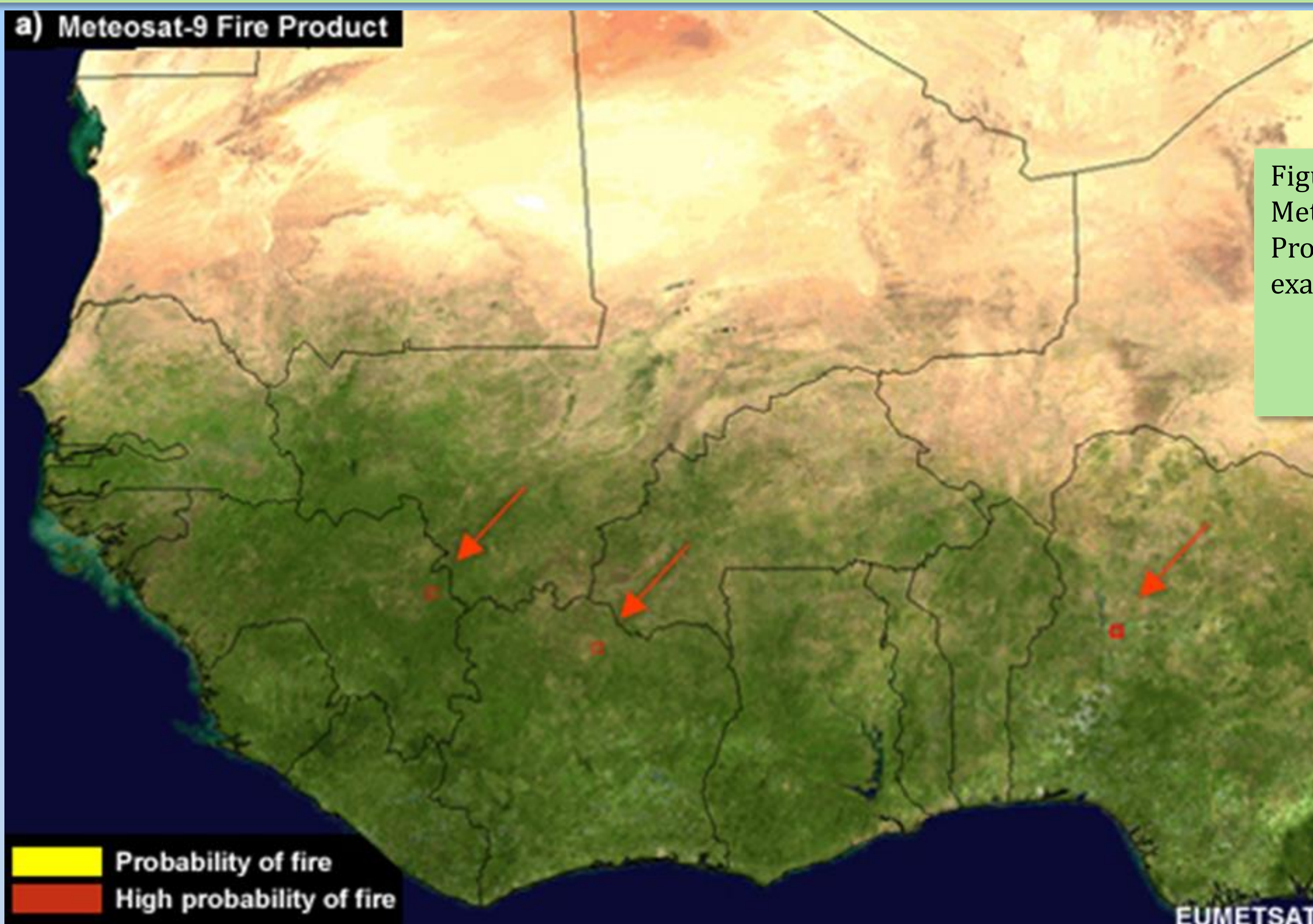

Figure 9.45 (a) Meteosat-9 Fire Product example.

Chapter 9: *Remote Sensing* - Lead Author Arlene Laing, CIRA, Colorado State University

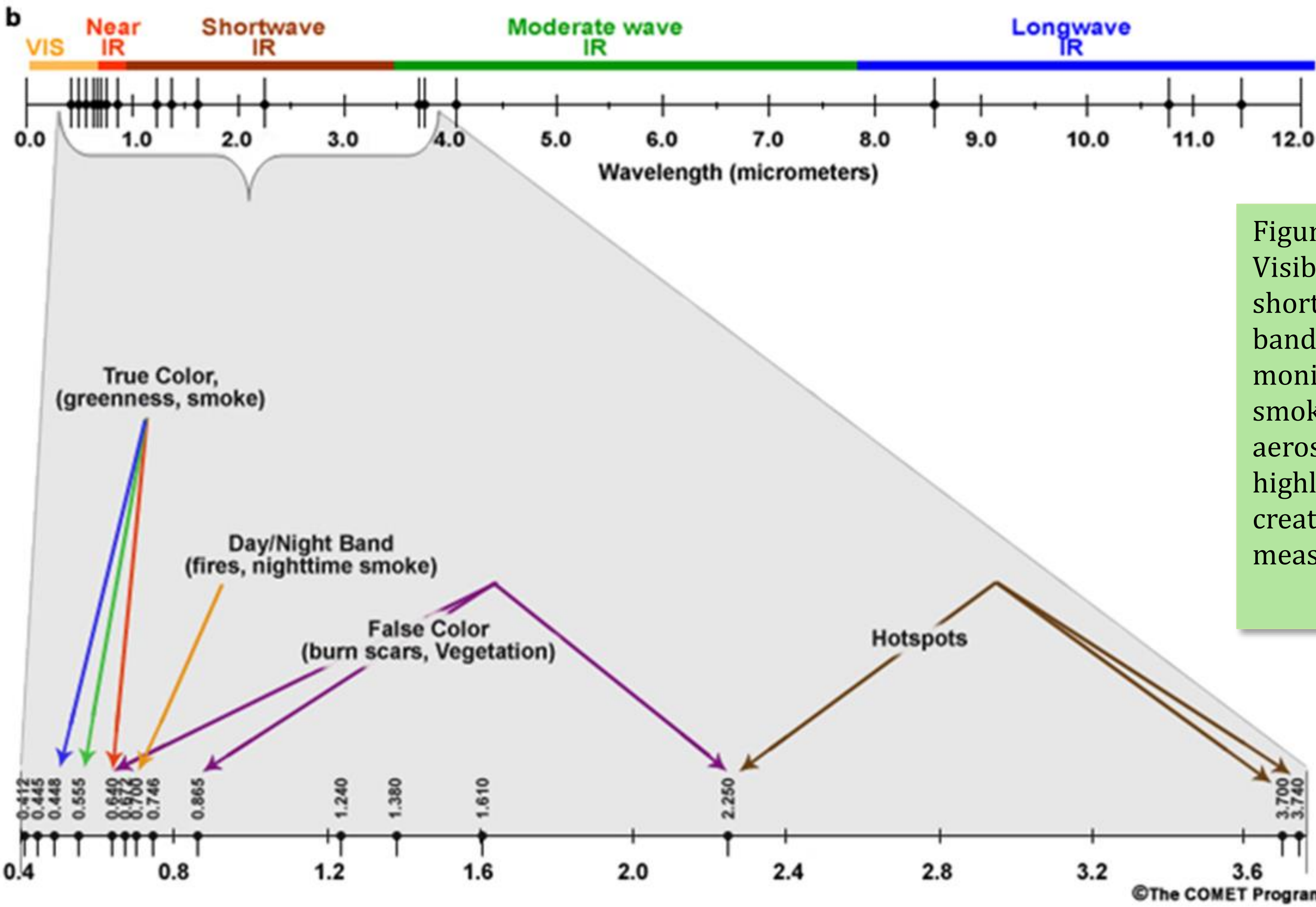

Figure 9.45 (b) Visible and shortwave IR bands used to monitor fires, smoke, and other aerosols. Labels highlight RGBs created from VIIRS measurements.

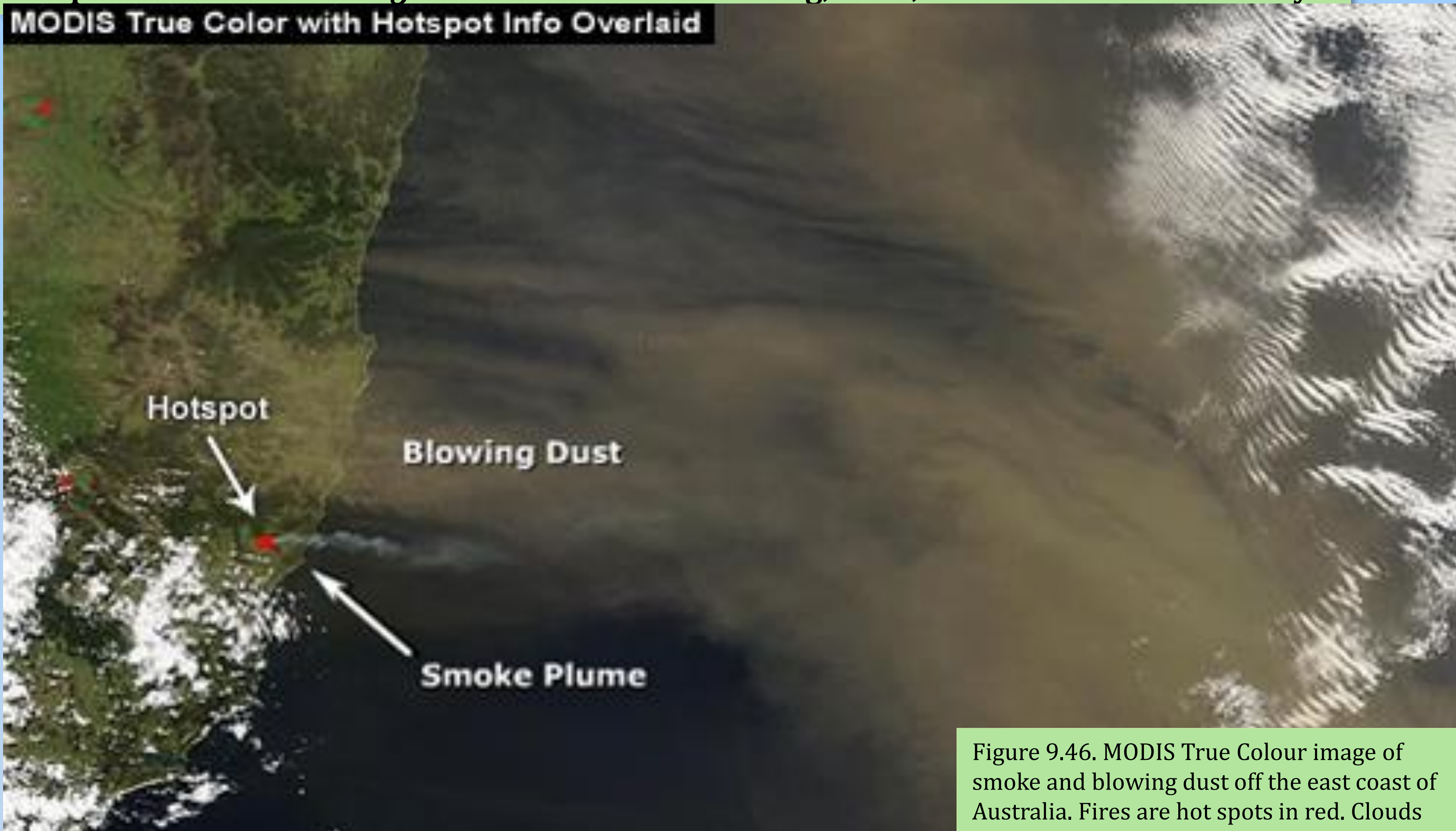

Figure 9.46. MODIS True Colour image of smoke and blowing dust off the east coast of Australia. Fires are hot spots in red. Clouds are bright white. Smoke is the grey line extending from a fire spot.

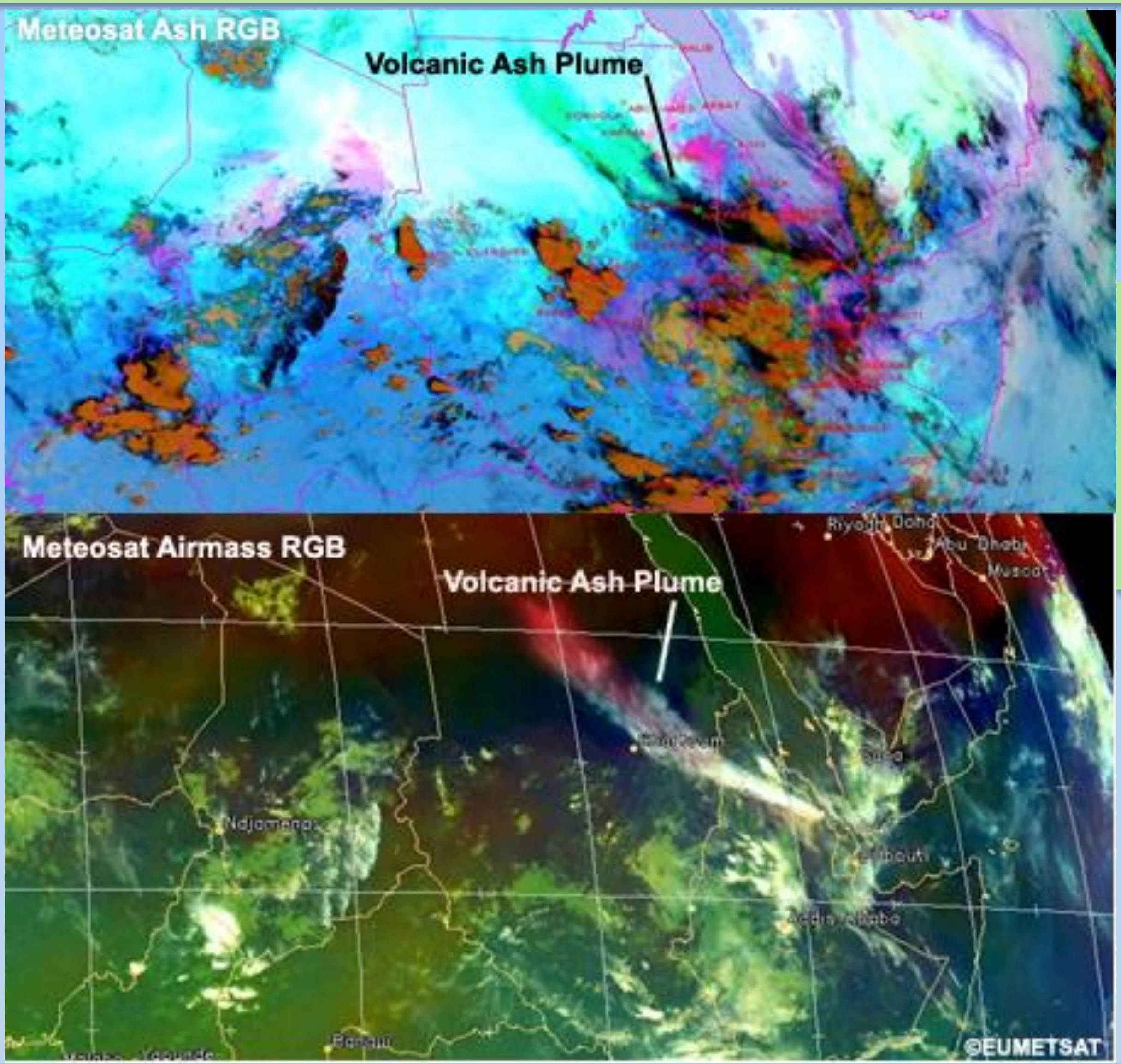

Figure 9.47 Volcanic ash and gases emanating northwestward from Ethiopia are observed using Meteosat Ash RGB (upper) and the Air Mass RGB (lower).

Chapter 9: *Remote Sensing* - Lead Author Arlene Laing, CIRA, Colorado State University

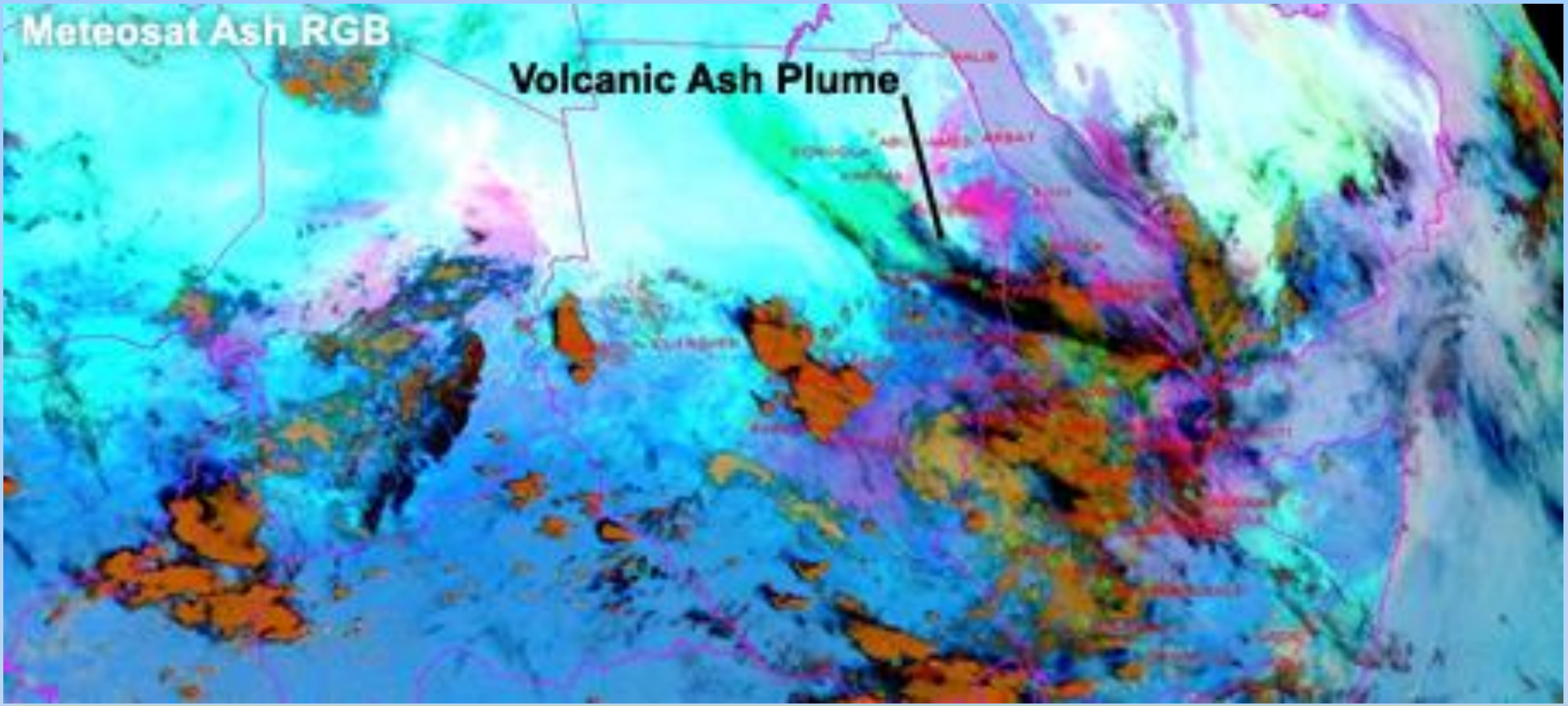

Figure 9.47 Volcanic ash and gases emanating northwestward from Ethiopia are observed using Meteosat Ash RGB.

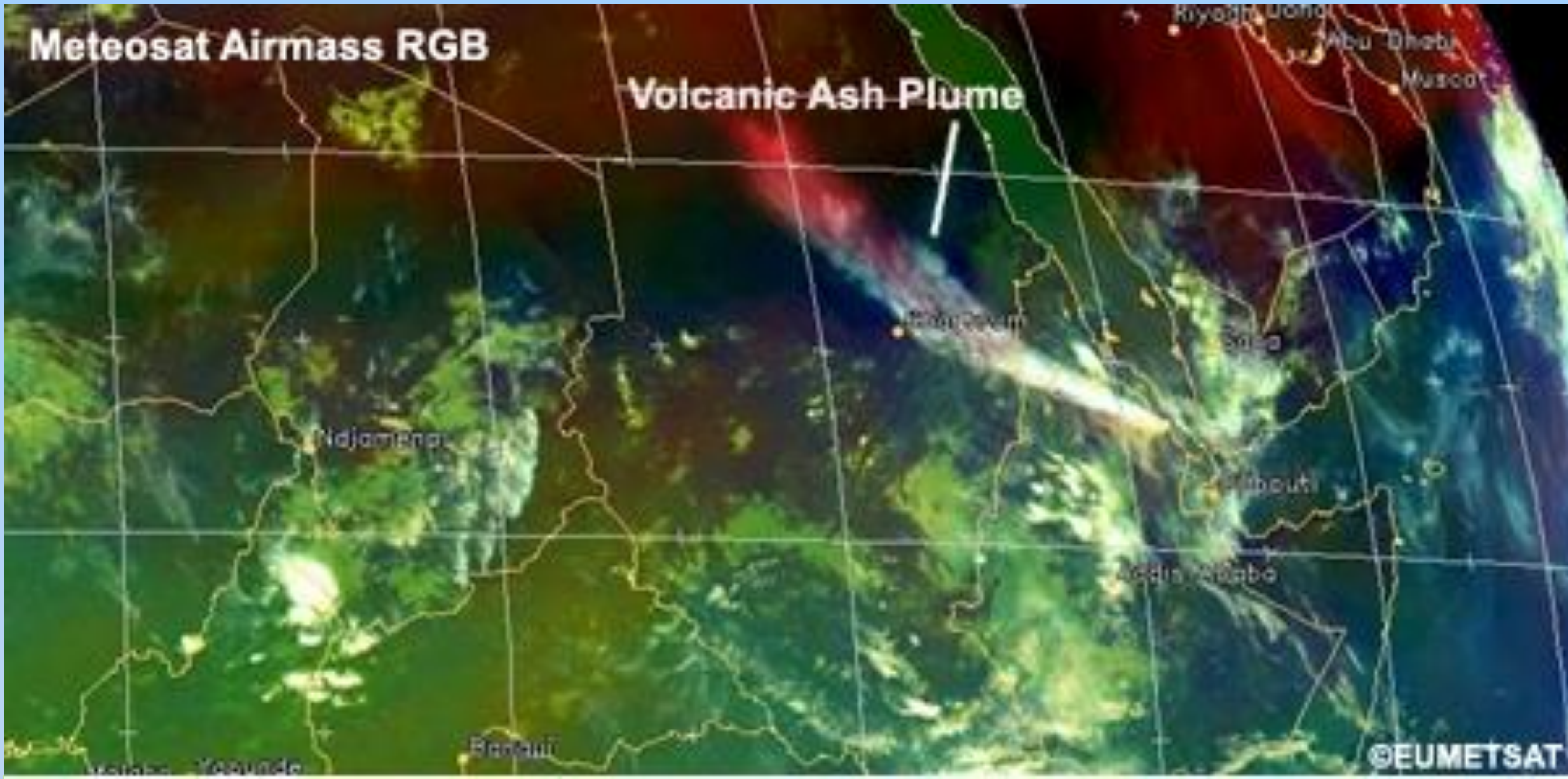

Figure 9.47 Volcanic ash and gases emanating northwestward from Ethiopia are observed using the Air Mass RGB.

Chapter 9: *Remote Sensing* - Lead Author Arlene Laing, CIRA, Colorado State University

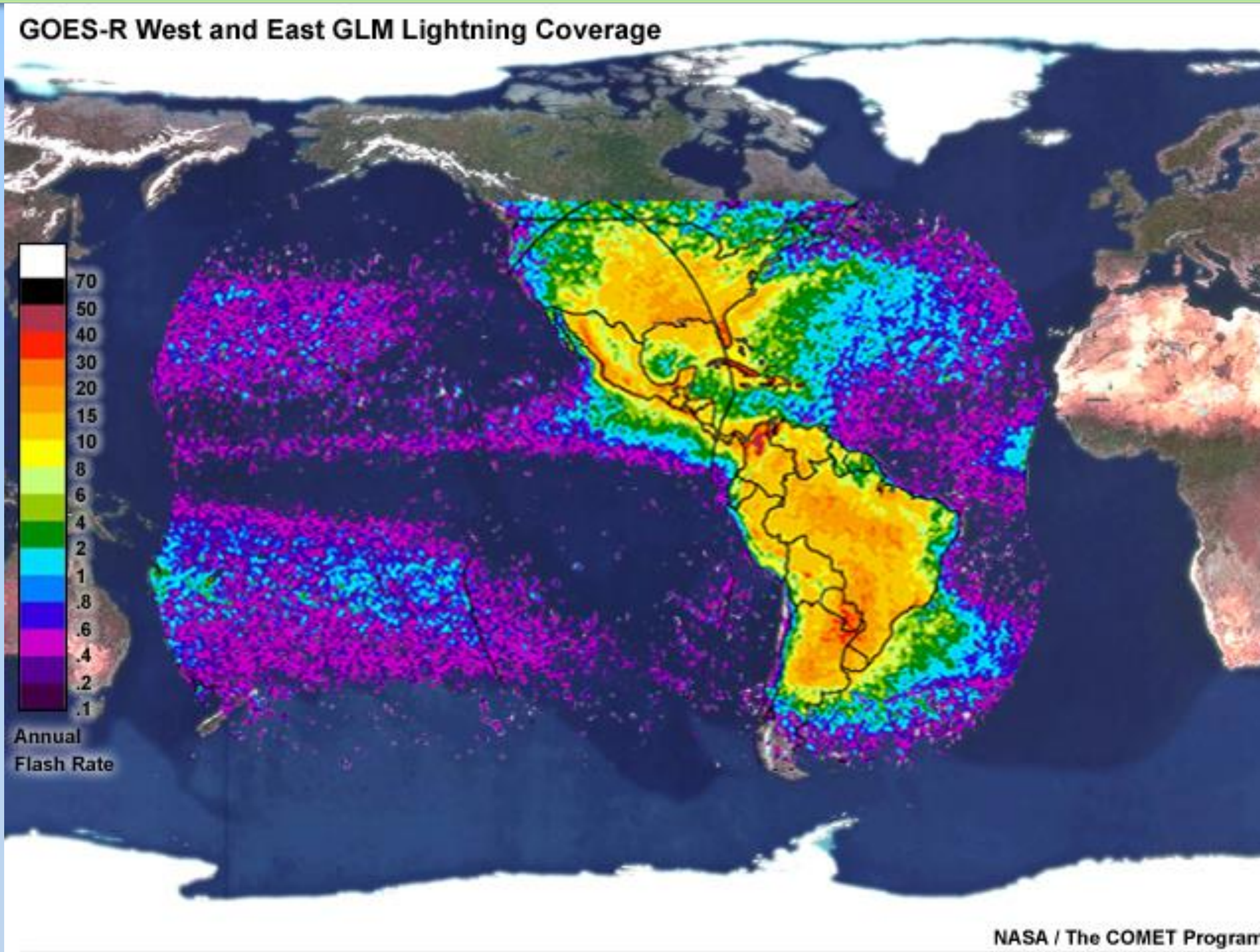

Figure 9.48 Simulation of lightning flash density coverage for the planned geostationary lightning mapper on GOES

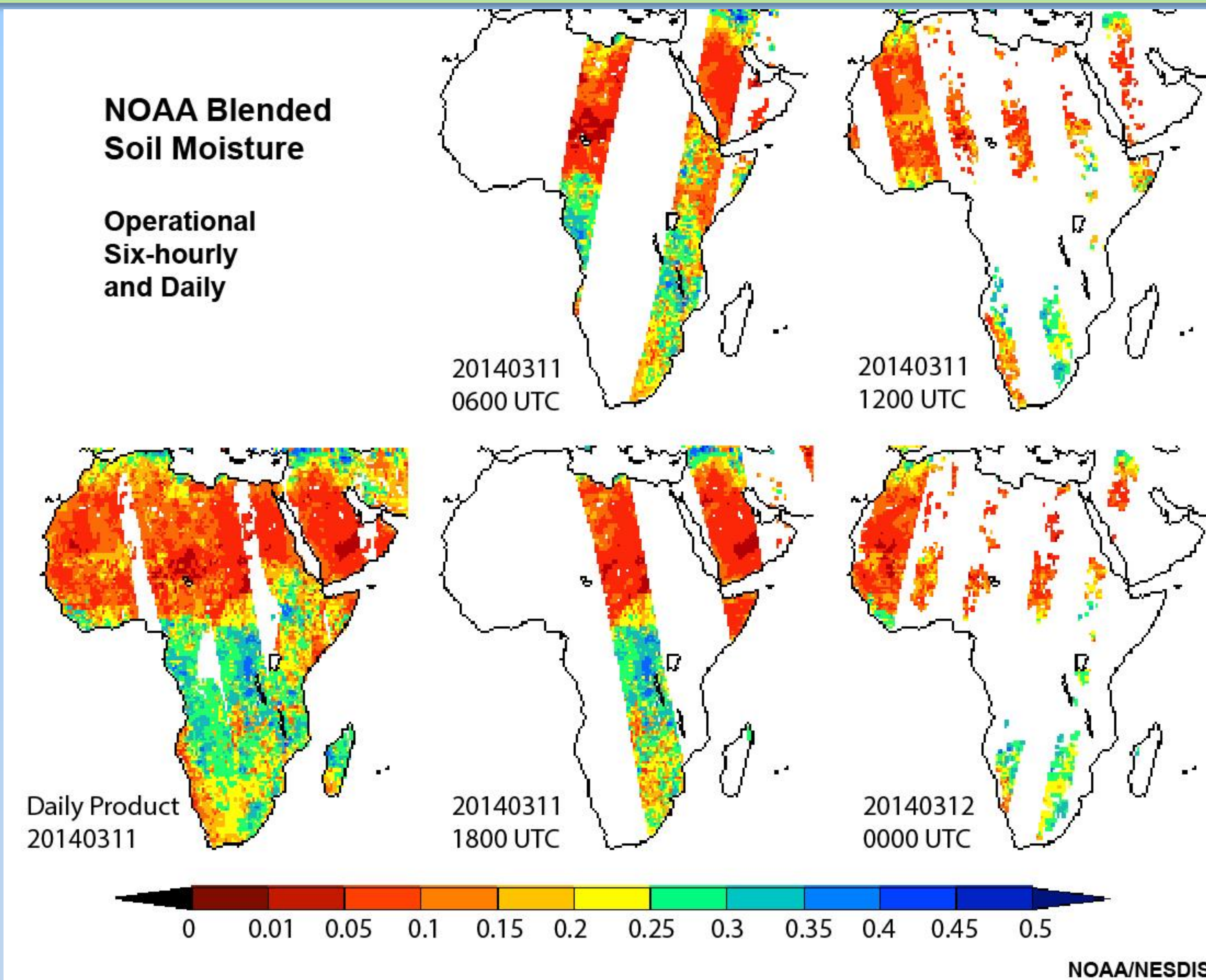

Figure 9.49. Example of blended soil moisture (% of water by volume of soil) from satellite microwave sensors available operationally, on a 0.25° x 0.25° grid, at six-hourly and daily intervals.

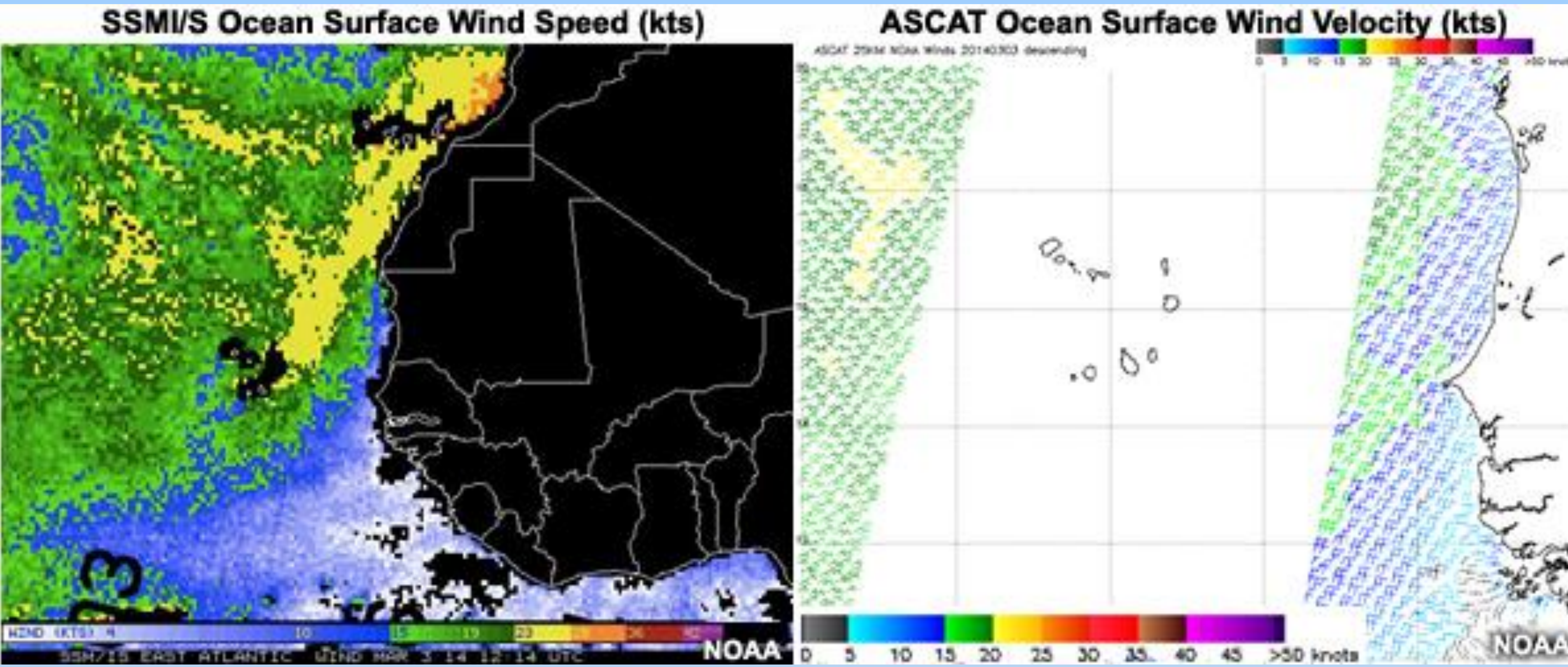

Figure 9.50 (left) Special Sensor Microwave Imager/Sounder (SSMIS) wind speed and (right) Advanced Scatterometer (ASCAT) wind speed and direction on 3 March 2014.

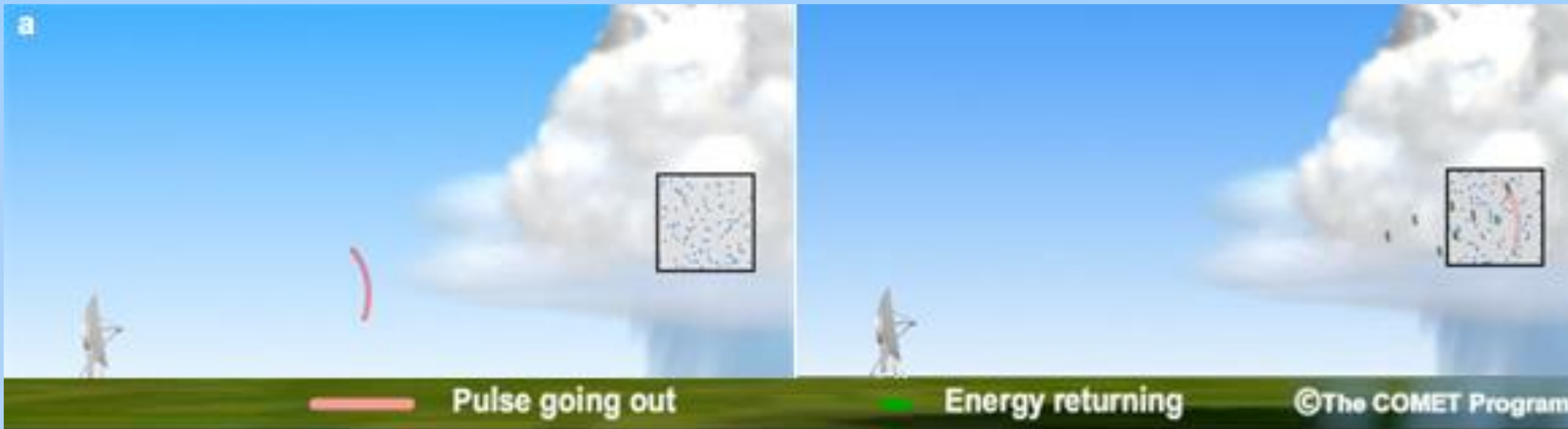

Figure 9.51(a) Schematics showing how radar operates to detect hydrometeors in a cloud.

Chapter 9: *Remote Sensing* - Lead Author Arlene Laing, CIRA, Colorado State University

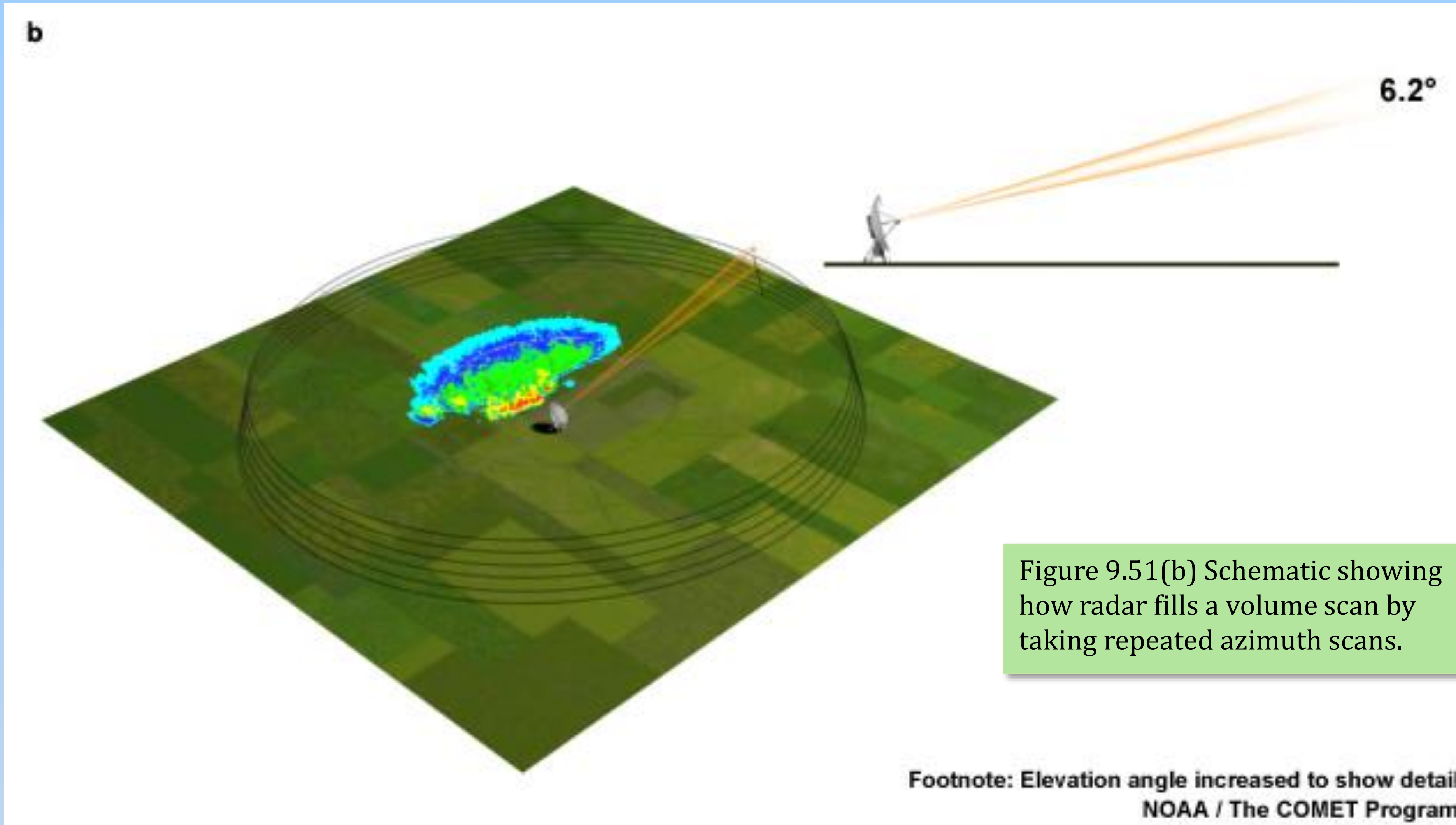

Figure 9.51(b) Schematic showing how radar fills a volume scan by taking repeated azimuth scans.

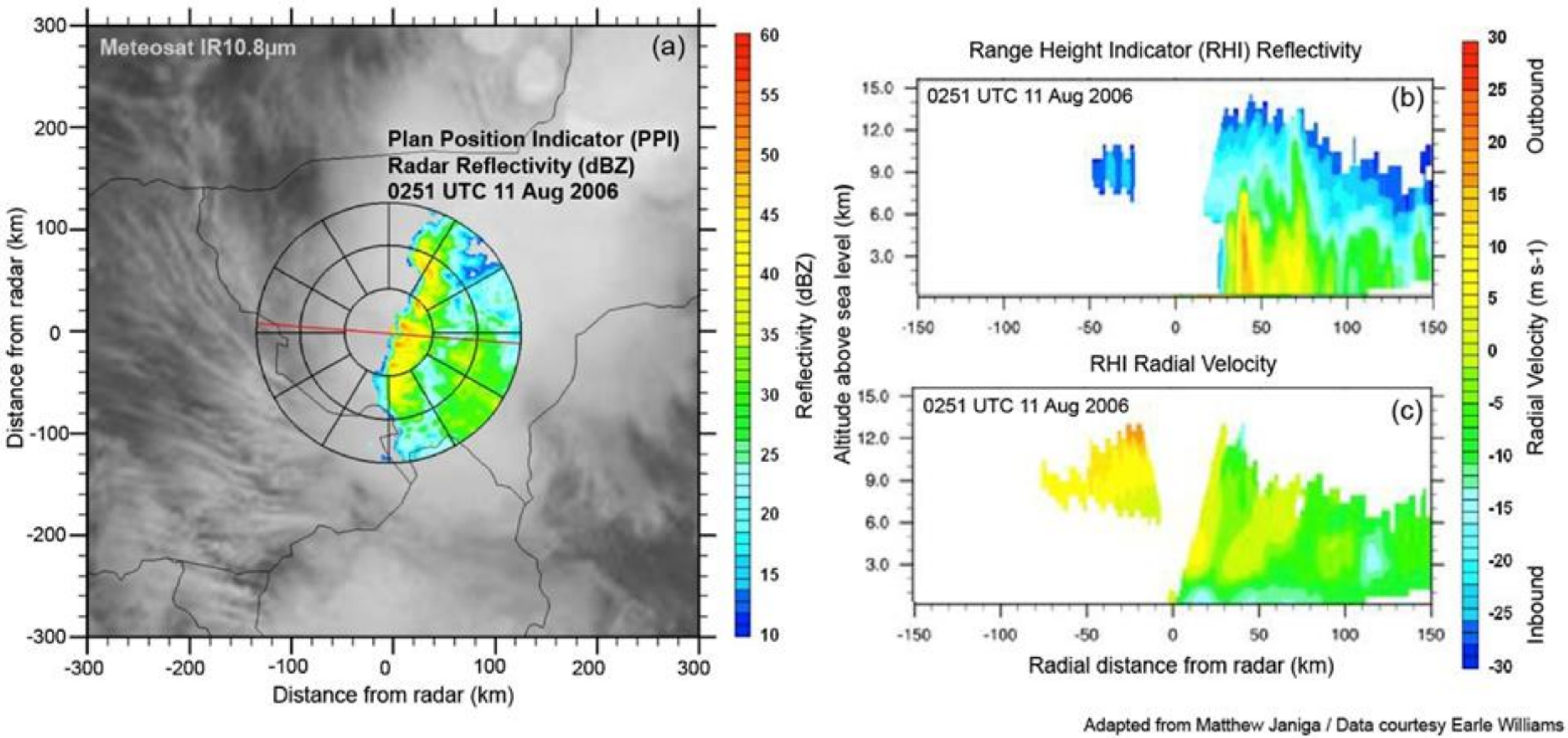

Figure 9.52. (a) Plan Position Indicator (PPI) base reflectivity produced by an MCS over Niamey, Niger at 0251 UTC on 11 August 2006 overlaid on Meteosat IR 10.8μm. Images in (b) and (c) are the corresponding Range Height Indicator (RHI) reflectivity and radial velocity, respectively, taken along the red line in (a). Notice in (b) and (c) the cone-shaped clear area directly above the radar; an area that is not scanned, and so termed “the cone of silence”.

Chapter 9: *Remote Sensing* - Lead Author Arlene Laing, CIRA, Colorado State University

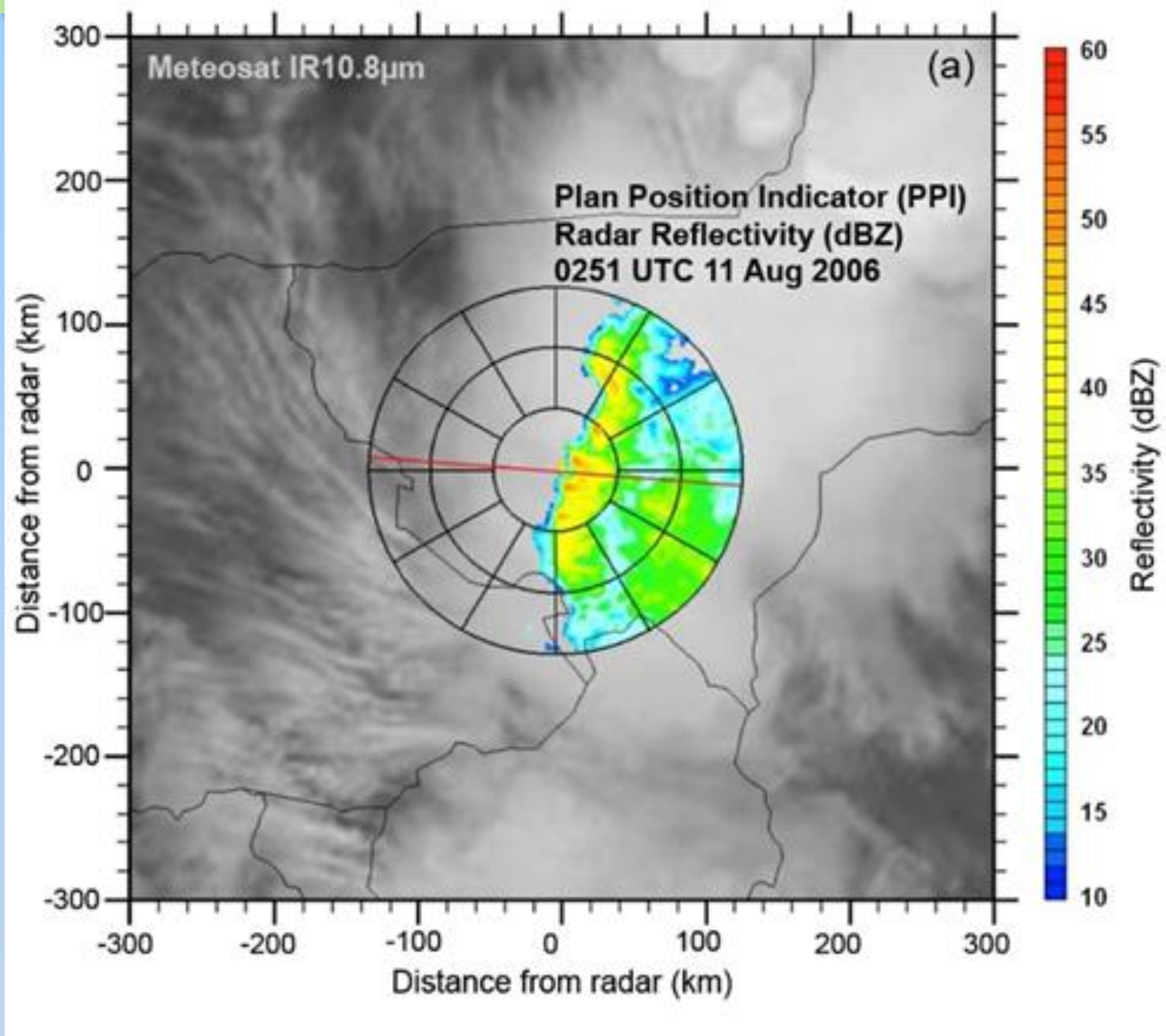

Figure 9.52. (a) Plan Position Indicator (PPI) base reflectivity produced by an MCS over Niamey, Niger at 0251 UTC on 11 August 2006 overlaid on Meteosat IR 10.8µm.

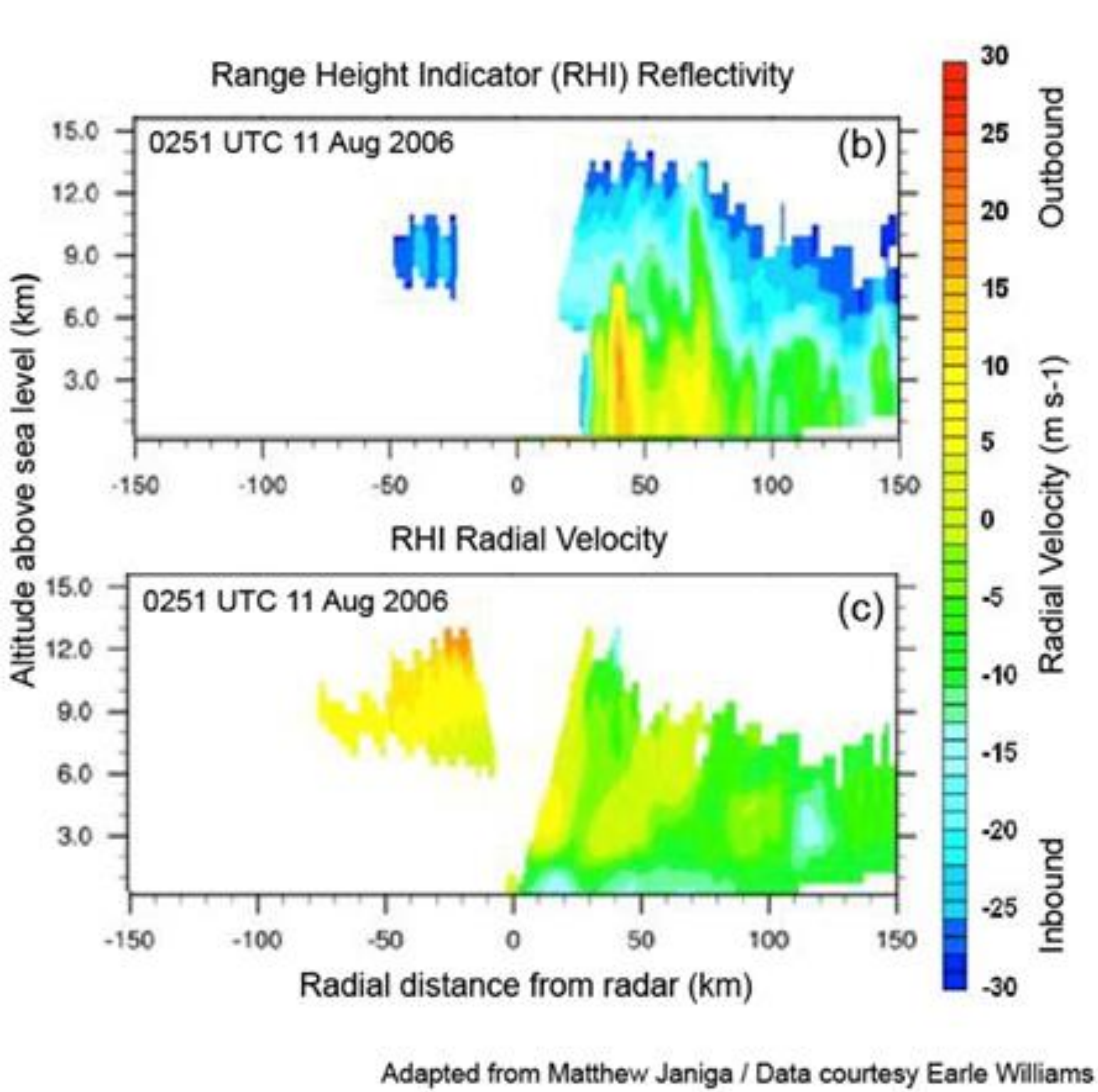

Figure 9.52 (b) and (c) show the corresponding Range Height Indicator (RHI) reflectivity and radial velocity, respectively, taken along the red line in 9.52(a). Notice in (b) and (c) the cone-shaped clear area directly above the radar; an area that is not scanned, and so termed "the cone of silence".

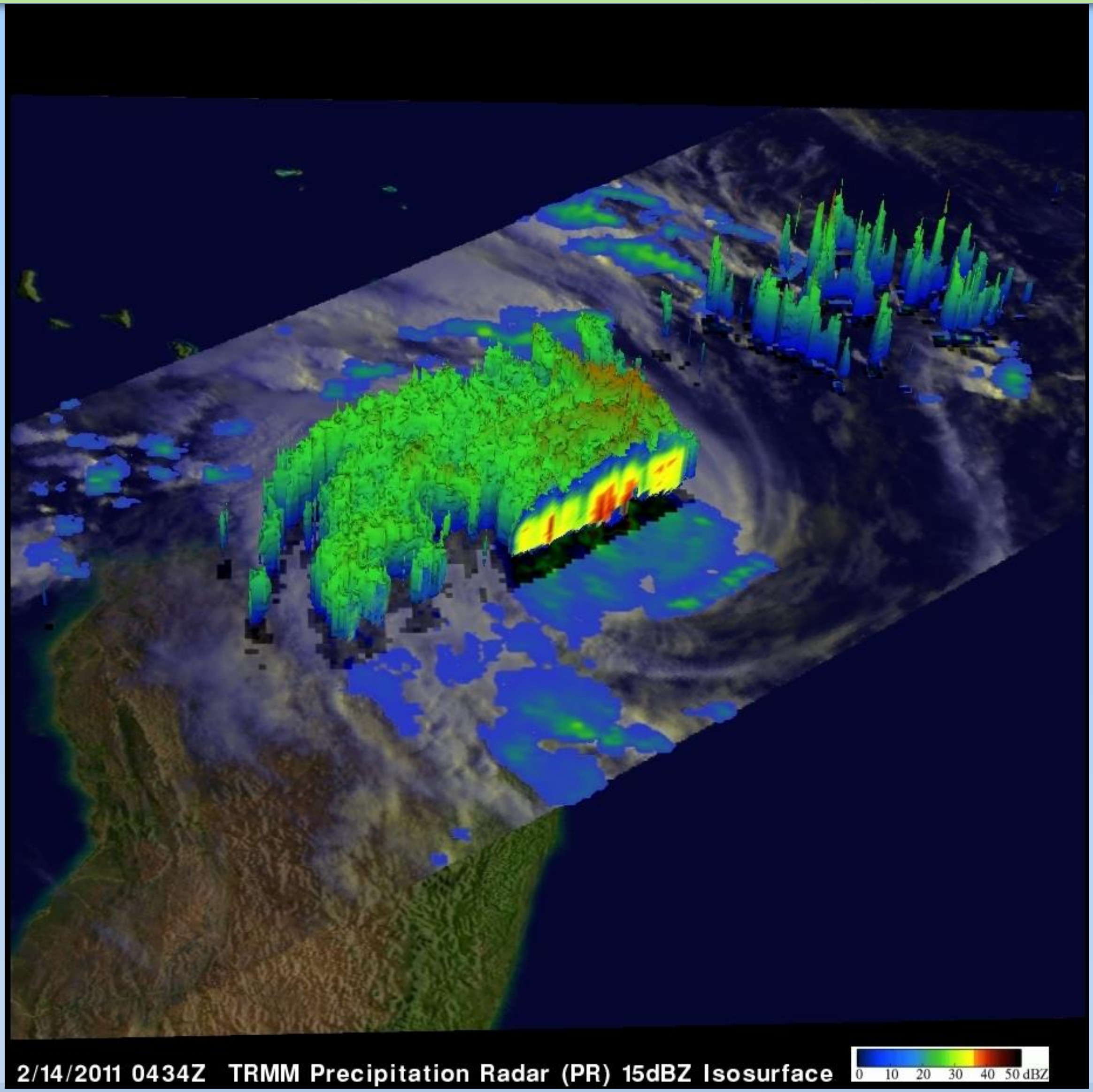

Figure 9.53
3-D image of radar reflectivity from TRMM Precipitation Radar showing a tropical cyclone making landfall in Madagascar.

Chapter 9: *Remote Sensing* - Lead Author Arlene Laing, CIRA, Colorado State University

Figure 9.54. Cumulonimbus clouds over Nigeria as seen by (a) Channel 1 VIS and (b) Channel 12 HRV at 0800 UTC 24 April 2003. (c) Coverage of the HRV from 0000-1400 UTC.(© EUMETSAT 2003)

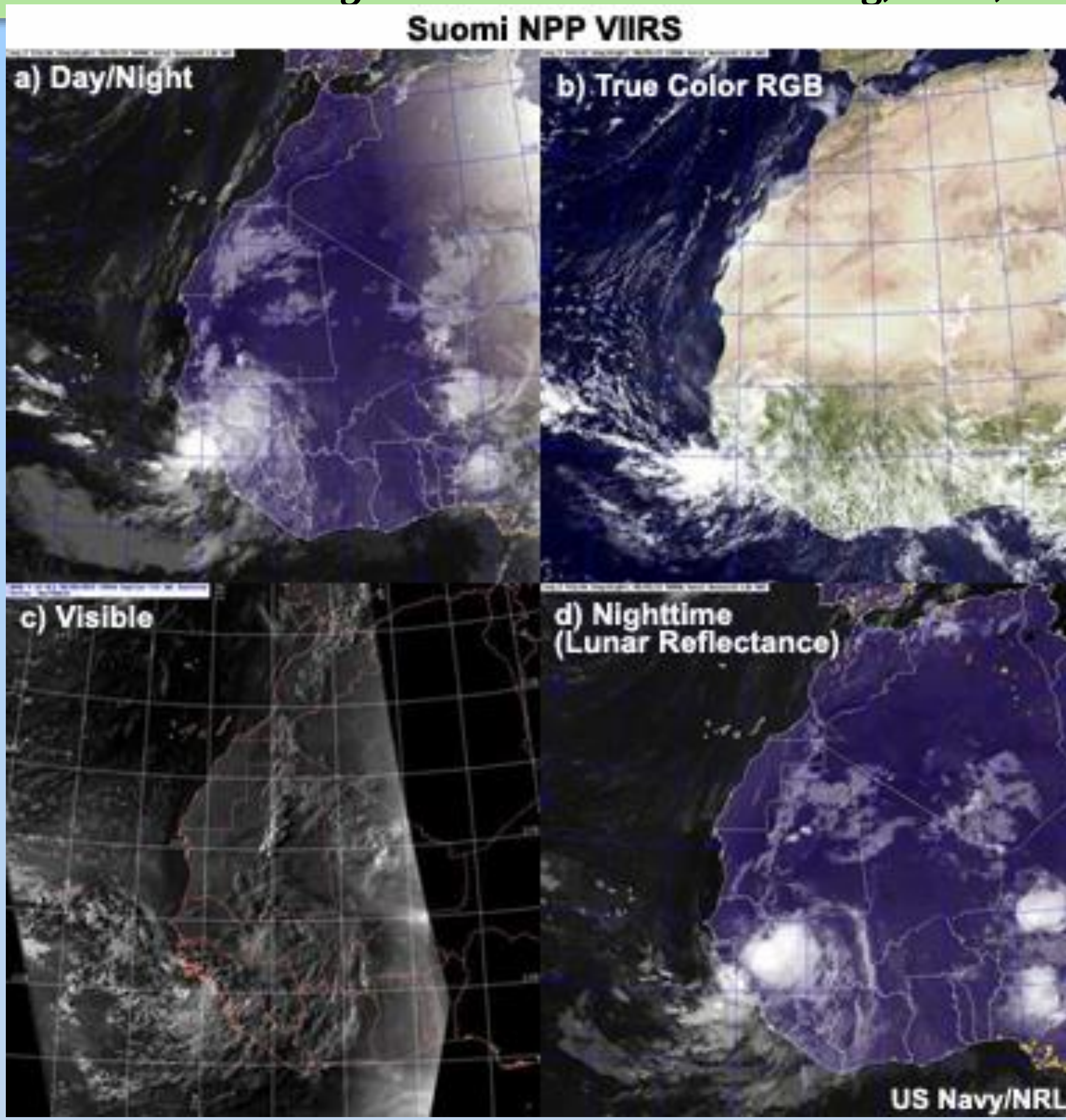

igure 9.55. xamples of VIIRS clockwise from pper left) ay/night, True olour RGB, isible, Night-time unar reflectance) roducts

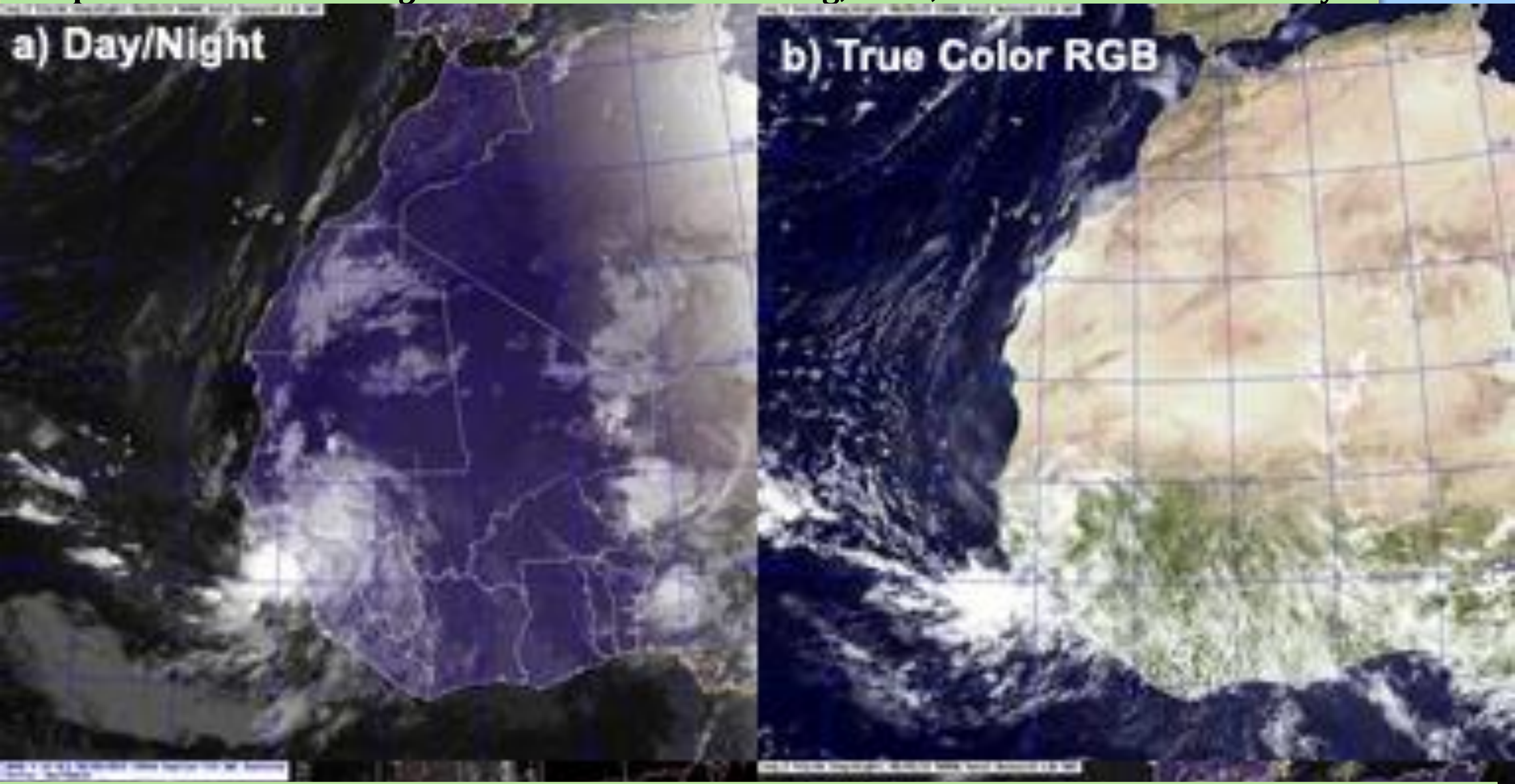

Figure 9.55. Examples of VIIRS (clockwise from upper left) Day/night, True Colour RGB, Visible, Night-time (lunar reflectance) products

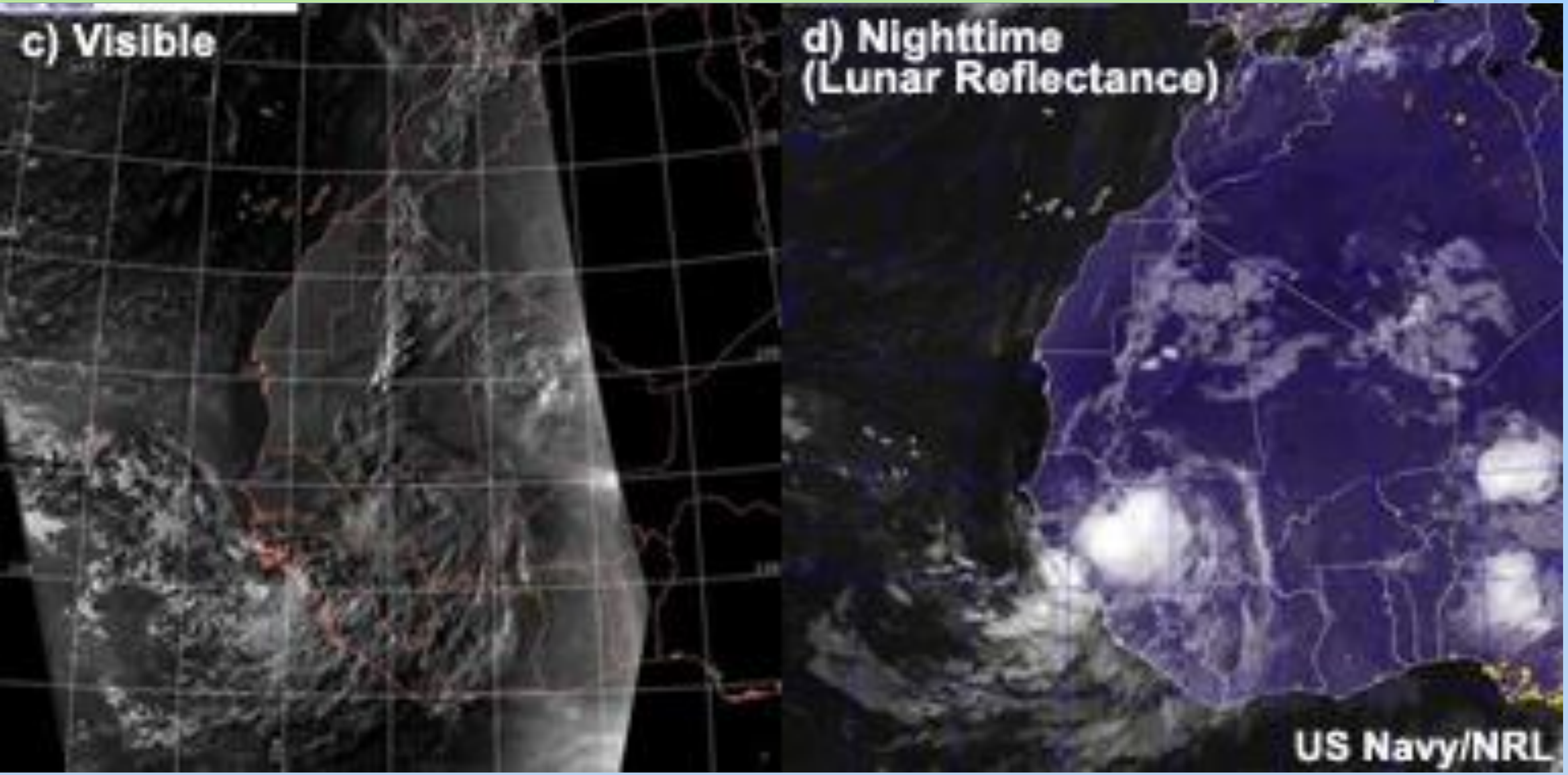

Figure 9.55. Examples of VIIRS (clockwise from upper left) Day/night, True Colour RGB, Visible, Night-time (lunar reflectance) products

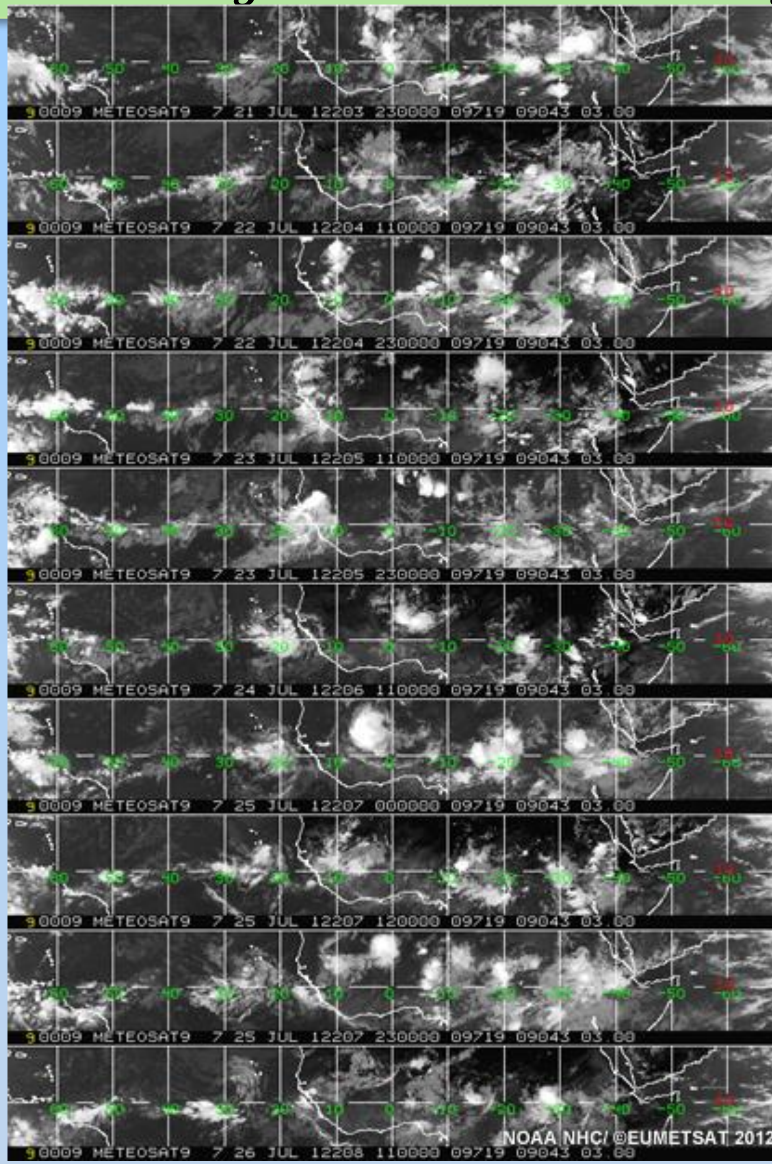

Figure 9.56. Hovmoller diagram of IR10.8 µm satellite images used to track the movement of synoptic weather systems over Africa and the tropical Atlantic over five days. Courtesy of NOAA National Hurricane Centre and ©EUMETSAT 2012

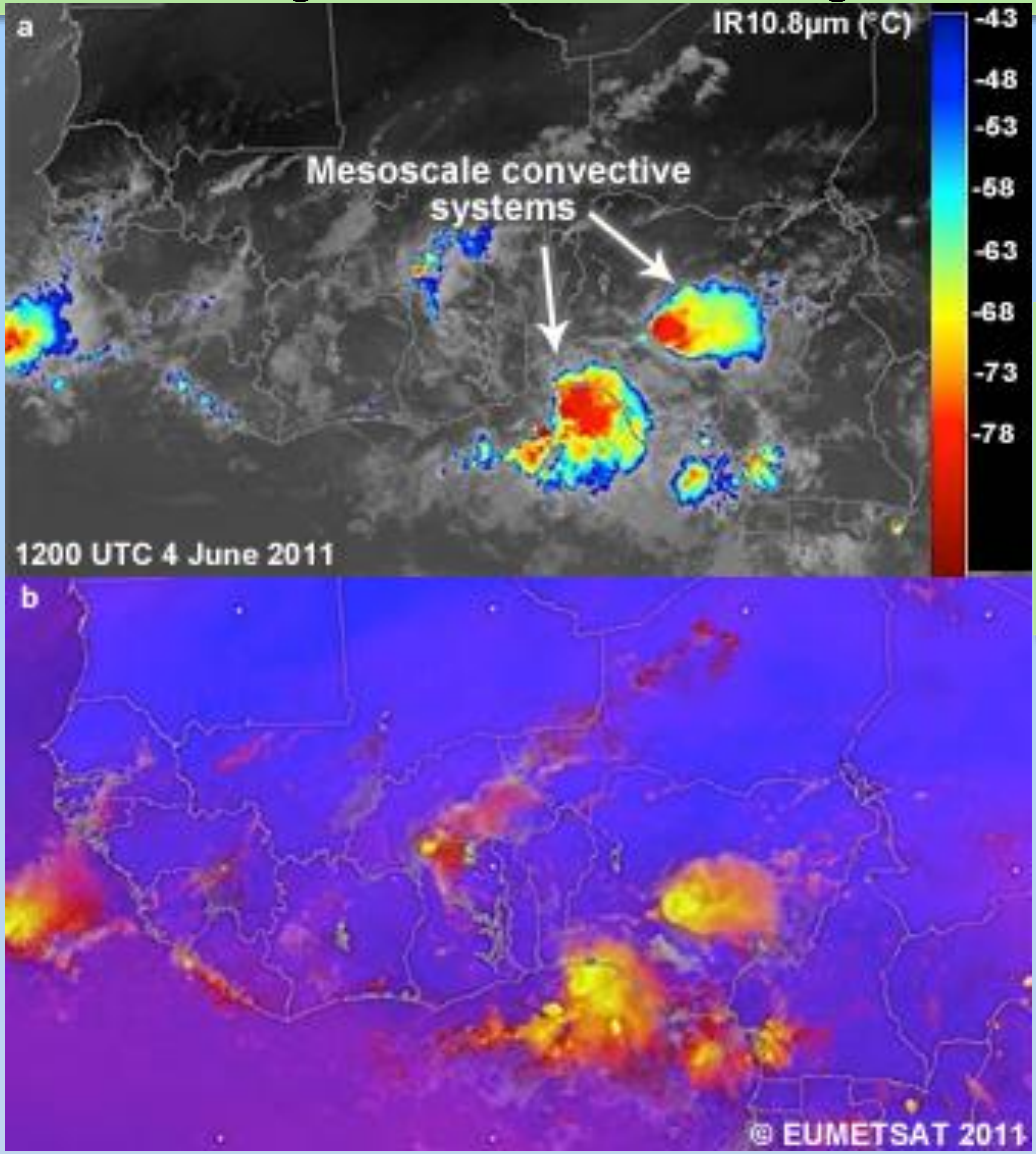

Figure 9.57. Convection satellite products for monitoring mesoscale convective systems: (a) colour-enhanced IR10.8 μm and (b) Convection RGB (© EUMETSAT 2011).

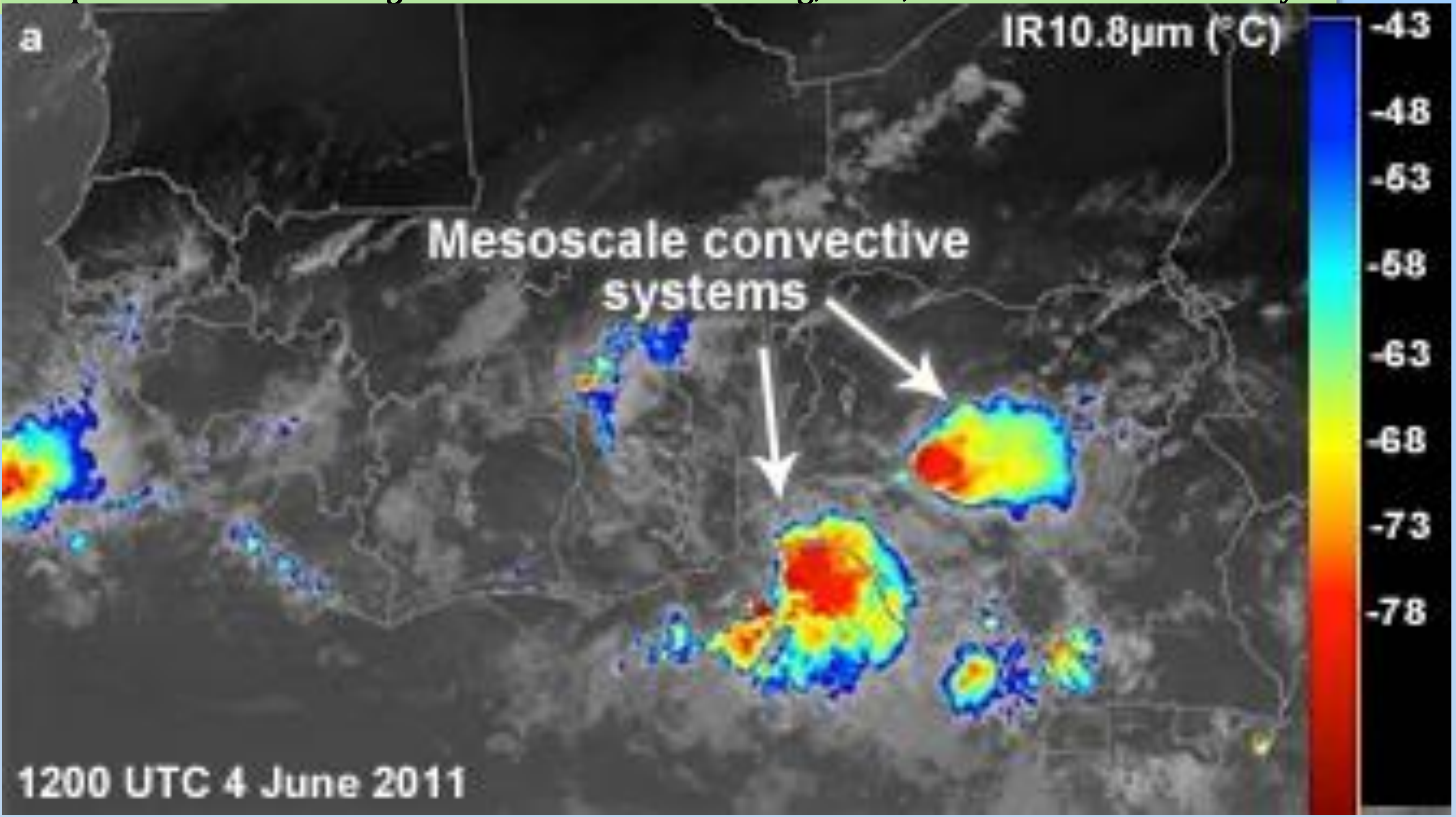

Figure 9.57(a) Convection satellite products for monitoring mesoscale convective systems: colour-enhanced IR10.8 μm.

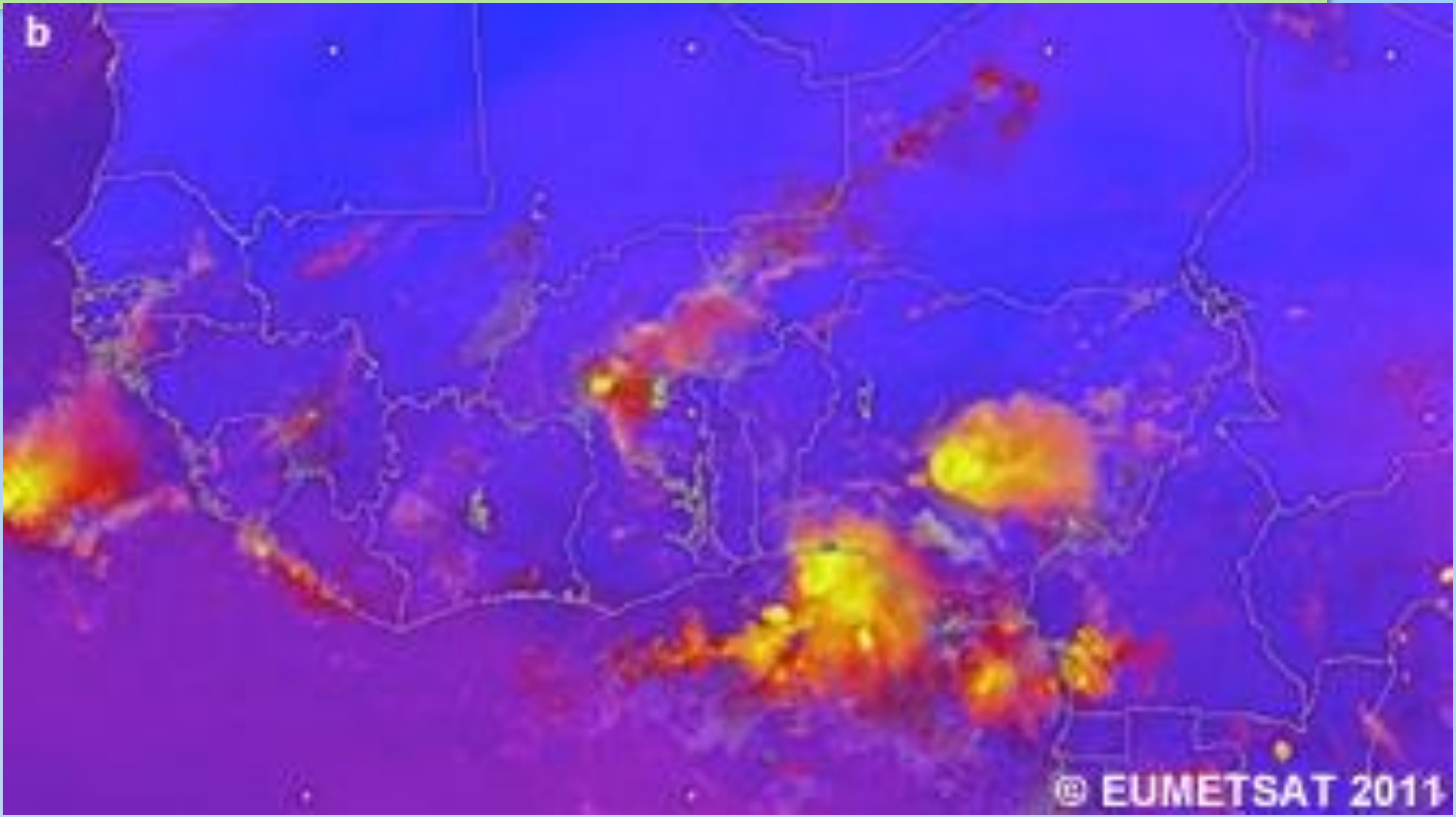

Figure 9.57(b) Convection satellite products for monitoring mesoscale convective systems: Convection RGB

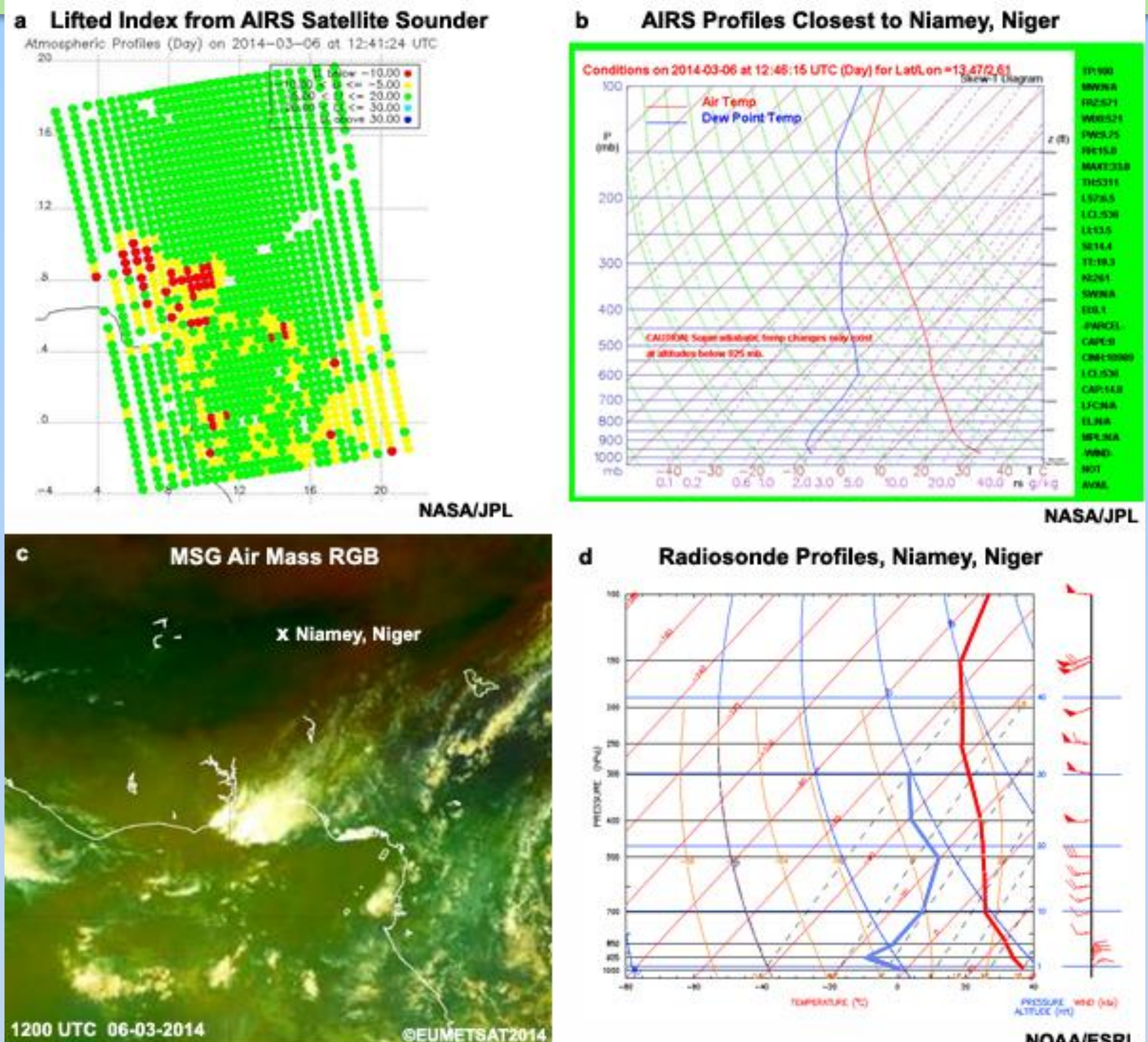

Figure 9.58. Example of real-time products from AIRS, Meteosat, and radiosondes on 6 March 2014: (a) Lifted Index derived from the sounder channels; (b) Skew-T log P plot at 12:46 UTC for location (13.47, 2.61); (c) Airmass RGB image at 1200 UTC, and (d) Skew-T log P plot from radiosonde at 1200 UTC.

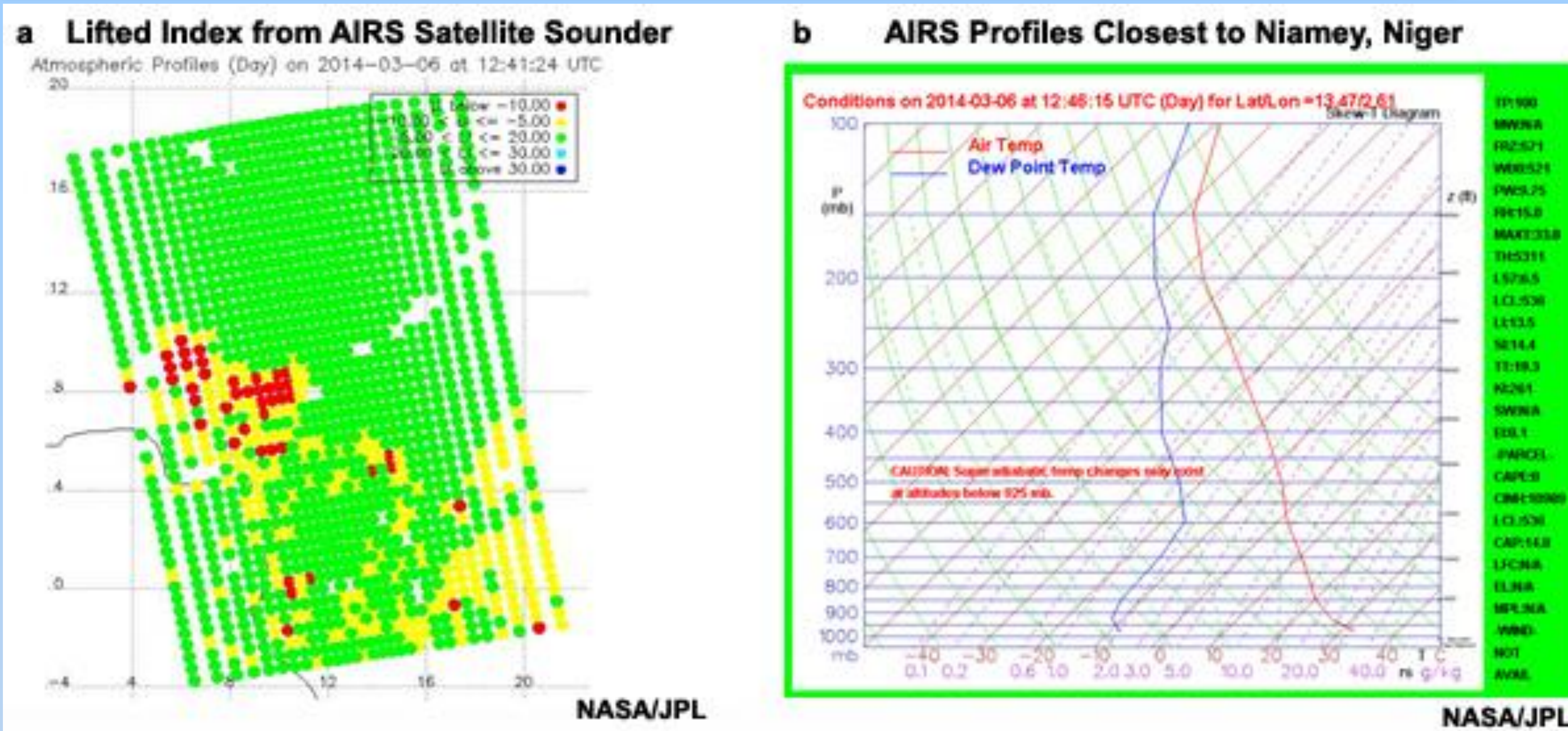

Figure 9.58. Example of real-time products from AIRS, Meteosat, and radiosondes on 6 March 2014: (a) Lifted Index derived from the sounder channels; (b) Skew-T log P plot at 12:46 UTC for location (13.47, 2.61)

African Monsoon Multidisciplinary Analysis
ACMAD
WMO

Chapter 9: *Remote Sensing* - Lead Author Arlene Laing, CIRA, Colorado State University

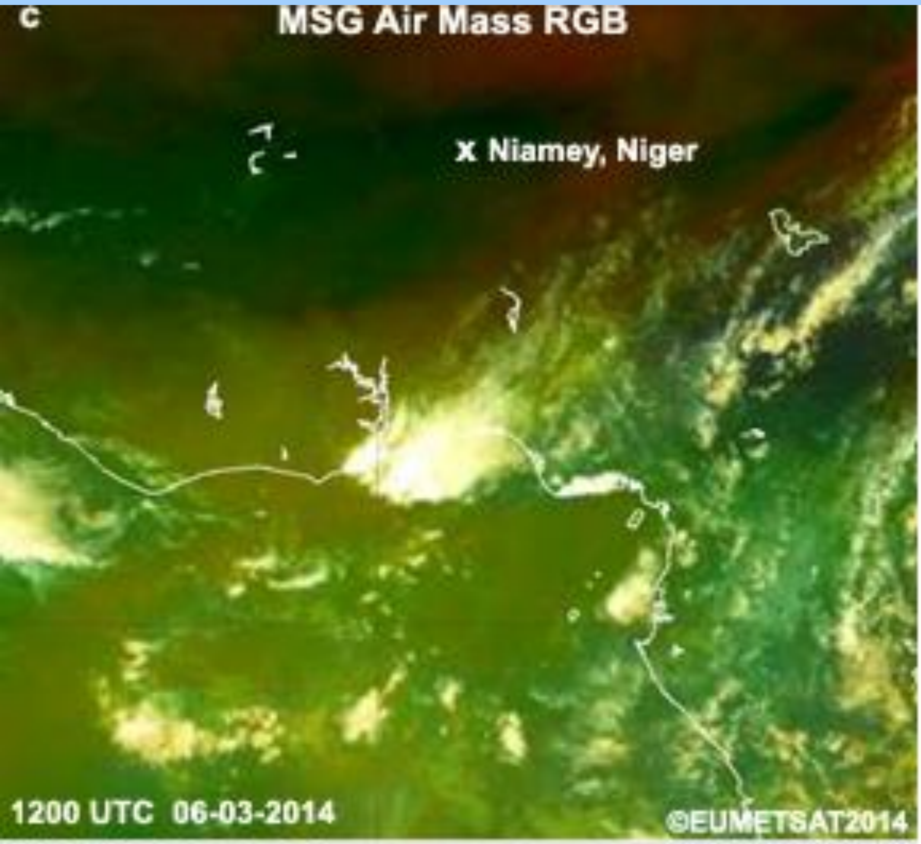

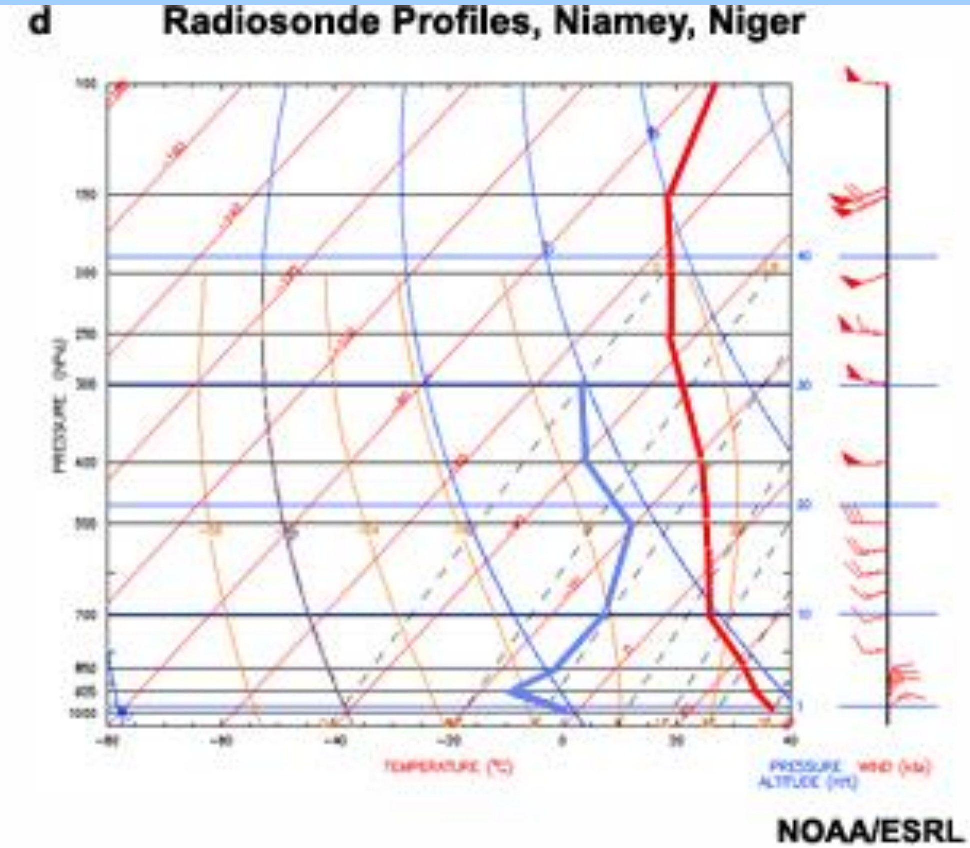

Figure 9.58. Example of real-time products from AIRS, Meteosat, and radiosondes on 6 March 2014: (c) Airmass RGB image at 1200 UTC, and (d) Skew-T log P plot from radiosonde at 1200 UTC.

Chapter 9: *Remote Sensing* - Lead Author Arlene Laing, CIRA, Colorado State University

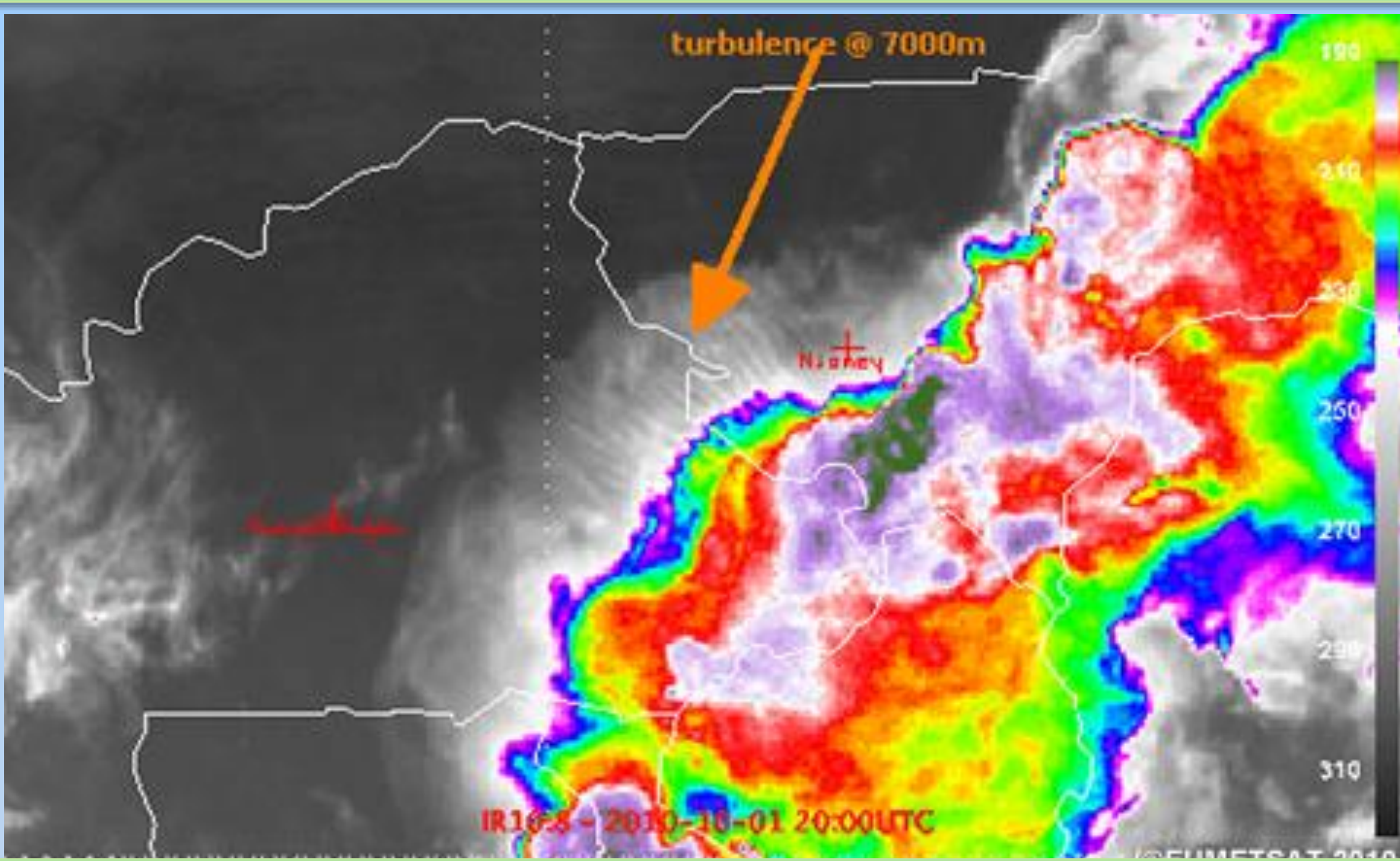

Figure 9.59. Near cloud turbulence generated by a mesoscale convective system over West Africa. Transverse wave lines mark the area of turbulence (©EUMETSAT 2010).

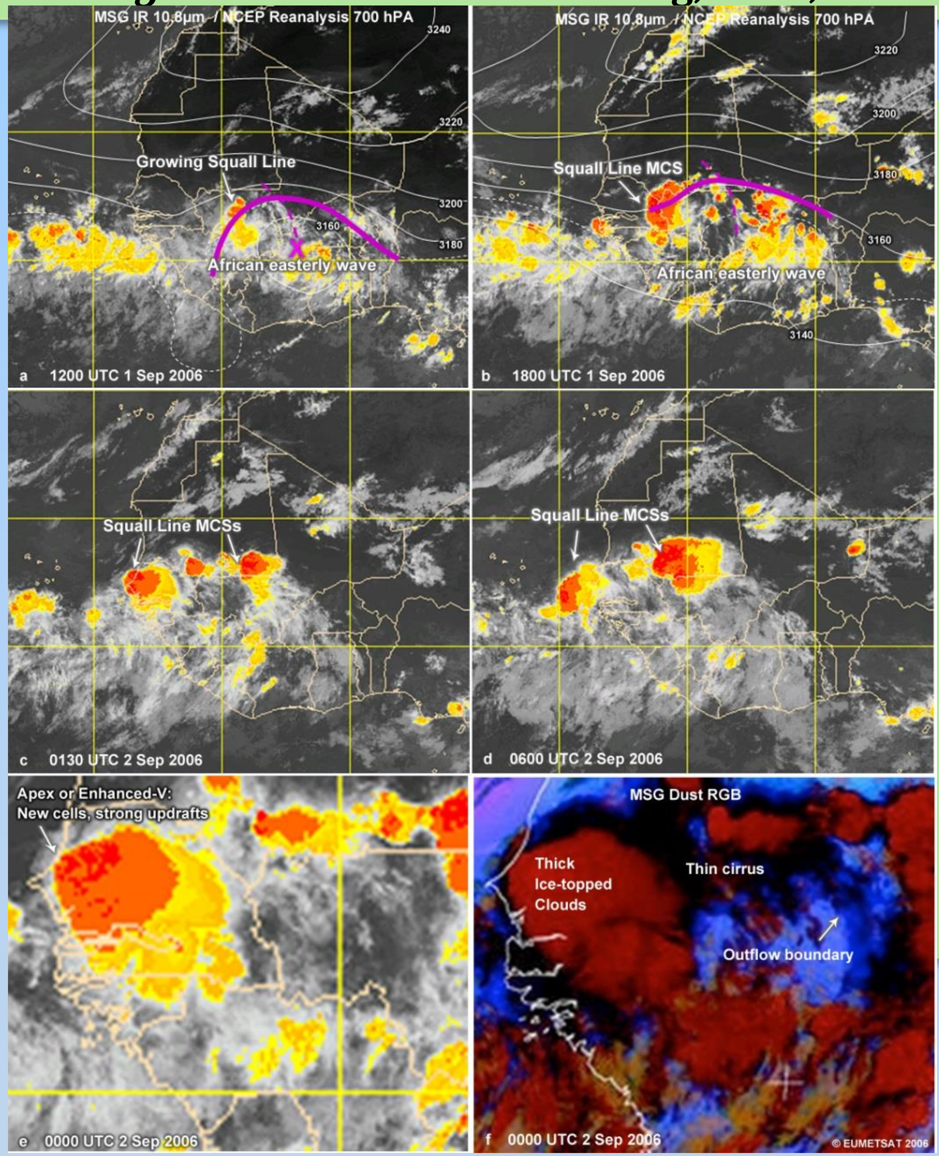

Figure 9.60. Enhanced Meteosat IR10.8 images of easterly wave and MCSs over West Africa at (a) 1200 UTC, (b) 1800 UTC 1 Sep, (c) 0130 UTC and (d) 0600 UTC 2 Sep 2006. (e) Zoomed in view of MCS at 0000 UTC and (f) Dust RGB view at 0000 UTC on 2 September. Orange contour in the IR10.8 images marks cloud tops colder than -65C. Panels (a) and (b) include contours of 700 hPa geopotential height with the wave trough and vortex highlighted in magenta.

Chapter 9: *Remote Sensing* - Lead Author Arlene Laing, CIRA, Colorado State University

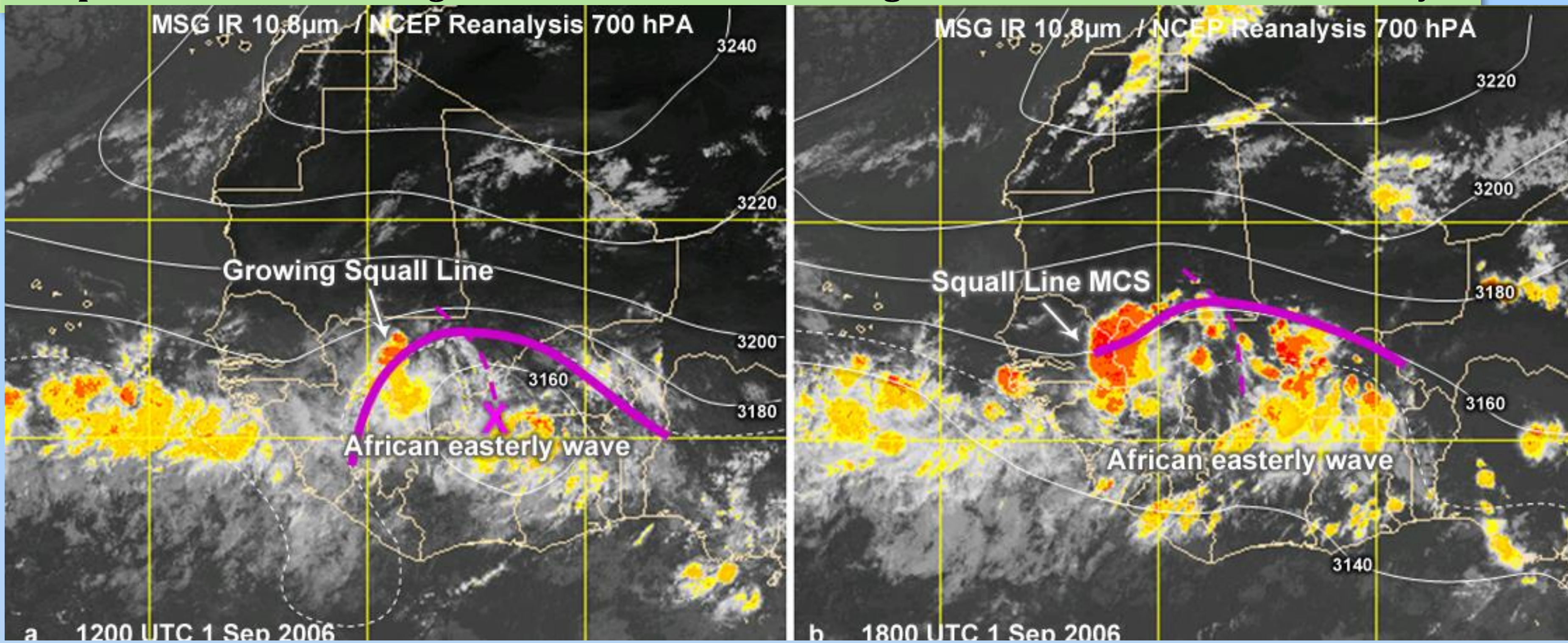

Figure 9.60. Enhanced Meteosat IR10.8 images of easterly wave and MCSs over West Africa at (a) 1200 UTC, (b) 1800 UTC 1 Sep. Orange contour in the IR10.8 images marks cloud tops colder than -65C. Panels (a) and (b) include contours of 700 hPa geopotential height with the wave trough and vortex highlighted in magenta.

Chapter 9: *Remote Sensing* - Lead Author Arlene Laing, CIRA, Colorado State University

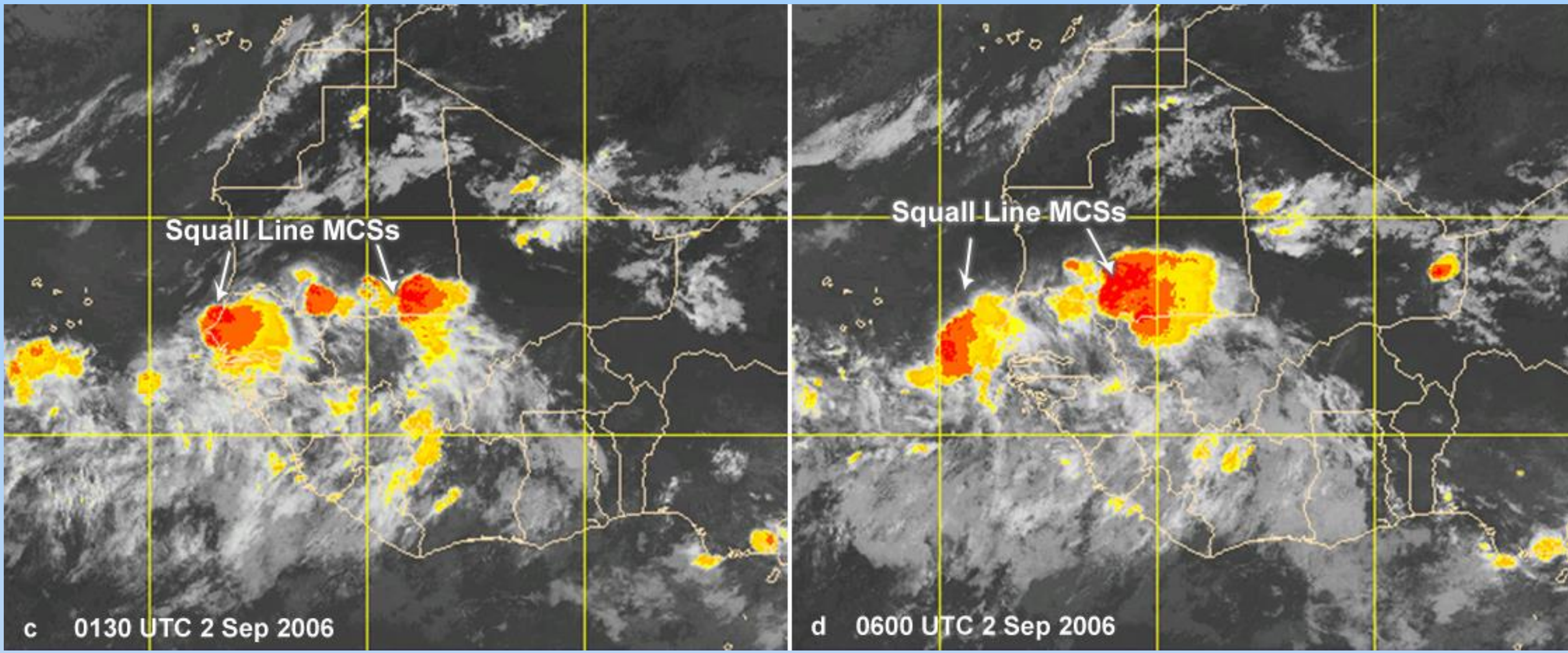

Figure 9.60. Enhanced Meteosat IR10.8 images of easterly wave and MCSs over West Africa at (c) 0130 UTC and (d) 0600 UTC 2 Sep 2006. Orange contour in the IR10.8 images marks cloud tops colder than -65C.

Chapter 9: *Remote Sensing* - Lead Author Arlene Laing, CIRA, Colorado State University

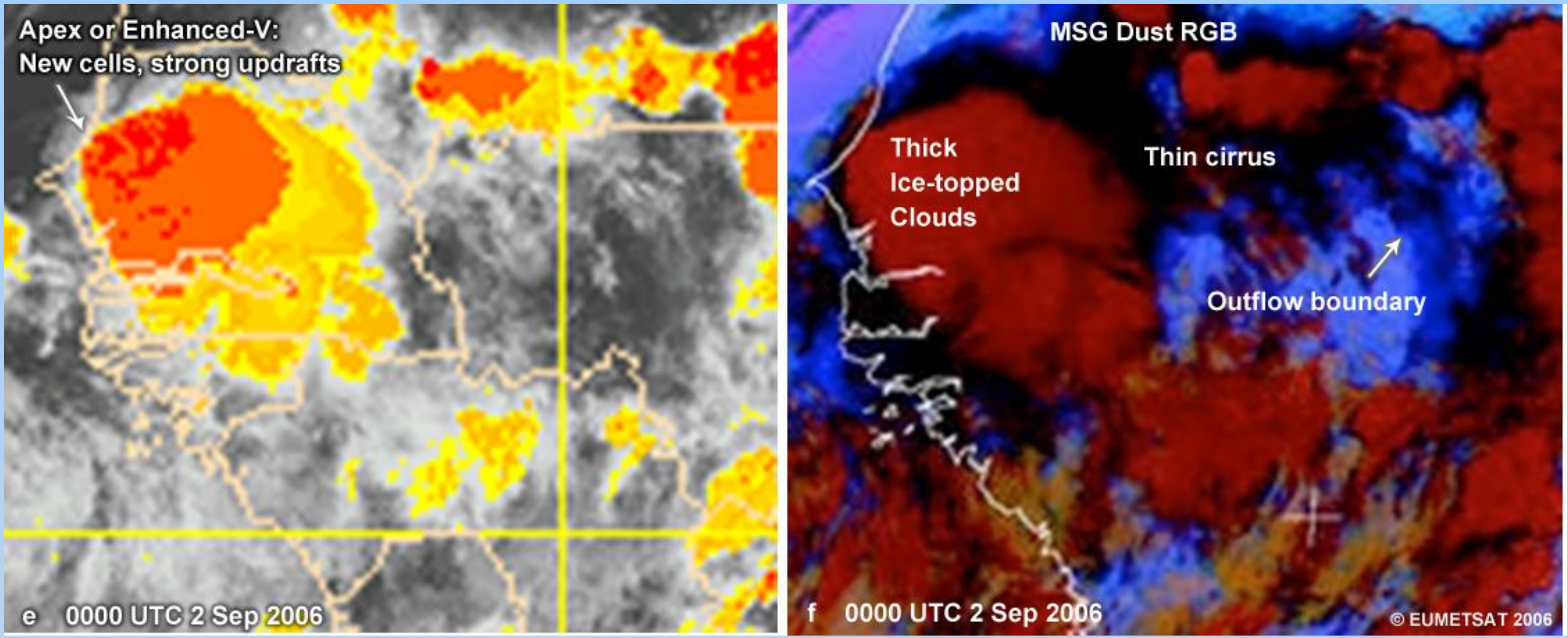

Figure 9.60. Enhanced Meteosat IR10.8 images of easterly wave and MCSs over West Africa at (e) Zoomed in view of MCS at 0000 UTC and (f) Dust RGB view at 0000 UTC on 2 September. Orange contour in the IR10.8 images marks cloud tops colder than -65C.

Chapter 9: *Remote Sensing* - Lead Author Arlene Laing, CIRA, Colorado State University

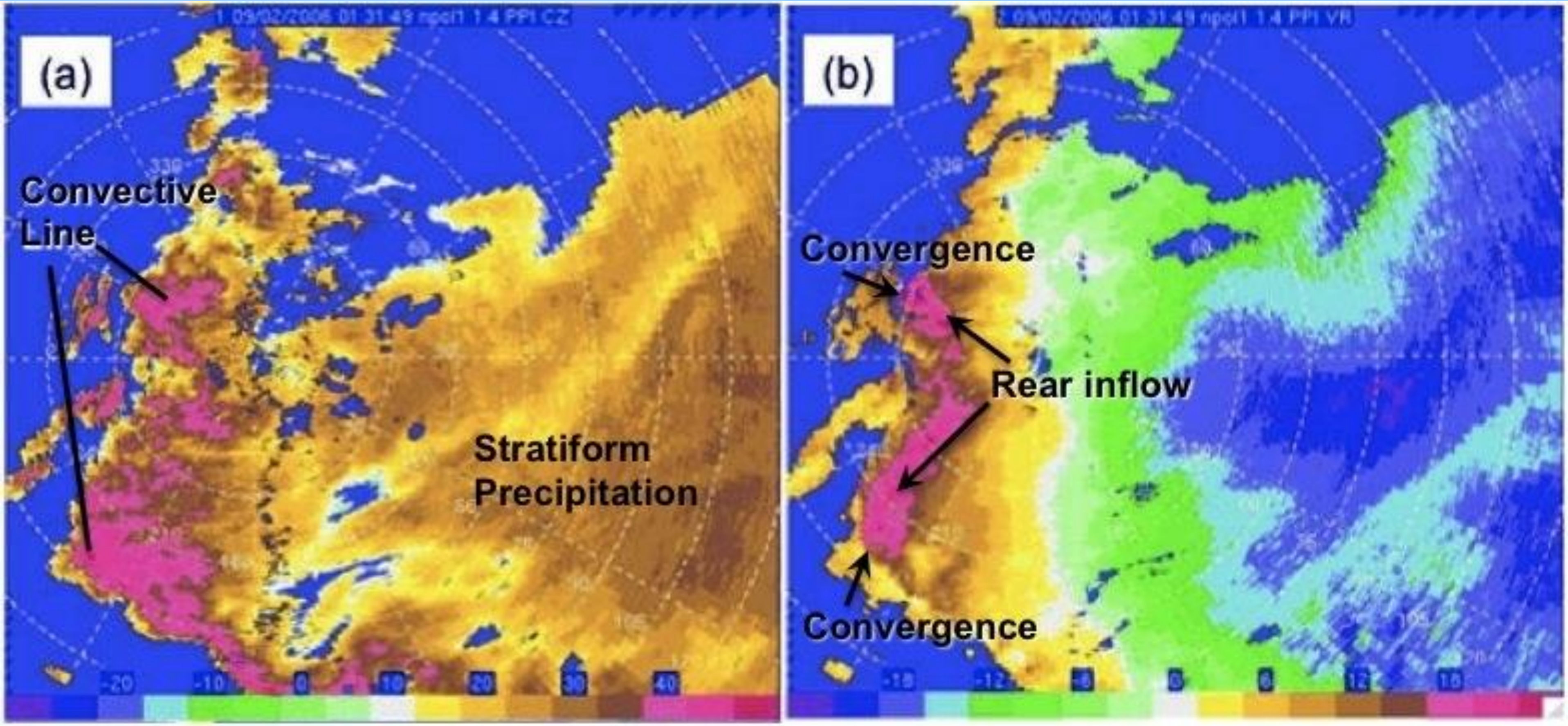

Figure 9.61. Low-level plan position indicator (PPI) scans of (a) radar reflectivity and (b) radial velocity (m s−1) from the NPOL radar, stationed at Dakar, Senegal, at 0132 UTC 2 Sep 2006. In (b) flow towards the radar is indicated by negative values (blue to green). Flow away from the radar is indicated by positive values (yellow to red). Reproduced from Cifelli et al. (2010).

Chapter 9: *Remote Sensing* - Lead Author Arlene Laing, CIRA, Colorado State University

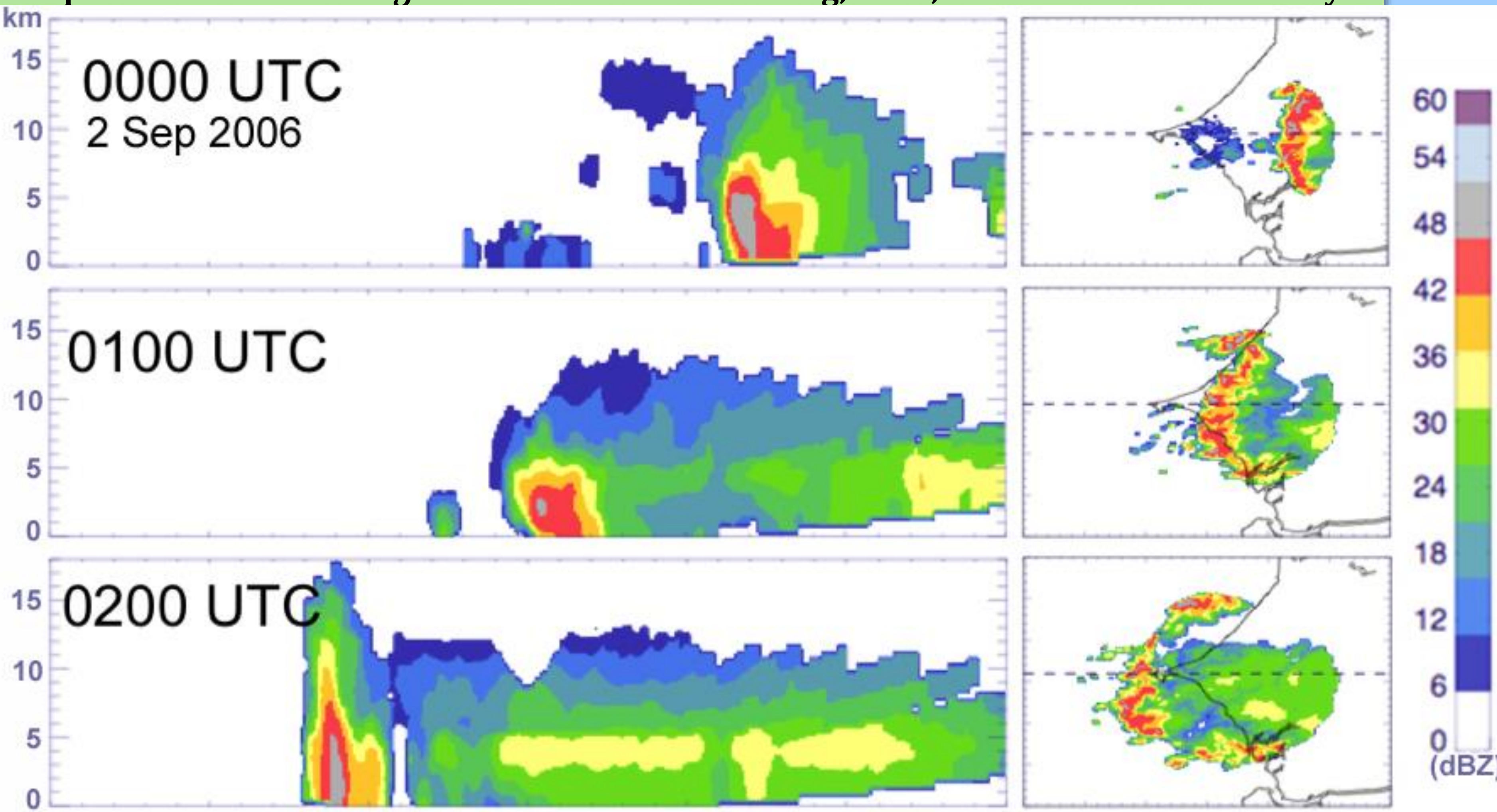

Figure 9.62 Radar reflectivity vertical cross-section and horizontal view of a squall line MCS that moved across the West African coast on 2 September 2006. Cross-sections are taken along the dashed line in the horizontal images (Courtesy of Amber Emory/NASA).

Chapter 9: *Remote Sensing* - Lead Author Arlene Laing, CIRA, Colorado State University

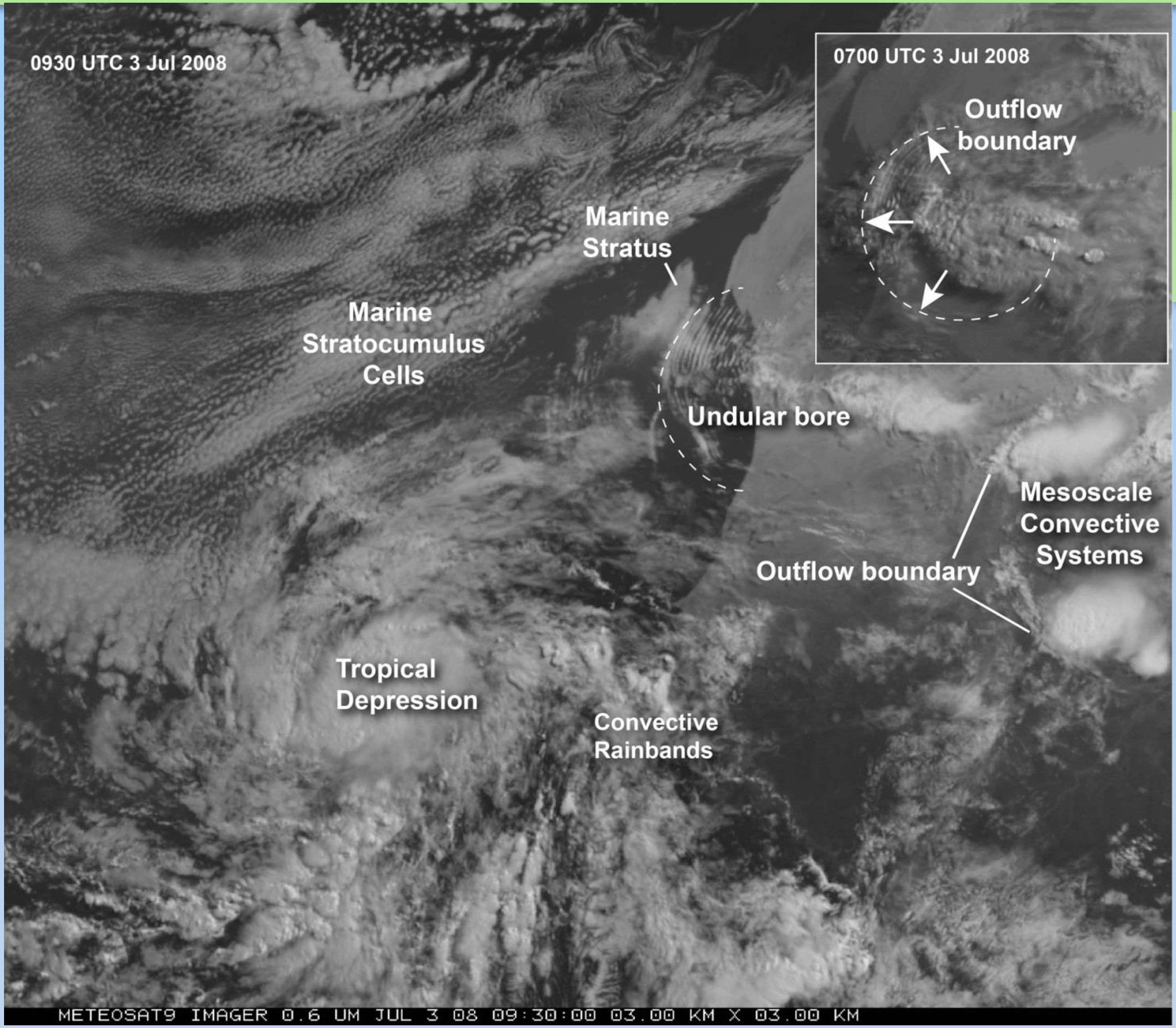

Figure 9.63(a) Meteosat Visible at 0930 and 1200 UTC, 3 Jul 2008 with many cloud systems.

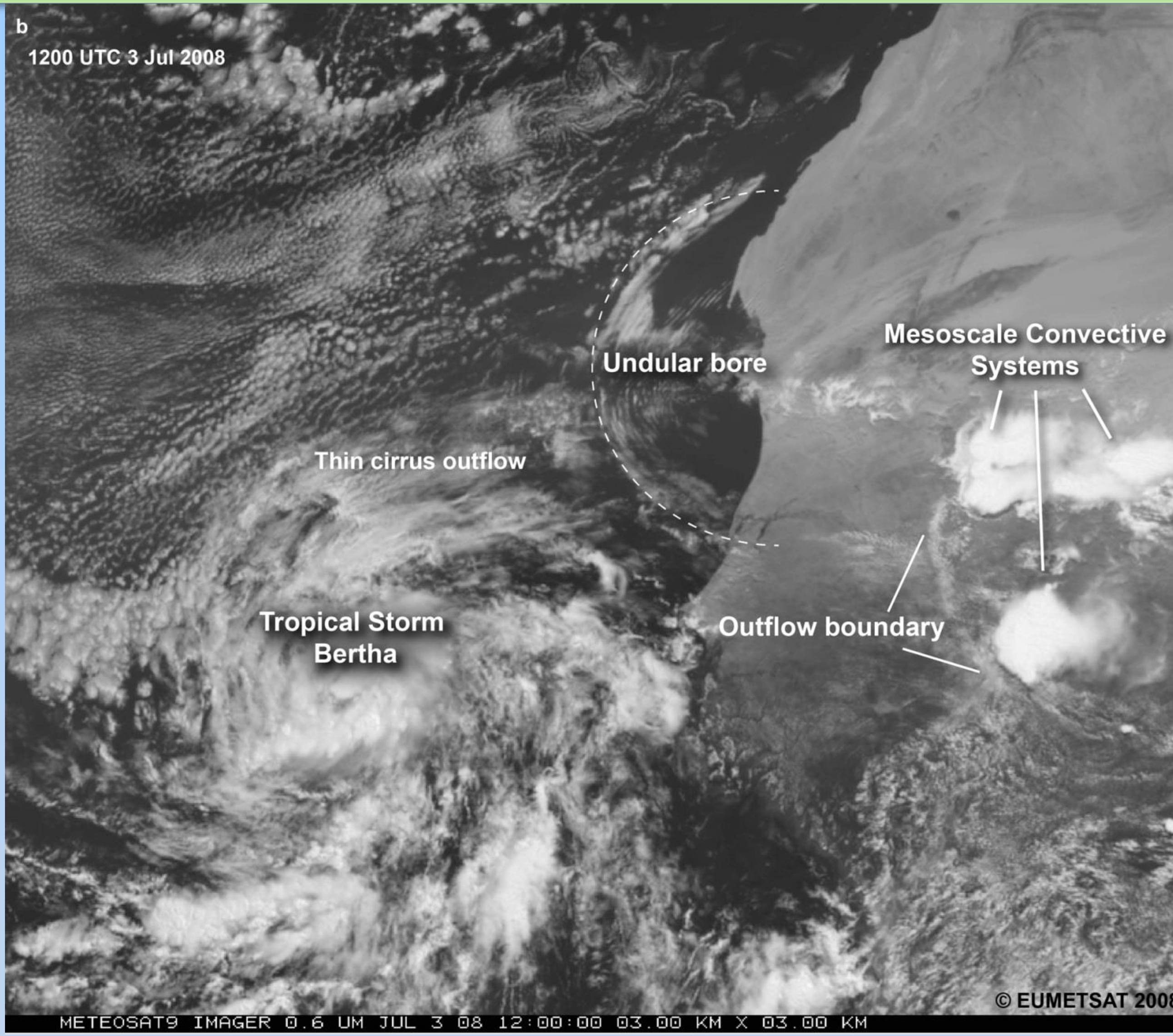

Figure 9.63(b) Meteosat Visible at 0930 and 1200 UTC, 3 Jul 2008 with many cloud systems.

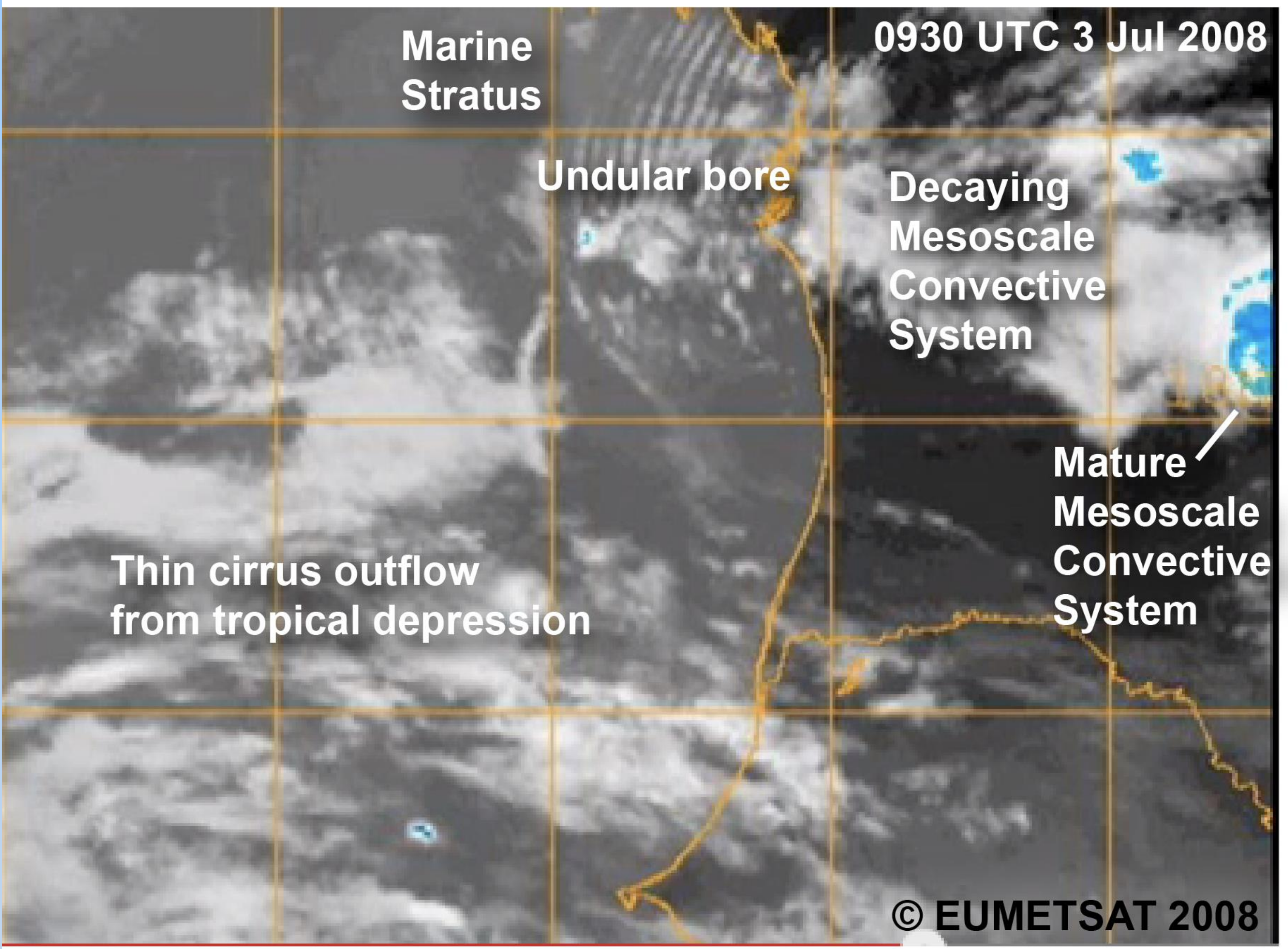

Figure 9.64. Meteosat IR 10.8 at 0930 UTC, 3 Jul 2008

Chapter 9: *Remote Sensing* - Lead Author Arlene Laing, CIRA, Colorado State University

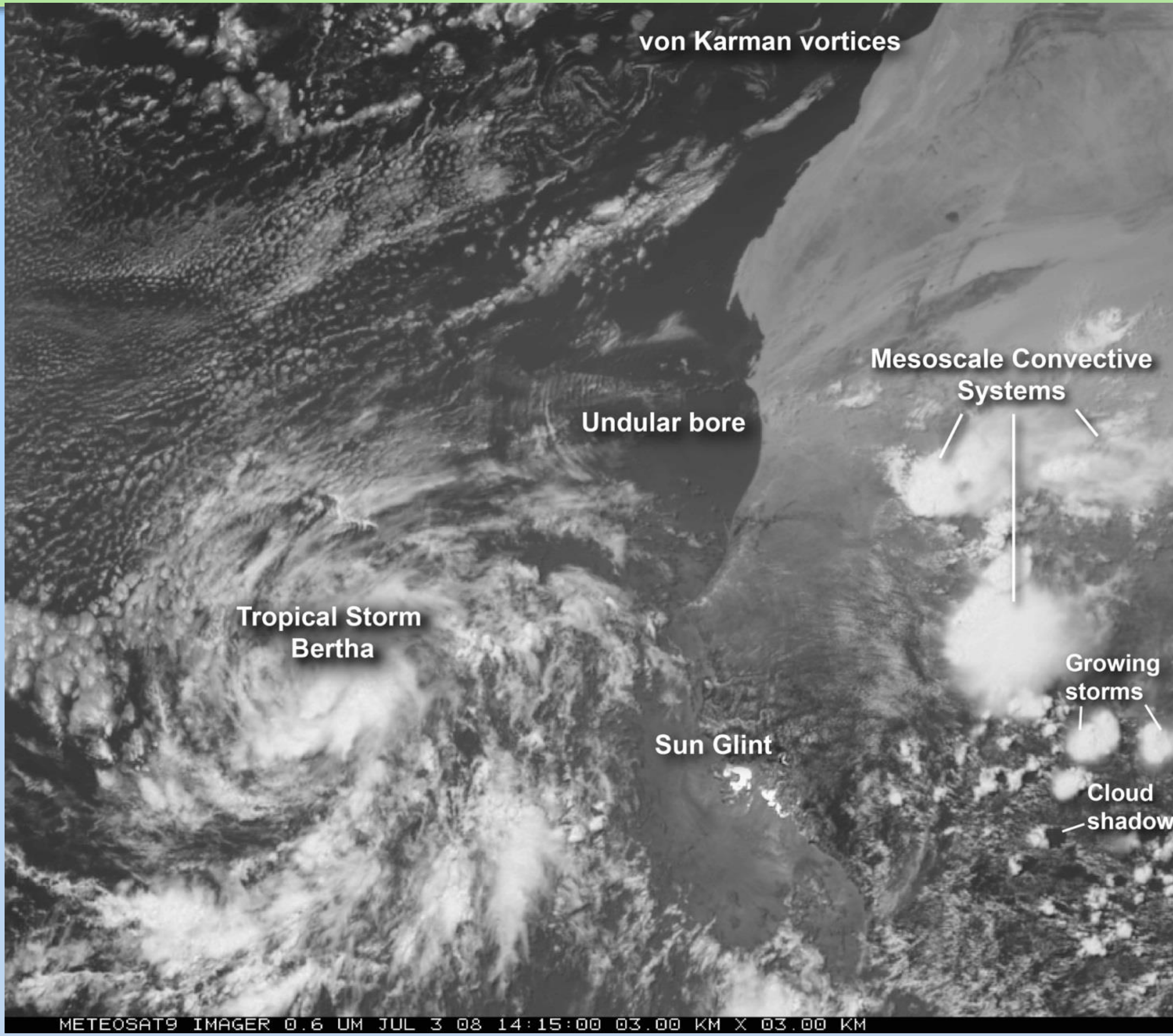

Figure 9.65. Meteosat Visible at 1415 UTC on 3 Jul 2008. Notice area of bright ocean due to sun glint, including small areas of bright white that would be misidentified as cloud.

African Monsoon Multidisciplinary Analysis